Time Dependent Finite Element Simulations of a Generalized Oldroyd-B Fluid

Ivajlo Donev

Thesis presented for the degree of Master of Science
in the department of Mathematics and Applied Mathematics
University of Cape Town

April, 2013

Plagiarism Declaration

I know the meaning of plagiarism and declare that all of the work in the document, save for that which is properly acknowledged, is my own.

Signed:__________________

Date: 15th April, 2013

Abstract

The main objective of this dissertation is to develop and implement a new finite element method to simulate time-dependent viscoelastic shear-thinning flows characterized by the generalized Oldroyd-B model. The developed algorithm is focused on increased stability by following theoretical arguments in the literature on developing free-energy dissipative schemes for the continuous system and discretely in the context of finite elements. The arguments presented in the literature involve using low-order piecewise-constant elements to approximate the extra stress field, which naturally preserve montonicity and the positive-definiteness of the conformation tensor. These properties ensure a consistent definition of a discrete free energy which is shown to dissipate with time and hence ensures stability of the solutions.

As numerical solutions to viscoelastic flows are notoriously difficult to obtain, various modifications and improvements are made to the algorithm, including: a pressure-projection method, a discontinuous Galerkin upwinding scheme and a symmetric interior penalty discontinuous Galerkin method. Each of these techniques is discussed in detail within this dissertation and combined to form a robust numerical scheme. A comparison is made to using higher-order discontinuous bilinear approximations for extra stress, where in addition we consider the influence of applying a slope limiter for these elements.

Improvements to the efficiency of the algorithm are made by the incorporation of a geometric multigrid preconditioner. A cell-wise Vanka smoother is implemented in the multigrid method to handle the block-matrix structure resulting from the mixed method. Additionally modifications required to handle hanging-nodes and non-uniformly refined meshes are also made to the preconditioner.

The algorithm is initially validated against two benchmark problems: flow over a confined cylinder and start-up driven cavity flow. These two problems are used as a basis to illustrate and compare the stability and accuracy of the resulting schemes when using both stress element choices. Start-up driven cavity flow is a transient problem, which provides a context in which to investigate the numerical consequences of some theoretical results concerning the stability of the generalized Oldroyd-B model, as found in the literature.

An application of the algorithm to modelling blood flow in arterioles and channels is considered by simulating pulsatile blood flow through a stenotic arteriole. Using a physiological set of model parameters the applicability and usefulness of the developed numerical method is illustrated. The individual influences of viscoelasticity and shear-thinning within the generalized Oldroyd-B model are investigated by comparing results to the Newtonian, generalized Newtonian and Oldroyd-B models. Recirculation flow, a new emerging flow feature, is observed solely as a result of shear-thinning and viscoelastic properties in combination.

Acknowledgements

I would like to express my gratitude for the guidance and support of my supervisor Prof. Daya Reddy. The work environment created by Prof. at CERECAM has been a stimulating and interesting place to learn and work. The many colleagues and friends there have provided me with much help throughout my masters, for which I am ever grateful. In particular I would like to acknowledge Jean-Paul Pelteret, Beverly Grieshaber and Timothy Povall. I would also like to thank Ruth Park for her patience and support and for putting up with my moaning when things weren't going to plan. Lastly, I would like to thank my family, without whom none of this would be possible. This work was carried out under the auspices of the South African Research Chair in Computational Mechanics.

Contents

Part I.

Introduction and Theory

1. Introduction

Fluid mechanics is a classical area of physics and mechanics which traditionally describes fluids on a continuum level. This is done by combining various conservation laws, expressed as the Navier-Stokes equations, with a constitutive equation that describes the material behaviour. The simplest class of fluids, which are referred to as Newtonian fluids, physically consist of small and light molecules. Materials such as water and air are typical examples. However many real materials do not possess such a simple underlying structure, and are constituted of large macromolecular or biological components. These materials often exhibit properties which are not predicted by the classic theory, but which nonetheless are very important to understand and be able to simulate, particularly for many industrial applications. To this end, the field of rheology seeks to describe these materials mathematically and the interesting properties these fluids possess.

One such property is shear-rate-dependent viscosity which is treated by generalizing the Navier-Stokes equations to have a viscosity that is a function of shear rate. Specific forms have been suggested in the literature, such as the empirically fitted Carreau-Yasuda function [20] and the thermodynamically derived model in [2].

Viscoelasticity is another non-Newtonian property, which arises from structures on the molecular level which deform elastically. These are often referred to as fluids with *memory*, as the history of these deformations propagates with the fluid (see [10]). This sub-continuum description is most successfully handled by statistical means, wherein an ensemble of a molecular model, such as a dumbbell, is considered and a constitutive equation for the stress is derived when ensemble averages are taken over phase space. Various models have been developed in this manner which result in differential constitutive equations such as the Oldroyd-B, the Upper Convected Maxwell model (UCM) and more complicated models such as the Phan-Thien Tanner (PTT) and FENE models. A very comprehensive review on the different models may be found in [70, 10].

In this work we focus on the Oldroyd-B (OB) model [67] which has received much attention in the literature from both a computational and theoretical perspective. This model is appropriate for viscoelastic fluids with constant viscosity, or Boger fluids [49]. We will also consider the generalized Oldroyd-B (GOB) model, which is a recent generalization by incorporating shear-thinning, as in [91]. This model has been used to more accurately describe blood flow. Although this generalized model has to date received relatively little attention from numerical studies, there are a few works in which simulations have been performed using this model. In Pontrelli [75] a 1D investigation of a pulsatile GOB fluid was performed, while more recently in Bodnar *et.al.* [12] a 3D finite volume method was used to simulate steady blood flow in a stenosed artery. This application to blood flow will be further discussed in chapter 7.

The constitutive equations for the OB and GOB models are nonlinear and hyperbolic in character. Furthermore they form part of a larger coupled system of equations which also describe the velocity and pressure. Due to these considerations, finding solutions for these fluids remains a great challenge, and for all but the simplest of geometries [41] there exist no analytical solutions. For this reason computational methods have been widely used to obtain approximate solutions for more complicated flows. However, from the earliest attempts of computational rheology, a common problem was observed that all methods fail to converge with increasing value of a dimensionless number: We - the Weissenberg number. This number is related to the relaxation time of the elasticity in the fluid. This issue was thus coined the "high Weissenberg number problem" (HWNP) ([55]) and has to date not been fully resolved.

Although the HWNP affects all viscoelastic models, the limits on We are lowest for the UCM model where there is no solvent viscosity. In a review of this problem, Keunings [55] states that the source of the problem is most likely numerical in nature, as the apparent limits of We reached showed sensitivity with mesh refinement. The numerical difficulty in capturing sharp stress gradients was deemed the likely culprit. This view is also expressed in Boyaval *et.al.* [15], where focus was placed on the OB model.

In the literature various approaches have been used to numerically simulate viscoelastic flows at ever increasing We numbers using different techniques, although finite elements have been most commonly used. The difficulties encountered from the hyperbolic character of the constitutive equation have been treated using Petrov-Galerkin upwinding schemes (SU and SUPG), as introduced by Brooks and Hughes [17] and Marchal and Crochet [62]. Alternatively, the discontinuous Galerkin (DG) method for hyperbolic problems, as introduced by Lesaint and Raviart [58] for neutron transport, has also received significant attention. A comparative review of these two methods may be found in Yurun [94].

Another difficulty lies in the coupled nature of the equations and the compatibility restrictions which arise in the choice of finite element spaces for each field. The pair of spaces for the velocity and pressure are required to satisfy the LBB condition, common for incompressible flow, whereas in the limit of a UCM fluid, additional compatibility between velocity and extra-stress spaces is required (see page 188 in [70] for a more complete discussion). A slight reformulation of the governing equations may be used to circumvent these requirements. One way in which this is done is Elastic Viscous Stress Splitting (EVSS), where the stress is reformulated so as to introduce additional viscosity in the momentum equation. An alternative approach is through the use of an adaptive viscosity within the Adaptive Viscous Stress Splitting (AVSS) formulation. Variants of these methods, which have gained popularity in the literature, are the DEVSS and DAVSS formulations where the deformation gradient is treated as an additional unknown field. A comparative review of these methods may be found in Baaijens [6].

Despite the developments described above and the vast amount of computational work performed on viscoelastic flows, a solid mathematical foundation was still required when discussing the stability of the resulting methods. This topic was dealt with, amongst others, by Lozinski *et.al.* [61] where a free energy estimate was derived for the OB model. This estimate under zero-flow boundary conditions showed unconditional exponential decay and hence guaranteed the stability of the continuous system in the long-time limit, acting as a Lyaponuov functional. The arguments presented in this work were based on a conformation tensor formulation of the governing equations. This is advantageous as it was shown that the positive-definiteness of the conformation tensor is maintained in the evolution of the system. This property corresponds well to the physical interpretation of the conformation tensor. In Mohammed and Reddy [64] similar arguments were presented for the GOB system, wherein there emerged a constraint on a quantity ζ, depending on the flow and model parameters to obtain a similar free-energy dissipation.

These notions were further extended by Boyaval *et.al.* [15] where it was shown that similar free-energy dissipative properties would carry over to a discrete form of the problem obtained by a finite element method when a low order discontinuous stress space was chosen. The theorems presented in this work concerned triangular elements in 2D with a DG stabilization of the constitutive equation.

1.1. Purpose of Study

It is on these arguments of stability that we base the work in this dissertation. Ultimately we seek to develop and implement a robust 2D finite element method to solve transient problems using the GOB model. The choice of elements is based on quadrilateral analogues to those presented in [15], using a DG-upwinding method for the constitutive equation. We additionally seek to improve the robustness and efficiency of the method by incorporating various modifications. These include a pressure-projection method to deal with incompressibility, a Newton Raphson method with line-search to deal with nonlinearity, a symmetric interior penalty DG method to solve the elliptic pressure update equations and geometric multigrid preconditioning to improve the efficiency of the algorithm.

We also wish to compare this very low-order piecewise constant space for the stress to a higher-order piecewise bilinear discontinuous space in terms of accuracy and stability. This numerical method will provide a basis to study the behaviour of the free energy estimates under different flows. We treat the resulting mixed method monolithically, i.e. solve for all the variables simultaneously, and treat the time dependence fully implicitly so as to improve the robustness. We additionally consider the application of a slope limiter or monotonicity enforcer, to improve the robustness and stability, comparing the accuracy of the solutions obtained with and without its application.

1.2. Outline of Work

This dissertation is organized into three parts, “Introduction and Theory”, “Numerical Work” and “Results and Conclusions”. The first part consists of chapter 1 and 2, where in chapter 1 a brief overview of the work and some of the relevant literature is presented. In chapter 2 much of the relevant theory used is discussed including: a continuum description of fluids used to obtain the governing equations for the Oldroyd-B model and its generalized form, alternative models for viscoelasticity and shear-thinning and the dimensionless forms of the governing equations. Furthermore some expansion on the HWNP is discussed in connection to theoretical results used to obtain a free-energy dissipative scheme.

In part 2, the numerical aspects of the work are discussed, consisting of chapters 3, 4 and 5. In chapter 3 the basis of finite elements is presented with specific details concerning their application to the GOB problem. In chapter 4 various aspects of the developed method are discussed individually and in conjunction to the method as a whole. Lastly, in chapter 5 focus is placed on multigrid methods, first generally and then as applied for the GOB problem.

The last part consists of chapters 6, 7 and 8. In chapter 6 the numerical method developed in the previous chapters is validated against two popular benchmark problems. The first is the problem of steady flow over a confined cylinder, while the second is the start-up driven cavity problem. In the first problem focus is placed on comparing the accuracy and stability of the resulting scheme when using each stress element. In the second problem focus is placed on the evolution of the free energy of the system and the numerical consequences of the theoretical results presented in chapter 2. In chapter 7 an application of the model to simulating pulsatile blood-flow through a stenotic channel is presented along with additional results concerning the accuracy and stability of the numerical scheme. In chapter 8 some concluding remarks are presented and prospective work arising from this dissertation is discussed. This dissertation additionally includes an appendix in which the methods and results used to obtain boundary conditions for Poiseuille flow are discussed.

2. The Oldroyd-B Fluid: Standard and General Models

In this chapter we introduce the Oldroyd-B model and its generalized form by systematically moving from the basic principles of continuum mechanics to fluid mechanics, non-Newtonian properties and then to viscoelasticity. We also present a brief overview of some alternate models and derivations. We conclude this chapter by discussing the High Weissenberg Number Problem in relation to the work presented in the literature on free-energy dissipative properties for the generalized Oldroyd-B system.

2.1. Frames of Reference

When dealing with fluids mathematically one needs to differentiate between Lagrangian and Eulerian frameworks. In a Lagrangian frame we consider an infinitesimal volume of a fluid which moves with the flow. This effectively describes the particles which constitute the fluid. On the other hand, in a Eulerian frame the fluid is described from a fixed or "lab" frame. It is important to define the connection between these two frameworks so that we may translate the kinematic behaviour in the Lagrange frame to a more useful Eulerian frame. To do so, we let the position of such a volume at time $t = 0$ be defined as $\boldsymbol{x}_0$ and the path along which this volume moves to be defined by $\boldsymbol{x}(\boldsymbol{x}_0, t)$, as shown in figure 2.1.

This mapping is thus a function not only of time, but also of the initial position of the material volume $\boldsymbol{x}_0$. The velocity of this fluid parcel is then defined by

$$\boldsymbol{u}(\boldsymbol{x}, t) = \frac{\partial \boldsymbol{x}(\boldsymbol{x}_0, t)}{\partial t}. \tag{2.1}$$

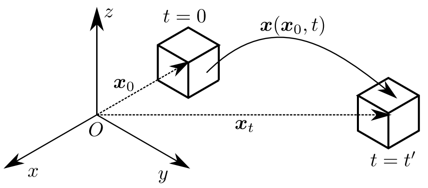

Figure 2.1. – Motion of a material volume in the Eulerian frame

To obtain the acceleration of the volume element, (2.1) is differentiated with respect to time and the chain rule applied to yield

$$\begin{aligned}\frac{\mathrm{D}u}{\mathrm{D}t} &= \frac{\partial \boldsymbol{u}}{\partial t} + (\boldsymbol{\nabla u}) \cdot \frac{\partial \boldsymbol{x}}{\partial t} \\ &= \frac{\partial \boldsymbol{u}}{\partial t} + \boldsymbol{u} \cdot \boldsymbol{\nabla u}. \end{aligned} \tag{2.2}$$

In (2.2) $\frac{\mathrm{D}}{\mathrm{Dt}}(\cdot)$ is known as a material derivative and is the appropriate time derivative for any transportable property of the field $\Phi(\boldsymbol{x}(\boldsymbol{x}_0, t), t)$ such as density, temperature or tensorial quantities such as stress etc... Thus for a general field this is defined as

$$\frac{D\Phi}{Dt} = \frac{\partial \Phi}{\partial t} + \boldsymbol{u} \cdot \boldsymbol{\nabla}\Phi. \tag{2.3}$$

2.2. Kinematic Equations

With this distinction made between the two frames of reference, we are now able to derive some kinematic equations to describe the motion of a fluid. These will be derived from various conservation laws which are known to hold true a priori for all materials. We begin with the most fundamental law in classical mechanics: conservation of mass.

2.2.1. Conservation of Mass

We consider an arbitrary fixed material volume $\mathcal{V}(t)$ in the domain Ω which moves with the flow. Assuming the mass of the fluid within this volume remains constant, it then follows that

$$\frac{\mathrm{d}}{\mathrm{dt}} \int_{\mathcal{V}(t)} \rho \, \mathrm{d}\mathcal{V} = 0 \tag{2.4}$$

where $\rho(\boldsymbol{x}, t)$ is the density of the fluid. Applying Reynolds transport theorem[1] to (2.4), it then follows that

$$\int_{\mathcal{V}(t)} \left(\frac{\partial \rho}{\partial t} + \boldsymbol{\nabla} \cdot (\rho \boldsymbol{u}) \right) \mathrm{d}\mathcal{V} = 0. \tag{2.5}$$

To simplify matters, we assume that for an incompressible fluid the density is constant in time and independent of position. Furthermore, since (2.5) holds true for any arbitrary material volume $\mathcal{V}(t)$ it must also hold true for all points in the domain. Hence the

---

[1] Reynolds transport theorem, following [70] (page 373), states that if $\mathcal{V}(t)$ is any material volume and $G(\boldsymbol{x}, t)$ is any scalar or vector field it then follows that

$$\frac{d}{dt} \int\limits_{V(t)} G \, \mathrm{d}\mathcal{V} = \int\limits_{V(t)} \left(\frac{DG}{Dt} + G \boldsymbol{\nabla} \cdot \boldsymbol{u} \right) \mathrm{d}\mathcal{V}$$

conservation of mass law, together with the assumption of incompressibility leads to the continuity equation

$$\boldsymbol{\nabla}\cdot \boldsymbol{u} = 0. \tag{2.6}$$

2.2.2. Conservation of Momentum

To describe the motion of a fluid we consider once again a material volume $\mathcal{V}(t)$ with bounding surface $\partial\mathcal{V}(t)$. By considering the conservation of momentum for this material volume we arrive at

$$\frac{\mathrm{d}}{\mathrm{dt}} \int_{\mathcal{V}(t)} \rho \boldsymbol{u}\, \mathrm{d}\mathcal{V} = \int_{\mathcal{V}(t)} \boldsymbol{f}\, \mathrm{d}\mathcal{V} + \oint_{\partial\mathcal{V}(t)} \boldsymbol{g}\, \mathrm{dS}, \tag{2.7}$$

where the left-hand side represents the rate of change of momentum and the right-hand side represents body forces $\boldsymbol{f}$ acting on the volume (such as gravity) and the traction forces on the surfaces $\boldsymbol{g}$, such as friction from neighboring layers of the fluid. It can be shown that traction forces $\boldsymbol{g}$ may be expressed as $\boldsymbol{g} = \boldsymbol{n} \cdot \boldsymbol{S}$, where $\boldsymbol{S}$ is the 2^{nd} order Cauchy stress tensor (see [70] Appendix A.1). Reynolds transport theorem is once again applied to the left hand side followed by Gauss's divergence theorem to transform the surface integral in (2.7) to a volume integral expressed as

$$\int_{\mathcal{V}(t)} \left(\rho \frac{\partial \boldsymbol{u}}{\partial t} + \rho \boldsymbol{u} \cdot \nabla \boldsymbol{u} \right) \mathrm{d}\mathcal{V} = \int_{\mathcal{V}(t)} (\boldsymbol{b} + \boldsymbol{\nabla} \cdot \boldsymbol{S})\, \mathrm{d}\mathcal{V}. \tag{2.8}$$

Since (2.8) holds for any general material volume it must also hold point-wise, resulting in the momentum equation

$$\rho \frac{\mathrm{D}\boldsymbol{u}}{\mathrm{Dt}} - \boldsymbol{\nabla}\cdot \boldsymbol{S} = \boldsymbol{b}. \tag{2.9}$$

The conservation of energy is perhaps the most important of conservation laws. In the context of fluid mechanics it provides the relationship between the temperature and the velocity field of the fluid. Since only isothermal flows will be considered in this work, details of this will be omitted. Additionally, by considering the conservation of angular momentum it can be shown that the stress tensor is symmetric (see [24] for a detailed introduction to fluid mechanics).

The stress tensor is frequently decomposed into two separate tensors as

$$\boldsymbol{S} = -p\boldsymbol{I} + \boldsymbol{T}, \tag{2.10}$$

where p denotes the hydrostatic pressure and $\boldsymbol{T}$ denotes the deviatoric stress, which is dependent on the rate of deformation. The exact definition of the deviatoric stress depends on the particular choice of material or fluid as discussed in the next section.

2.3. Constitutive Equations

2.3.1. Newtonian Fluids

Up to this point no mention has been made of the fluid material, with the conservation laws above applying universally to all fluids. However, to fully describe a specific fluid system a definition of the stress tensor is required in terms of the velocity field. The simplest fluids, corresponding to either gases or liquids with light molecular substructure, are referred to as Newtonian fluids. For this class of fluids the stress tensor is assumed to consist only of linear combinations of the first derivatives of the velocity. Furthermore it is also assumed to be isotropic and symmetric as mentioned above. By combining all these assumptions, we may define the deviatoric stress tensor, in the incompressible limit, as

$$\boldsymbol{T} = \eta \dot{\boldsymbol{\gamma}} \tag{2.11}$$

where η is the viscosity and $\dot{\boldsymbol{\gamma}}$ is the rate-of-strain tensor, defined as

$$\dot{\boldsymbol{\gamma}} = \boldsymbol{\nabla u} + (\boldsymbol{\nabla u})^T . \tag{2.12}$$

With this definition, it is now possible to write the full Navier-Stokes equations for an incompressible, isothermal fluid in a bounded domain $\Omega \subset \mathbb{R}^2$or $\mathbb{R}^3$ with Lipschitz boundary $\partial\Omega$ as

$$\begin{aligned} \rho \frac{\mathrm{D}\boldsymbol{u}}{\mathrm{Dt}} - \boldsymbol{\nabla} p + \eta \boldsymbol{\nabla}^2 \boldsymbol{u} &= \boldsymbol{b}, \\ \boldsymbol{\nabla} \cdot \boldsymbol{u} &= 0. \end{aligned} \tag{2.13}$$

2.3.2. Non-Newtonian Fluids

Although some of the most common fluids such as air and water can be considered as Newtonian; the assumptions made are not appropriate for all materials. In particular, macromolecular fluids such as polymer solutions and many biological fluids are composed of structures whose orientation, interaction and internal properties does affect the macroscopic flow. These fluids exhibit properties and effects which are not predicted by the Navier-Stokes equations.

The most common of these effects in everyday materials is shear-rate-dependent viscosity, as found in many food stuffs such as tomato sauce, molten chocolate and cream. We will only focus on materials which exhibit shear-thinning properties, where the viscosity decreases with increasing shear-rate. The mechanism behind this is assumed to be related to the alignment and entanglement of the macromolecules and the formation of weak bonds or cross-linking [52]. The Navier-Stokes equations can be modified to incorporate this effect by assuming that the viscosity η is not constant, but depends rather on the

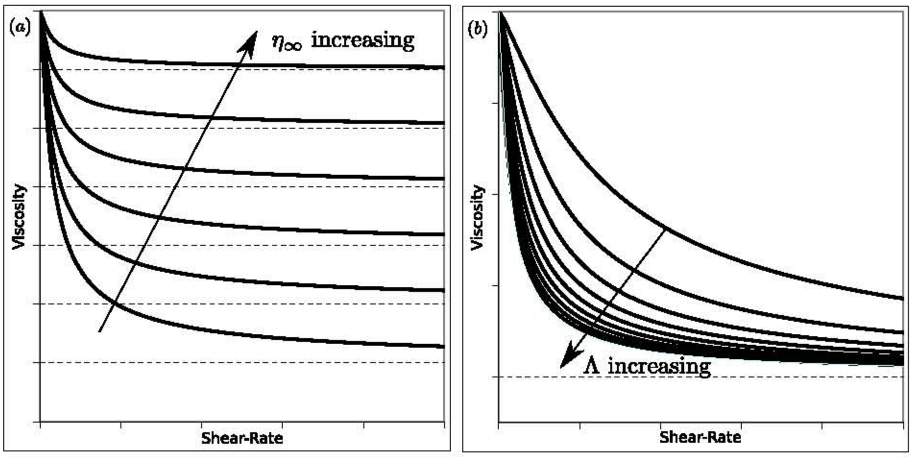

Figure 2.2. – The dependence of the Carreau-Yasuda viscosity function on internal parameters. (a) Dependence on varying η_∞. (b) Dependence on varying Λ.

principal invariants of the deviatoric stress, i.e. $\eta \to \eta(\dot\gamma)$ where $\dot\gamma$ is the "shear-rate" defined as

$$\dot\gamma = \sqrt{\frac{1}{2}\dot{\boldsymbol\gamma} : \dot{\boldsymbol\gamma}}. \tag{2.14}$$

Carreau-Yasuda Viscosity Function

Many models exist in the literature to describe the relationship between the shear-rate and viscosity (see [10] pg 208 for a comprehensive list of viscosity models). Many of these relationships are empirically based. In this work we focus on the Carreau-Yasuda viscosity model

$$\eta(\dot\gamma) = \eta_\infty + (\eta_0 - \eta_\infty)\left\{1 + (\Lambda\dot\gamma)^a\right\}^{\frac{n-1}{a}} \tag{2.15}$$

which is a generalization of the original Carreau Model [20].

This model is characterized by five parameters which are fitted from experiments for each material. The advantage of this model is that it *smoothly* moves between two asymptotic values, namely: η_0 the zero-shear viscosity and η_∞ the infinite-shear viscosity. This is important as it ensures a continuous derivative, which is essential when linearizing with a Newton-Raphson scheme. The difference between η_0 and η_∞ dictates the amount of variability in the viscosity (as seen in figure 2.2 (a)) while the remaining parameters control the offset, slope and other features. For example in figure 2.2 (b) the influence of increasing the parameter Λ is shown with all other parameters held constant.

Thixotropy

The discussion above considered an immediate response of viscosity to shear-rate. However, for many materials these relationships may only be applied to steady flows. Typically these materials require a finite time for the viscosity to change and hence the above generalized Newtonian models may offer only a crude approximation in the unsteady case. This process is referred to as *thixotropy,* or work-softening, where the viscosity will decrease with time under constant shear-rate. This arises from the time required for the constitutive molecules to form networks. Although relaxation features are usually associated with viscoelasticity, thixotropy is an independent phenomenon featuring in both elastic and inelastic flows. A very recent review of this topic may be found in Mewis and Wagner [63].

2.4. Viscoelasticity

The presence of macromolecules in most real life fluids, albeit in small concentrations, introduces additional material properties. Particularly long molecular chains in polymeric fluids may absorb and release elastic energy in their bonds. These long molecular chains differ greatly from the rigid point-like approximations in Newtonian fluids. When present in a solvent there exists an interplay between elastic and viscous forces which renders the material *viscoelastic*. As may be expected, these materials behave somewhere between a Hookean solid and a Newtonian fluid. The extent to which fluids are viscoelastic may be characterized by their *relaxation* and *retardation* times.

The *relaxation* time refers to the time scale in which the stress reduces to zero under the imposition of a constant strain. Consider this in relation to an elastic solid which experiences a constant stress under a constant strain and a viscous fluid which experiences zero stress under the same conditions. On the other hand, the *retardation* time refers to the time scale in which under an imposed stress the strain rate grows to its asymptotic constant value. An elastic solid would exhibit an immediate constant strain, while a viscous fluid would exhibit unbounded linear growth in strain, i.e. constant strain-rate. These concepts are illustrated in figure 2.3 where the behaviour of viscoelastic materials relative to behaviour of elastic solids and viscous fluids can be more easily seen. This finite response time in viscoelastic fluids is typically characterized as a “fading” memory.

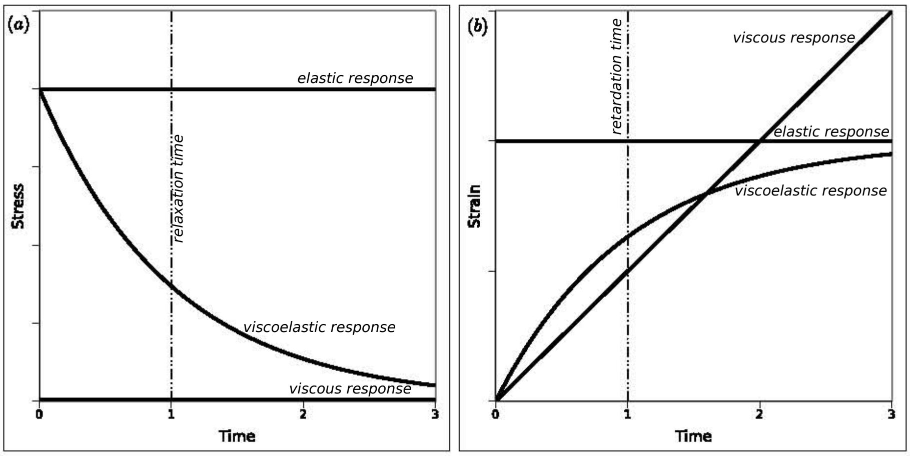

Figure 2.3. – Response of a linear viscoelastic fluid to a suddenly imposed (a) strain and (b) stress, as compared to purely viscous and elastic responses.

To fully describe the behaviour and dynamics of these fluids we require a material constitutive equation to describe the evolution of the stress relative to the deformation gradient. We proceed by first introducing a class of linear viscoelastic models in section §2.4.1. Although these models are relevant for only small deformations, they provide a good basis for extension to differential nonlinear models, and in particular the Oldroyd-B model as shown in section §2.5.

2.4.1. Linear Viscoelastic Models

The simplest linear viscoelastic models may be viewed as generalizations of 1D systems of dashpots and springs to represent the viscous and elastic contributions to the material function. The simplest of this class of models is Maxwell's model, which may be represented in 1D as shown in figure 2.4.

In figure 2.4 (a) the dashpot represents the viscous stress response. In 1D, the force F and rate of extension $\frac{\mathrm{d}x}{\mathrm{dt}}$ are linearly related by the viscosity η. This may be generalized to higher dimensions as

$$F = -\eta \frac{\mathrm{d}x}{\mathrm{dt}} \to \boldsymbol{T} = -\eta \dot{\boldsymbol{\gamma}}(t), \tag{2.16}$$

where $\boldsymbol{T}$ is the stress tensor and $\dot{\boldsymbol{\gamma}}$ is the rate-of-strain tensor.

Similarly, in figure 2.4 (b) the spring represents the elastic response where the force F and extension are linearly related by the elasticity modulus G. When extended in this instance the stress is related to the strain tensor $\boldsymbol{\gamma}$ as

$$F = -Gx \to \boldsymbol{T} = -G\boldsymbol{\gamma}(t). \tag{2.17}$$

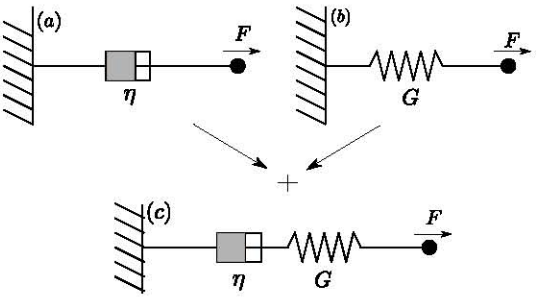

Figure 2.4. – Mechanical representation of Maxwell's model. (a) Single dashpot representing a viscous material. (b) Single spring representing an elastic material. (c) Series combination of dashpot and spring representing a Maxwell viscoelastic fluid.

The simplest combination of these elements is shown in figure 2.4 (c), consisting of one spring and dashpot in series and is referred to as Maxwell's model. Since the stress in each element is the same, and the extension may be expanded over each element, we may then combine (2.16) and (2.17) to arrive at the constitutive Maxwell relation

$$\boldsymbol{T} + \lambda \frac{\partial \boldsymbol{T}}{\partial t} = -\eta \dot{\gamma}(t), \tag{2.18}$$

where $\lambda = \eta / G$ is the relaxation time of the material.

Many other models of this class exist, which may be viewed as different combinations of springs and dashpots in series and parallel. One such instance is the Kelvin model, consisting of a spring and dashpot in parallel. A particularly useful member of this class is Jeffrey's model, represented in figure 2.5. This is an important model as it incorporates both relaxation and retardation times and will be used as a starting point to extension to more general nonlinear models.

The constitutive equation for Jeffrey's model may be easily derived as

$$T + \lambda_1 \frac{\partial \boldsymbol{T}}{\partial t} = -\eta(\dot{\gamma} + \lambda_2 \frac{\partial \dot{\gamma}}{\partial t}), \tag{2.19}$$

where the parameters relate to the diagram as : $\eta = \eta_1$, $\lambda_1 = (\eta_1 + \eta_2)/G_2$ (the relaxation time) and $\lambda_2 = \eta_2 / G_2$ (the retardation time).

The models presented in this section are all empirically based and apply to small deformations due to their lack of "objectivity". To elaborate: these models apply well to infinitesimal material volumes but they do not take into consideration the motion of these volumes relative to a fixed lab frame. This problem will be tackled in the next section by introducing corotational invariant forms of these models.

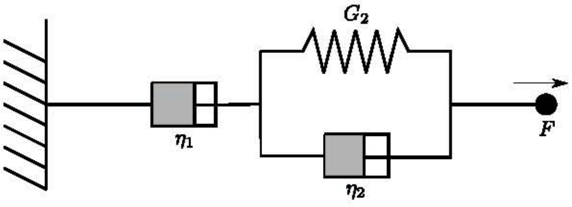

Figure 2.5. – Mechanical representation of Jeffrey's model: a series combination of a dashpot with a parallel spring and dashpot system.

2.4.2. Differential Constitutive Models

Corotational Frames

Consider a material volume at time $t = t$ with coordinate system $\hat{\boldsymbol{X}}(t, t)$, which has the same orientation as the fixed coordinate system $\boldsymbol{X}$ and is offset by the vector $\boldsymbol{b}(t, t)$. Assuming this volume at a previous time $t = t'$ had coordinates $\hat{\boldsymbol{X}}(t, t')$, as shown in figure 2.6, we need to consider the offset and rotation of the coordinate system at later times when taking time derivatives of tensor quantities. This may be seen as a generalization of the material derivative derived in section §2.1. We may relate the coordinate systems at different times by the expression

$$\hat{\boldsymbol{X}}(t, t') = \boldsymbol{\Omega}(t, t')(\hat{\boldsymbol{X}}(t, t) - \boldsymbol{b}(t, t)) + \boldsymbol{b}(t, t'), \tag{2.20}$$

where $\boldsymbol{\Omega}(t, t')$ is the rotation matrix and will depend on the vorticity tensor $\boldsymbol{\omega} = \boldsymbol{\nabla u} - \boldsymbol{\nabla u}^T$.

In order to make the models in section §2.4.1 objective, we need only transform all the *local* derivatives such that they are relative to the fixed *global* frame, i.e. $\frac{\partial}{\partial t}(\cdot) \to \frac{\mathfrak{D}}{\mathfrak{D}t}(\cdot)$, where the latter is referred to as the *Jaumann* derivative and may be expressed as

$$\begin{aligned} \frac{\mathfrak{D}\boldsymbol{T}}{\mathfrak{D}t} &= \boldsymbol{\Omega}\frac{D\boldsymbol{T}}{Dt}\boldsymbol{\Omega}^T \\ &= \frac{D\boldsymbol{T}}{Dt} + \frac{1}{2}\boldsymbol{\omega}\cdot\boldsymbol{T} - \frac{1}{2}\boldsymbol{T}\cdot\boldsymbol{\omega} \end{aligned} \tag{2.21}$$

where $\frac{\mathrm{D}}{\mathrm{D}t}(\cdot)$ again denotes a material derivative.

Corotational Jeffrey's Model

By replacing the local derivatives in the Jeffrey's model constitutive equation with Jaumann derivatives, this renders the model "objective" with a constitutive equation given by

$$\boldsymbol{T} + \lambda_1\frac{\mathfrak{D}\boldsymbol{T}}{\mathfrak{D}t} = -\eta\left(\dot{\gamma} + \lambda_2\frac{\mathfrak{D}\dot{\gamma}}{\mathfrak{D}t}\right). \tag{2.22}$$

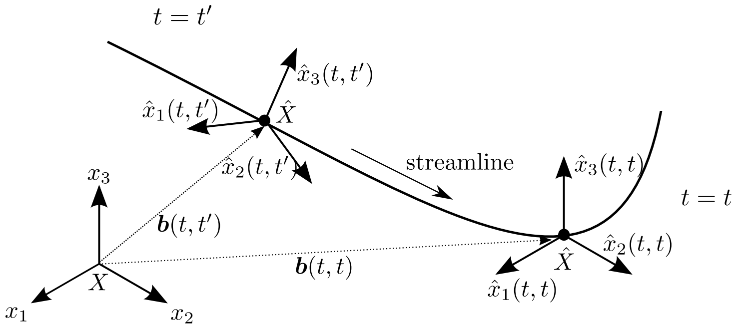

Figure 2.6. – The rotation and translation of a Lagrange coordinate system relative to a fixed Eulerian frame of reference.

It was however shown that this model was still not sufficient to describe many rheological observed phenomena (see [10]). This led Oldroyd [67] to introduce certain modifications to this model which eventually led to development of the much used Oldroyd 8-constant series of models.

2.5. The Oldroyd-B Model

The modifications proposed by Oldroyd consisted of adding all quadratic terms in $\dot{\boldsymbol{\gamma}}$ and $\boldsymbol{T}$ to (2.22), weighted by various constants. The particular choice of constants led to a particular choice of Oldroyd model; the most popular of which is the Oldroyd-B model, expressed as

$$\begin{aligned}\boldsymbol{T} + \lambda_1 \frac{\mathfrak{D}\boldsymbol{T}}{\mathfrak{D}t} - \frac{1}{2}\lambda_1 \left(\dot{\boldsymbol{\gamma}} \cdot \boldsymbol{T} + \boldsymbol{T} \cdot \dot{\boldsymbol{\gamma}}\right) &= -\eta(\dot{\boldsymbol{\gamma}} + \lambda_2 \frac{\mathfrak{D}\dot{\boldsymbol{\gamma}}}{\mathfrak{D}t} - \lambda_2 \dot{\boldsymbol{\gamma}} \cdot \dot{\boldsymbol{\gamma}}) \\ \Rightarrow \boldsymbol{T} + \lambda_1 \overset{\triangledown}{\boldsymbol{T}} &= -\eta(\dot{\boldsymbol{\gamma}} + \lambda_2 \overset{\triangledown}{\dot{\boldsymbol{\gamma}}}). \qquad (2.23)\end{aligned}$$

In (2.23), $\overset{\triangledown}{(\cdot)}$ denotes the *Oldroyd* or upper-convected derivative, defined as

$$\overset{\triangledown}{(\cdot)} = \frac{\mathrm{D}}{\mathrm{D}t}(\cdot) - (\boldsymbol{\nabla u}) \cdot (\cdot) - (\cdot) \cdot (\boldsymbol{\nabla u})^T. \qquad (2.24)$$

2.5.1. Non-Dimensional Form

Numerical treatment of viscoelastic problems, and fluid problems in general, is typically performed within a dimensionless formulation that ensures that all variables have roughly the same order of magnitude. This requires that the governing equations are transformed into their non-dimensional forms. We begin by splitting the viscosity η into a solvent Newtonian η_s and polymeric η_p contribution, expressed as

$$\eta = \eta_s + \eta_p. \tag{2.25}$$

The deviatoric stress may then be decomposed into a Newtonian and polymeric part similarly: $\boldsymbol{T} = \eta_s \dot{\boldsymbol{\gamma}} + \boldsymbol{\tau}$. The polymeric contribution $\boldsymbol{\tau}$ is referred to as the extra stress. The first dimensionless number we introduce is $\beta = \lambda_2/\lambda_1$ corresponding to the ratio of retardation and relaxation times and simultaneously the fraction of solvent to total viscosity $\beta = \eta_s/\eta$. It then follows that $\eta_p = (1-\beta)\eta$. With this definition we simplify the momentum and continuity equation (2.13) and the constitutive equation (2.23) to form the governing set of equations for the Oldroyd-B model in a bounded domain $\Omega \subset \mathbb{R}^2$ or $\mathbb{R}^3$ with Lipschitz boundary $\partial\Omega$:

$$\begin{aligned} \rho\left(\frac{\partial \boldsymbol{u}}{\partial t} + \boldsymbol{u}\cdot\boldsymbol{\nabla}\boldsymbol{u}\right) + \boldsymbol{\nabla}p - \beta\,\eta\nabla^2\boldsymbol{u} - \boldsymbol{\nabla}\cdot\boldsymbol{\tau} &= \boldsymbol{0}, \\ \boldsymbol{\nabla}\cdot\boldsymbol{u} &= 0, \\ \boldsymbol{\tau} + \lambda_1\overset{\nabla}{\boldsymbol{\tau}} - (1-\beta)\,\eta\,\dot{\boldsymbol{\gamma}} &= \boldsymbol{0}. \end{aligned} \tag{2.26}$$

For the problem to be well posed, initial values for the velocity field $\boldsymbol{u}_0 : \Omega \to \mathbb{R}^2$ or $\mathbb{R}^3$ and extra-stress field $\boldsymbol{\tau}_0 : \Omega \to \mathbb{R}^2$ or $\mathbb{R}^3$ are required throughout the domain. Furthermore, we assume the boundary may be decomposed into two segments $\partial\Omega = \Gamma_{\mathrm{D}} \cup \Gamma_{\mathrm{N}}$, such that $\Gamma_{\mathrm{D}} \cap \Gamma_{\mathrm{N}} = \emptyset$ and essential or Dirichlet boundaries for $\boldsymbol{u}$ are set along Γ_{D} and natural or Neumann boundaries are set along Γ_{N}. Lastly, inflow boundary conditions are required for $\boldsymbol{\tau}$ along the inflow boundary $\Gamma_{\mathrm{IN}} = \partial\Omega \cup \{\boldsymbol{u}\cdot\boldsymbol{n}|_{\partial\Omega} < 0\}$, where $\boldsymbol{n}$ is the outward normal to $\partial\Omega$.

The fields, primitive variables and operators are then cast into dimensionless forms, designated by a tilde over the symbol. This is done by scaling these quantities with intuitive characteristic values, expressed as

$$\tilde{\boldsymbol{u}} = \frac{\boldsymbol{u}}{U}, \quad \tilde{\boldsymbol{x}} = \frac{\boldsymbol{x}}{L} \to \tilde{\boldsymbol{\nabla}} = L\nabla, \quad \widetilde{t} = \frac{t}{T} = \frac{t}{L/U}. \tag{2.27}$$

Here U is the characteristic velocity, L the characteristic length and T is the characteristic time which is derived from the previous two values. Additionally we scale the pressure and extra stress by a common factor as

$$\tilde{p} = \frac{p}{(U/L)\eta}, \quad \tilde{\boldsymbol{\tau}} = \frac{\boldsymbol{\tau}}{(U/L)\eta}. \tag{2.28}$$

Substituting (2.27) and (2.28) into (2.26) yields the dimensionless form of the Oldroyd-B system in the absence of any body forces:

$$\begin{aligned} \mathrm{Re}\,\frac{\mathrm{D}\boldsymbol{u}}{\mathrm{D}t} + \boldsymbol{\nabla} p - \beta\,\nabla^2 \boldsymbol{u} - \boldsymbol{\nabla}\cdot\boldsymbol{\tau} &= \boldsymbol{0}, \\ \boldsymbol{\nabla}\cdot\boldsymbol{u} &= 0, \\ \boldsymbol{\tau} + \mathrm{We}\,\overset{\triangledown}{\boldsymbol{\tau}} - (1-\beta)\,\dot{\boldsymbol{\gamma}} &= \boldsymbol{0} \end{aligned} \tag{2.29}$$

where we have introduced two dimensionless numbers: $\mathrm{Re} = \frac{\rho U L}{\eta}$ - the Reynolds number and $\mathrm{We} = \frac{\lambda_1}{L/U}$ - the Weissenberg number[2]. The Reynolds number is an important quantity in fluid mechanics and denotes the ratio of inertial to viscous forces in the fluid. The Weissenberg number is related to the relaxation time of the viscoelastic fluid.

2.5.2. Alternative Derivation

To arrive at the Oldroyd-B constitutive equation equation (2.29), we began with a rather naive model of the continuum *viz.* a combination of dashpots and springs. However it may be shown that by developing the model from a more natural description on a molecular level, the same continuum model may be acquired.

We approximate the material by an ensemble of Hookean dumbbells suspended in a Newtonian solvent. A representative dumbbell is shown in figure 2.7. This approximates the long molecules by their end points and the elasticity in their bonds by the connecting spring. By considering the hydrostatic forces on the beads, elastic forces from the spring as well as Brownian forces due to the small scale, when ensemble averages are taken the same evolution equation for the extra stress is obtained (see [70] pg. 34 for additional details).

This is clearly a more physically realistic setting and additionally provides a more intuitive interpretation of the extra stress. In figure 2.7, the end-to-end vector of the dumbbell is denoted as $\boldsymbol{q} = \boldsymbol{r_2} - \boldsymbol{r_1}$. Since this is a statistical variable, we denote by $\langle \boldsymbol{q} \otimes \boldsymbol{q} \rangle$ the ensemble averaged second moment at any point in space and time. The extra stress is

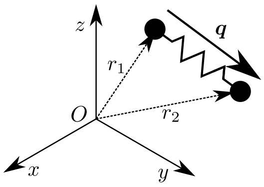

Figure 2.7. – Representative dumbbell of kinetic description of the Oldroyd-B model.

---

[2] Note we have dropped the tilde in this and all following equations and we assume all fields are dimensionless from this point onwards

linearly related to this quantity and thus corresponds to the amount as well as the direction of stretching of the "molecular" dumbbells. This interpretation is most directly used when the problem is reformulated in terms of the conformation tensor (section §2.5.3) and is particularly useful in the context of stability analysis (see section §2.8).

2.5.3. Conformation Tensor

The conformation tensor $\boldsymbol{\sigma}$ is defined as

$$\boldsymbol{\sigma} \quad = \quad \frac{\mathrm{We}}{1-\beta}\boldsymbol{\tau} + \boldsymbol{I} \tag{2.30}$$

and as stated above is equivalent to the second moment of the dumbbell end-to-end statistical vector, i.e.

$$\boldsymbol{\sigma} = \langle \boldsymbol{q} \otimes \boldsymbol{q} \rangle \,. \tag{2.31}$$

Due to this definition it inherits certain favourable properties, such as symmetry and positive-definiteness.

These properties have made it an attractive variable to work with in numerous studies [44, 64, 15] where the focus was placed on the stability of the system. These works presented some important theoretical results concerning the preservation of the positive-definiteness of the conformation tensor. Numerically, the loss of positive-definiteness of the approximate conformation tensor has been shown to act as an early indicator for the onset of numerical instability; typically consisting of an unbounded growth in solutions. When the model is extended to a generalized form, i.e. $1-\beta$ becomes variable, the conformation tensor becomes inconvenient to work with and hence the numerics in this work are all performed with respect to the original extra-stress tensor.

2.5.4. Boger Fluids

The Oldroyd-B model describes a viscoelastic fluid with constant viscosity, however most real fluids do exhibit some form of shear-rate-dependent viscosity. This seems to render the Oldroyd-B model too simplistic to fully represent any real material. There exists a class of fluids called Boger fluids, initially created by David Boger in the 1970s which possess both elastic and viscous properties but exhibit nearly constant viscosity. This class of fluids is sufficiently described by the Oldroyd-B model and typically consist of very dilute polymer suspensions in a Newtonian solvent. They are interesting to study as they decouple the effects of elasticity and viscosity. A short introduction to this class of fluids may be found in the review by James [49].

2.6. Alternative Viscoelastic Models

The validity and applicability of the Oldroyd-B model has been discussed thoroughly in the literature and although it provides reasonable predictions for Boger fluids in shear flow, it produces spurious results when considering extensional flows. In the latter instance, the model predicts unbounded growth in stress by assuming that the dumbbells may stretch infinitely. There exists in the literature a vast collection of viscoelastic models with varying degrees of complexity and scope, where in particular the issue raised above has been accounted for in many of these models. A brief overview of some popular viscoelastic models are presented below for completeness:

- **Oldroyd 8-Constant Models**
  This class of eight models are obtained by setting different values for weightings in the additional terms in (2.29), as discussed in section §2.5. The Oldroyd-B model is a particular instance of this class with other popular viscoelastic models derived in a similar fashion. These include the Upper Convected Maxwell (UCM) model (which has no solvent viscosity) and the Johnson-Segalman model.

- **FENE (Finitely Extensible Nonlinear Elastic) Dumbbell Model**
  This model seeks to counter the infinite extensibility of the dumbbells by modifying the potential of the spring to be neo-Hookean with a finite extensibility. A similar differential constitutive equation to the Oldroyd-B model is obtained, with additional nonlinear terms.

- **PTT (Phan-Thien-Tanner) Model**
  This is a nonlinear model, as developed in [74], based on network theory and has been shown to predict well the elongational properties of polymer solutions.

Highly concentrated polymer melts are typically dealt with by integral based constitutive equations such as the Kaye-BKZ model and Curtis-Bird model. These are based on polymer network theories which fall outside the scope of this work (see [11] for a brief overview).

Typically polymeric fluids have a large range of constitutive molecules which form a spectrum of relaxation and retardation times. These are referred to as multi-modal fluids. This spectrum of relaxation times is normally taken into account by considering linear combinations of each model with respect to a range of parameters. This renders obtaining numerical solutions for these fluids very expensive. Only fluids with a single relaxation time will be considered in this work.

2.7. The Generalized Oldroyd-B Model

2.7.1. Modeling Blood Flow

Blood is a complex biological material which has been shown to exhibit both non-Newtonian (shear-thinning) and viscoelastic properties. Although much of the discussion on this will be reserved for chapter 7, it was in seeking to better describe blood flow that the generalized Oldroyd-B (GOB) model was proposed by Yeleswarapu [91]. This model was proposed on an empirical basis, after it was shown to better fit experimental results. The GOB model is effectively a modified Oldroyd-B model where the viscosity is replaced with a function of shear-rate: that is

$$\eta(\dot{\gamma}) = \eta_\infty + (\eta_0 - \eta_\infty)\left\{\frac{1 + \ln(1 + \Lambda\dot{\gamma})}{1 + \Lambda\dot{\gamma}}\right\} \tag{2.32}$$

and where the solvent viscosity is assumed as constant. This is by no means the only possible generalization of the Oldroyd-B model, and other viscosity functions such as the Carreau-Yasuda (2.15) may be used in place of (2.32).

2.7.2. Dimensionless Form

Obtaining a dimensionless form for the generalized Oldroyd-B equations follows similarly to the classical model, and hence most details will be omitted with only the differences between the two derivations presented. In this work we focus on the shear-thinning case and hence the characteristic viscosity is chosen as η_0 (the value at zero shear-rate). The Reynolds number is redefined as $\mathrm{Re} = \rho U L/\eta_0$ and the dimensionless solvent viscosity similarly as $\beta = \eta_s/\eta_0$. Since $\eta_p(\dot{\gamma}) = \eta(\dot{\gamma}) - \eta_s$ we may define the dimensionless polymeric viscosity as

$$\begin{aligned} \tilde{\eta_p}(\dot{\gamma}) &= \eta(\dot{\gamma})/\eta_0 - \eta_s/\eta_0 \\ &= (\alpha - \beta) + (1 - \alpha)\phi(\dot{\gamma}), \end{aligned} \tag{2.33}$$

where $\alpha = \eta_\infty/\eta_s$ is the ratio of infinite shear-rate to zero shear-rate viscosity and $\phi(\dot{\gamma})$ is the functional form of the specific viscosity function. The parameter α represents the extent of shear-thinning in the system, with $\alpha = 1$ reducing the model to the classical Oldroyd-B form. A natural constraint $\alpha > \beta$ emerges that ensures that both polymeric and solvent viscosities remain positive.

With these new definitions we may now obtain the dimensionless form of the GOB equations. These differ from (2.29) only in that $(1 - \beta)$ in the constitutive equation is replaced with $\tilde{\eta_p}(\dot{\gamma})$. From this point onwards the tilde will be dropped from this quantity without fear of confusion, as all variables are assumed dimensionless. For the GOB model, the conformation tensor (2.30) may be redefined, following [64], as

$$\boldsymbol{\sigma} = \frac{\mathrm{We}}{\eta_p(\dot{\gamma})}\boldsymbol{\tau} + \boldsymbol{I}. \tag{2.34}$$

2.8. The High Weissenberg Number Problem (HWNP)

As was discussed in the introduction, the HWNP is the observed phenomenon that all numerical schemes diverge or fail at high values of the We number. However, as discussed in Keunings [55], the source of this problem is most likely numerical in nature. It is thus important for any successful numerical scheme to have a firm theoretical basis on the stability of the method and to also provide some quantification of this stability.

In Boyaval *et.al.* [15] some important results were derived with respect to this issue. Most importantly, it was shown that for the continuous problem if $\boldsymbol{\sigma}\,(t=0)$ is a symmetric positive-definite tensor, which acts as an initial condition for the problem defined by the Oldroyd-B governing equations (2.29), then this property will propagate in time assuming that homogeneous Dirichlet boundary conditions are applied on all boundaries and no forcing terms are present. It was this result which allowed a consistent definition of a free energy as

$$E_1(t) = \int\limits_{\Omega} \left\{ \frac{\mathrm{Re}}{2} \left\| \boldsymbol{u} \right\|^2 + \frac{1-\beta}{\mathrm{We}^2} \mathrm{tr}\left(\boldsymbol{\sigma} - \ln(\boldsymbol{\sigma}) - \boldsymbol{I} \right) \right\} \mathrm{d}\Omega. \tag{2.35}$$

The above properties of the conformation tensor ensure that the energy density is non-negative throughout the domain and for all time, and furthermore that $\ln(\boldsymbol{\sigma})$ is well defined.

This free energy may be interpreted as having a traditional kinetic term $1/2\mathrm{Re}\left\|\boldsymbol{u}\right\|^2$ and an entropic term depending on the conformation tensor, related to the orientations of the elastic dumbbells. The stability of the system was then guaranteed by showing the dissipation of the defined free energy E_1. These results for the continuous case were then carried over to a discrete approximation, based on a finite element method. It was then shown that a piecewise-constant approximation for the extra stress would allow for a similar dissipation of the discrete free energy. These arguments were also extended to handle more general constant boundary conditions, where it was shown that the energy would asymptote to a constant value.

2.8.1. Extension to the General Model

The arguments above were later extended to include the generalized Oldroyd-B model in Mohamed and Reddy [64]. Due to relevance of this study to our work we will present a brief overview of some of the relevant results in this section.

In [64] the arguments presented followed that of Boyaval *et.al.* [15] by first expressing the governing equations in terms of the newly proposed conformation tensor (2.34), which yielded the system

$$\begin{aligned} \mathrm{Re}\,\frac{D\boldsymbol{u}}{Dt} - \beta\,\nabla^2\boldsymbol{u} + \boldsymbol{\nabla} p - \boldsymbol{\nabla}\cdot\boldsymbol{\sigma} - \frac{1}{\mathrm{We}}\,\boldsymbol{\nabla}\eta_p\left(\dot{\gamma}\right) &= \boldsymbol{f}, \\ \boldsymbol{\nabla}\cdot\boldsymbol{u} &= 0, \\ \zeta\,\boldsymbol{\sigma} + \overset{\nabla}{\boldsymbol{\sigma}} &= \zeta\,\boldsymbol{I} \end{aligned} \tag{2.36}$$

where ζ was defined as

$$\zeta = \frac{1}{We} + \frac{D}{Dt}\ln\mu_p\left(\dot{\gamma}\right). \tag{2.37}$$

Although this formulation is convenient for theoretical arguments, it is inconvenient to deal with numerically. This is mostly due to the presence of ζ, which introduces higher order spatial derivatives for the velocity field and additional time derivatives. For these reasons we will perform our numerical work within the original $\boldsymbol{\tau}$ formulation and later translate our results into the conformation tensor for comparison.

Two analogous results to [15] were then obtained for the generalized Oldroyd-B system, concerning the propagation of the positive-definiteness of the conformation tensor. However, the presence of non-constant viscosity introduced an additional constraint to ensure this propagation. These theorems are presented below, where the second theorem is a stricter form of the first:

1. If $\boldsymbol{\sigma}\left(t=0\right)$ is sufficiently smooth and symmetric positive-definite and $\zeta(x,t) > 0$ $\forall x \in \Omega$ and $t \in \mathbb{R}^+$ then $\boldsymbol{\sigma}(t)$ will remain symmetric positive-definite $\forall t \in \mathbb{R}^+$
2. If $\boldsymbol{\sigma}\left(t=0\right)$ is sufficiently smooth and symmetric positive-definite and $\det\left(\boldsymbol{\sigma}\left(t=0\right)\right) > 1$, then for sufficiently small $\zeta(x,t) > 0$ $\forall x \in \Omega$ and $t \in \mathbb{R}^+$ then $\boldsymbol{\sigma}(t)$ will remain symmetric positive-definite and $\det\left(\boldsymbol{\sigma}(t)\right) > 1$ $\forall t \in \mathbb{R}^+$

By using the second theorem it was then possible to define the energy functional

$$E_2(t) = \int_\Omega \left\{\frac{\mathrm{Re}}{2}\left\|\boldsymbol{u}\right\|^2 + \mathrm{tr}(\boldsymbol{\tau})\right\} \mathrm{d}\Omega \tag{2.38}$$

written in terms of the $\boldsymbol{\tau}$ variable. Under the conditions of the second theorem this energy is well defined and additionally shown to be dissipative. Under only the conditions of the first theorem a different energy functional was defined, which was also shown to be dissipative.

Although the requirement in the second theorem that ζ be sufficiently small may be difficult to apply in practice, the condition $\zeta > 0$ has clear implications on the parameter values and flow field. Using the definition of ζ (2.37), this constraint may be expressed as a bound on the We number as

$$\mathrm{We} \quad < \quad \frac{(\max_{\Omega,t}\{G_0(\dot{\gamma})\})^{-1}}{\Lambda \max_{\Omega,t}\{\left|\frac{D\dot{\gamma}}{Dt}\right|\}} \tag{2.39}$$

where the function $G_0(\dot{\gamma})$ is derived for the particular applied viscosity function. For the Carreau-Yasuda function this may be explicitly written as

$$G_0 \quad = \quad (1-n)\Lambda^a \frac{\dot{\gamma}^{a-1}}{(1+(\Lambda\dot{\gamma})^a)}. \tag{2.40}$$

Since the bound on We is dependent on the flow field it may not be possible to determine an a-priori limit to guarantee a stable solution. It is however possible to determine the validity and stringency of this constraint numerically during a simulation. This is the approach that we will follow in section §6.2, where we investigate whether this condition is valid in the discrete setting. Furthermore it is not clear how strong or stringent the constraint may be, which is a question that could potentially be investigated with numerical work.

2.9. Numerical Solutions

Following the definition of our model and discussion on the free-energy dissipative properties of the OB and GOB systems, we turn our attention now to obtaining numerical solutions for these models. We follow the work presented in Boyaval *et.al.* [15], who showed that the dissipative free-energy properties for the continuous system carry over to the discrete solution when using a mixed finite element method with piecewise-constant approximations for the extra stress and stabilization of the constitutive equation through a DG-upwinding method. In the next chapter we will focus on the finite element method and the way in which it applies to the GOB system.

Part II.

Numerical Work

3. The Finite Element Method

The finite element method is a popular and extensively studied technique within the numerical community. The literature for this method is quite extensive. The books of Hughes [45], Fish and Belytscheko [35] and Zienkiewicz [95] are good introductory texts on the principles, theory and implementation of the finite element method.

As an overview to the finite element method: we may simply view it is a spatial approximation technique used to solve partial differential equations on arbitrary domains. The process consists of breaking up these domains into a finite number of sub-domains over which polynomials are used to interpolate the solution fields. The equations are rewritten in a weak, or variational, formulation from which when combined with the finite dimensional approximation spaces, a set of linear equations arise. Once solved, these polynomial interpolations may be used in reverse to provide an approximation of the solution field throughout the domain.

More details about each of these processes are presented in the sections that follow, along with the application of finite elements to the generalized Oldroyd-B model.

3.1. Introductory Theory

The principles of finite elements are most easily explained when considering the prototypical scalar Poisson problem, stated in its *strong* form as

$$-\nabla^2\phi = f \ \ \forall x \in \Omega, \qquad \phi|_{\Gamma_D} = g, \quad \frac{\partial \phi}{\partial n}|_{\Gamma_N} = h. \tag{3.1}$$

This boundary value problem is defined over a domain Ω whose boundary $\partial\Omega$ can be decomposed into two non-intersecting segments Γ_D and Γ_N, i.e. $\partial\Omega = \Gamma_D \cup \Gamma_N$ and $\Gamma_D \cap \Gamma_N = \emptyset$, along which essential (Dirichlet) boundary and natural (Neumann) boundary conditions are set respectively.

3.1.1. Weak Formulation

As mentioned above, the finite element method provides approximate solutions to equations in a *weak* or variational formulation, which has less restriction on the smoothness of solutions. Prior to introducing this formulation we define the space of admissible functions $\mathcal{S}(\Omega) = \{\phi \in H^1(\Omega) \mid \phi|_{\Gamma_D} = g\}$ as the *trial* space, where $H^1(\Omega)$ denotes the first Sobolev space[1]. Additionally we define the space of weighting functions $\mathcal{V}_0(\Omega) = \{\varphi \in H^1(\Omega) \mid \varphi|_{\Gamma_D} = 0\}$, also known as the *test* space. The weak form can then be formulated by multiplying (3.1) by an arbitrary weight function $\varphi \in \mathcal{V}_0(\Omega)$ and integrating over the entire domain to yield

$$-\int_\Omega \nabla^2\phi\,\varphi\,\mathrm{d}\Omega \;=\; \int_\Omega f\varphi\,\mathrm{d}\Omega. \tag{3.2}$$

Integration by parts is then performed on the first term in (3.2), which reduces the order of the derivative and additionally introduces the natural boundary conditions through the boundary integral. The resulting variational formulation is then:

- Find $\phi \in \mathcal{S}(\Omega)$ such that (3.3) is true.

$$\int_\Omega \boldsymbol{\nabla}\phi \cdot \boldsymbol{\nabla}\varphi\,\mathrm{d}\Omega - \int_{\Gamma_n} h\varphi\,\mathrm{d}\Omega = \int_\Omega f\varphi\,\mathrm{d}\Omega \quad \forall\varphi \in \mathcal{V}_o(\Omega) \tag{3.3}$$

Note that due to the definition of $\mathcal{V}_0$ the boundary terms on the Dirichlet boundaries are exactly zero. The requirements that $\mathcal{S} \subset H^1$ and $\mathcal{V}_0 \subset H^1$ are lesser requirements than expected of solutions of (3.1) as only first derivatives are present in (3.3).

3.1.2. Galerkin Approximation

To obtain numerical approximations to the solution of (3.3), we may approximate the infinite dimensional test and trial spaces with finite dimensional spaces, i.e. $S \to \mathcal{V}^h$ and $\mathcal{V}_0 \to \mathcal{V}_0^h$, where $\mathcal{V}^h \subset \mathcal{S}$ and $\mathcal{V}_0^h \subset \mathcal{V}_0$. These spaces are constructed by discretizing the domain Ω into a finite number of non-overlapping sub-domains or *elements* $\{\Omega_e\}$. This forms the mesh $\mathcal{T}_h$, where h denotes the characteristic discretization size. This is equivalently stated as

$$\Omega = \bigcup_{e\in\mathcal{T}^h} \Omega_e \text{ and } \Omega_e \cap \Omega_f = \emptyset \;\; \forall e, f \in \mathcal{T}^h,\; e \neq f. \tag{3.4}$$

The trial and test functions are then approximated by members of these finite dimensional spaces, i.e. $\phi \to \phi^h$ and $\varphi \to \varphi^h$. The Galerkin approximation consists of using the same

---

[1] Generally speaking $H^m(\Omega)$, the m^{th} Sobolev space, denotes the space of functions $f : \Omega \to \Re$ which are square-integrable and additionally whose derivatives up to, and including, order m are also square-integrable over the domain Ω

space for both these functions. This requires that the trial function is decomposed as $\phi^h = \phi_0^h + g^h$, where $\phi_0^h \in \mathcal{V}_0^h$ and $g^h|_{\Gamma_D} = g$ and hence maintains the correct Dirichlet boundary conditions. Substituting this decomposition and approximate functions into (3.3) yields the discrete weak formulation:

- Find $\phi_0^h \in \mathcal{V}_0^h$ such that (3.5) holds.

$$\int\limits_{\Omega} \boldsymbol{\nabla}(\phi_0^h + g^h) \cdot \boldsymbol{\nabla}\varphi^h \, \mathrm{d}\Omega - \int\limits_{\Gamma_N} h\varphi^h \, \mathrm{d}\Omega = \int\limits_{\Omega} f\varphi^h \, \mathrm{d}\Omega \quad \forall \varphi^h \in \mathcal{V}_o^h(\Omega) \tag{3.5}$$

Although additional terms containing g^h arise, these may in practice be ignored with the boundary conditions maintained either with Lagrange multipliers weakly or by setting ϕ^h at the boundary to g^h and condensing out any of the linear equations at these positions. The analysis of variational formulations and finite element methods may typically be done assuming homogeneous Dirichlet boundary conditions without any loss in generality.

The finite-dimensional function spaces $\mathcal{V}^h$ and $\mathcal{V}_0^h$ are spanned by a finite set of basis functions $\{N_i \mid i = 1..n\}$ also referred to as *global shape functions.* These are required to be in $H^1(\Omega)$ for the second order problem (3.1) and to satisfy the essential boundary conditions. Using this basis, we may write any member of these spaces $\phi^h \in \mathcal{V}^h$ as a linear combination of these basis functions, i.e. as

$$\phi_h(x) = \sum_{i=1}^{n} \phi_i N_i(x). \tag{3.6}$$

The solution can then be expressed as a vector $\boldsymbol{\phi} = (\phi_1 ... \phi_n)$, where each component corresponds to the coefficient of the respective global shape function. These coefficients along with the shape functions allow us to determine the field value at any point throughout the domain. The finite element method provides a framework of defining these shape functions relative to the discretization of the domain $\mathcal{T}_h$.

Consider a quadrilateral tessellation of the domain and simultaneously consider the set of nodes $\{\boldsymbol{x}_i \mid i = 1...n\}$ over this domain, where there is a node at least at each intersection of the quadrilateral elements (see figure 3.1 (a)). Additional nodes may also be placed on the midpoints of the edges of each element and at the centroid of each element (see figure 3.1 (b)). The set of basis functions can then be defined relative to this set of nodes and elements. We also define the *local shape functions* $N_i^{(e)}$ as the restriction of the global shape functions associated with the i^{th} node to the element Ω_e as

$$N_i^{(e)} = N_i|_{\Omega_e}. \tag{3.7}$$

The local basis functions are then defined as polynomials over their respective elements, where we additionally require that the resulting global basis functions satisfy the following three requirements, namely:

1. **Continuity**
   The shape function N_i is bounded and continuous. It is often easier to construct these functions to posses this property rather than to attempt to enforce it at a later stage.

2. **Compact Support**
   The shape function N_i is nonzero only over elements which contain or border the node $\boldsymbol{x}_i$.

3. **Kronecker Delta Property**
   The shape functions N_i have the value one at its associated node and is zero at all other nodes, i.e. $N_i(x_j) = \delta_{ij}$ [2].

3.1.3. Local Shape Functions

From the discussion above it remains to define the local shape function $N_i^{(e)}$ with respect to an arbitrary element Ω_e. Initially we consider only nodal shape functions over quadrilaterals in 2D, where the shape functions are constructed using Lagrange polynomials (see section §3.1.5) over a corresponding set of nodes. Two popular elements are: bilinear Q_1 elements, consisting of a node at each vertex as shown in figure 3.1 (a) and biquadratic Q_2 elements, consisting of nine nodes as shown in figure 3.1 (b). The resulting global shape functions are then piecewise polynomials acting as interpolation functions where the components of the solution vector $\boldsymbol{\phi}$ represent the value of the field at each corresponding node.

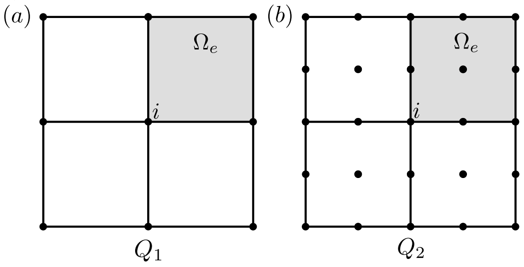

Figure 3.1. – Nodal positions for two prototypical quadrilateral elements: (a) bilinear element Q_1 with 4 degrees of freedom (b) biquadratic element Q_2 with 9 degrees of freedom.

---

[2] The Kronecker Delta function is defined as $\delta_{ij} = \begin{cases} 1 & \text{if } i = j \\ 0 & \text{if } i \neq j \end{cases}$

Using the above definition it is clear that the three properties in section §3.1.2 are satisfied. Firstly, as the shape functions are defined with respect to the set of nodes, which are shared by elements, continuity across element boundaries is ensured. Furthermore, the Lagrange polynomials are both bounded and continuous within each element. The second and third requirement are similarly satisfied by definition.

For the bilinear element: the four degrees of freedom, corresponding to the value of the field at each vertex may equivalently be treated as the coefficients of the four basis monomials $\{1, x, y, xy\}$, which span the space of Q_1 polynomials. Similarly for the biquadratic element, the nine degrees of freedom may be viewed as the coefficients to the nine basis monomials $\{1, x, y, xy, x^2, y^2, x^2y, yx^2, x^2y^2\}$, which span the space of Q_2 polynomials. This treatment does not naturally ensure the continuity of these functions across element boundaries, nor does it naturally ensure that the resulting functions have compact support. Nonetheless, this formulation will be used later in the creation of alternative elements (see section §3.2).

A family of higher-order Q_n elements can be easily constructed by introducing extra nodes on the elements. Additionally, extension to higher dimensions requires only the Cartesian product of the Lagrange polynomials in each dimension. This orthogonality of the coordinates for quadrilateral and hexahedral elements allows for very modular code design.

3.1.4. Isoparametric Mapping

Each element is defined relative to a global coordinate system $\boldsymbol{X} = (x, y)$ via a set of vertices and their order, i.e. figure 3.2 (b). However, it is generally preferable to perform most calculations on an element within a reference frame of a bi-unit square as shown in figure 3.2(a) with coordinate system $\boldsymbol{\xi} = (\xi, \eta)$.

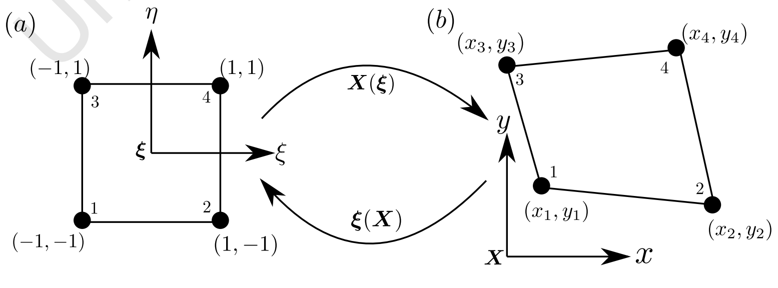

Figure 3.2. – Isoparametric mapping between bi-unit parent cell with coordinates $\boldsymbol{\xi}$ to the real cell with coordinates $\boldsymbol{X}$.

This forms the *parent cell* from which all cells derive and provides a space within which to define shape functions and perform other calculations. In particular the bi-unit square provides an ideal setting for Gauss-Legendre quadrature which is frequently used. The relationship between the reference and real cell is defined by the mapping $\boldsymbol{X}(\boldsymbol{\xi}) : \boldsymbol{\xi} \to \boldsymbol{X}$. An isoparametric mapping is constructed by using the same set of shape functions that define the finite element interpolation, i.e.

$$\begin{pmatrix} x \\ y \end{pmatrix} = \sum_i \begin{pmatrix} x_i \\ y_i \end{pmatrix} N_i^{(e)}(\begin{matrix} \xi \\ \eta \end{matrix}). \tag{3.8}$$

The main advantage of using an isoparametric mapping is that since the mapping of a edge will depend only on the nodal positions on that edge, this ensures that neighbouring cells will map their shared edge to the same curve. A Q_1 mapping, as shown in figure 3.2, will be used for all field variables within this work. This mapping depends only on the vertices of each cell and maps all edges to straight line segments.

3.1.5. Lagrange Polynomials

Lagrange polynomials are frequently used in numerical analysis to interpolate between a set of points. For a set of n points $\{(x_i, y_i) \mid i = 1..n\}$ Lagrange interpolation will provide a unique polynomial of degree $n-1$ passing exactly through all n points. This is performed by creating the set of Lagrange basis polynomials

$$\vartheta_i(x) = \prod_{j \neq i} \left\{ \frac{(x - x_j)}{(x_i - x_j)} \right\} \tag{3.9}$$

over the independent coordinate x_i. Each basis polynomial is by definition unity over its associated point and exactly zero over all others in the set. The interpolation then consists of a linear combination of these basis polynomials, weighted by the corresponding dependent variable y_i. As there exists a unique polynomial of degree $n-1$ passing through n points, the Lagrange basis polynomials provide a method to obtain this unique interpolation function.

These polynomials provide a natural way to extend shape functions to higher dimensions. This is because in the parent frame all coordinates are orthogonal, and hence we may simply take the Cartesian product of the functions in each direction while maintaining the same properties. In 2D this may be written as

$$N_{\mathrm{A}}^{(e)}(\xi, \eta) = \vartheta_{\mathrm{XA}}(\xi)\vartheta_{\mathrm{YA}}(\eta). \tag{3.10}$$

3.1.6. Numerical Solutions

With the definitions of the weak form (3.5) and the shape functions (3.6), we are now able to construct a corresponding linear system of equations. By expanding the functions in (3.5), we obtain the result

$$\sum_i \varphi_i \left\{ \sum_j A_{ij}\phi_j - b_i \right\} = 0,$$

$$\begin{aligned} \text{where } A_{ij} &= \int\limits_{\Omega} \boldsymbol{\nabla} N_i(x) \cdot \boldsymbol{\nabla} N_j(x) \ \mathrm{d}\Omega \\ \text{and } b_i &= \int\limits_{\Gamma_N} h(x) N_i(x) \ \mathrm{d}\Gamma_{\mathrm{N}} + \int\limits_{\Omega} f(x) N_i(x) \ \mathrm{d}\Omega. \end{aligned} \tag{3.11}$$

Since (3.11) must hold for all choices of φ_i, it then follows that the terms in curly brackets are equivalent to zero. Thus by using the notation introduced in (3.11) we arrive at the linear system

$$A\boldsymbol{\phi} = \boldsymbol{b} \tag{3.12}$$

which is solved for the vector of shape function coefficients $\boldsymbol{\phi} = \{\phi_i \mid i = 1...n\}$.

The matrix and right-hand-side vector can be formulated using Gaussian quadrature over the parent cell, as described in section §3.1.4. An advantage of the Galerkin approximation is in the favourable properties of the resulting matrix A. These include sparsity, due to the compact support, near diagonal-dominance and in this instance symmetry. This renders the system appropriate for iterative linear algebra solvers.

3.2. Alternative Elements

The requirements set for potential shape functions in section §3.1.2 may be viewed as slightly flexible, with new elements emerging when one or more of these are disregarded. The Kronecker delta property (3) assumes that shape functions are associated with nodes. However, since shape functions are simply basis polynomials this need not be satisfied.

When using these basis polynomials, maintaining continuity across element boundaries is not automatically guaranteed and in some instance it is not possible to enforce at all. This is the case when linear P_1^{disc} shape functions with basis monomials $\{1, x, y\}$ are chosen over quadrilateral elements. Nonetheless, a large class of methods, referred to as discontinuous Galerkin (DG) methods, which permit discontinuous interpolation functions do exist with numerous advantages and applications.

3.2.1. Discontinuous Galerkin (DG) Methods

The discontinuous Galerkin (DG) method was initially developed by Reed and Hill in 1973 [79] and Lesaint and Raviart in 1974 [58] to solve the neutron transport problem. The lack of continuity across elements was advantageous in that it could easily handle complicated geometries, incorporate h and p type adaptivity and be easily parallizable. More importantly, it was also able to capture discontinuous solutions which arise from certain hyperbolic problems. Furthermore, the method was efficient as it allowed for solutions to be obtained on element-by-element basis. The range of applications was extended as the field matured, as discussed in the review of Cockburn *et.al.* [25]. Most relevantly this includes the work of Fortin and Fortin [37], where DG methods were first used for solving the constitutive equation for viscoelastic flow.

DG methods have also been used to solve elliptic and parabolic problems. Additional stabilization is frequently required when using discontinuous elements, where one such class of such stabilized methods are known as interior penalty (IP) methods. A review of these methods can be found in the work of Arnold *et.al.* [3].

Additional detail on DG methods for upwinding and elliptic problems are also presented in this work in section §4.3 and section §4.6 respectively as they are incorporated into the overall algorithm.

3.3. Vector and Tensor Problems

In the preceding discussion focus was placed on solving a scalar problem in terms of the field ϕ. Finite element methods are also capable of solving vector-valued problems, where each component is treated as a separate field. This often requires a certain amount of bookkeeping and renumbering to ensure that the resulting linear system remains well-conditioned and sparse. Before we proceed, we introduce the following notation: if we consider a vector field $\boldsymbol{v} : \Omega \to \mathbb{R}^d$, where d represents the number of dimensions, we may denote the space of these fields as $\boldsymbol{v} \in [V(\Omega)]^d$. Additionally, it may be required to consider tensor fields $\boldsymbol{\tau}$. In this work we will focus on 2^{nd} rank symmetric tensors. To preserve storage and computation, only unique components of this tensor will be treated, i.e. $\frac{1}{2}d(d+1)$ components. We denote the space of these fields as $\boldsymbol{\tau} \in [S(\Omega)]^{\frac{1}{2}d(d+1)}$.

3.3.1. Mixed Methods

Mixed methods refer to finite element methods where multiple fields are treated as unknowns. A particularly important case of this is the stationary Stokes problem

$$\begin{aligned} -\nabla^2 \boldsymbol{u} + \boldsymbol{\nabla} p &= \boldsymbol{f}, \\ \boldsymbol{\nabla} \cdot \boldsymbol{u} &= 0, \\ \boldsymbol{u}|_\Gamma &= \boldsymbol{0} \end{aligned} \tag{3.13}$$

as discussed in various works (see for example [29]). To ease notation, only homogeneous Dirichlet boundaries will be considered here. The weak form of this system can then be expressed as:

- Find $\boldsymbol{v} \in [\mathcal{V}_0]^d$ and $p \in \mathcal{Q}$ such that (3.14) holds.

$$\begin{aligned} \int_\Omega \{\boldsymbol{\nabla}\boldsymbol{u} : \boldsymbol{\nabla}\boldsymbol{v} - p\boldsymbol{\nabla}\cdot\boldsymbol{v}\}\, \mathrm{d}\Omega &= \int_\Omega \boldsymbol{f}\cdot\boldsymbol{v}\,\mathrm{d}\Omega \quad \forall \boldsymbol{v} \in [\mathcal{V}_0]^d, \\ \int_\Omega \boldsymbol{\nabla}\cdot\boldsymbol{u} q\,\mathrm{d}\Omega &= 0 \qquad\qquad\quad \forall q \in \mathcal{Q} \end{aligned} \tag{3.14}$$

From this formulation it can be seen that the pressure variable may be interpreted as a Lagrange multiplier which maintains the incompressibility constraint. Substituting finite dimensional approximations to the above spaces we arrive at the linear system

$$\begin{pmatrix} A & B \\ B^T & 0 \end{pmatrix} \begin{pmatrix} \boldsymbol{u} \\ p \end{pmatrix} = \begin{pmatrix} \boldsymbol{f} \\ 0 \end{pmatrix}. \tag{3.15}$$

This is a prototypical example of a saddle-point problem. Solving this system is not straight forward as the presence of the zero diagonal block in the matrix adds additional requirements on the choice of pair spaces of $\boldsymbol{u}$ and p to ensure solvability.

Let $n_v = \dim(\mathcal{V}^h)$ be the number of free velocity degrees of freedom and $n_p = \dim(\mathcal{Q}^h)$ be the number of free pressure degrees of freedom. It then follows that B^T has dimensions $n_p \times n_v$. To ensure solvability we require that this matrix has a non-empty kernel, i.e $\ker(B^T) \neq \emptyset$. This leads to the necessary condition on combination of spaces: $\dim(Q^h) < \dim(\mathcal{V}^h)$. Formally, a sufficient stability condition for the choice of spaces is expressed as the Inf-Sup or Ladyzhenskaya, Babuska and Brezzi (LBB) condition:

$$\inf_{q\in Q^h} \sup_{\boldsymbol{w}^h \in V^h} \frac{(q^h, \boldsymbol{\nabla}\cdot\boldsymbol{w}^h)}{\|q^h\|_0 \|\boldsymbol{w}^h\|_1} \geq \alpha > 0. \tag{3.16}$$

Ensuring or showing that a pair of spaces satisfy this condition is not easy, although various well known stable space pairs exist in the literature. Alternatively, various approaches exist to attempt to circumvent the LBB condition such as relaxing the incompressibility constraint to be near-incompressible. Studies of the Stokes system are important to this work as many of these properties transfer to the Navier-Stokes system, as well as extensions such as the Oldroyd-B system.

The generalized Oldroyd-B system is solved with a mixed finite element method, which introduces two compatibility requirements. The first is the same as for the Stokes system, related to the incompressibility constraint. To handle this, we follow the work by Boyaval *et.al.* [15] where the known stable pair Crouzeix-Raviart triangular elements (quadratic velocity and discontinuous linear pressure) were used. We do so by selecting the quadrilateral analogous elements, namely: biquadratic velocity and discontinuous linear pressure. This is known as a stable choice (see Donea and Heurta [29] pg 285 and Fortin [36]) and exhibits similar convergence properties to the triangular elements.

The second requirement, as outlined in [6], arises when there is no solvent viscosity, i.e. the limit of the Upper Convected Maxwell model. This requires that the gradient of the velocity field must lie in the space of the extra-stress tensor. This typically requires equal order interpolations for the velocity and stress spaces, and a discontinuous space for the stress components. As we do not consider this limit, we are able to choose a much lower order polynomial for the extra stress. In particular we choose piecewise constant Q_0^{disc} elements and discontinuous bilinear elements Q_1^{disc}. This choice follows the theoretical arguments in [15], and in particular Q_0^{disc} elements for stress have been shown to produce a very stable algorithm for viscoelastic flow (see [4]).

3.4. The Generalized Oldroyd-B Model

In this section we develop the weak formulation for the generalized Oldroyd-B system along with details of the particular choices for the element spaces.

We seek to develop an algorithm to handle fully transient flows. Additionally many steady problems for viscoelastic flows are typically tackled by time-stepping towards equilibrium while maintaining constant boundary conditions. Time dependence is typically dealt with by first discretizing in time using a finite difference scheme and then using finite elements to solve the system spatially within each time step. We have chosen to use a fully implicit time differentiation to avoid additional CFL like restrictions. We also treat the problem monolithically, solving for all fields simultaneously. This results in a mixed method with the compatible choice of interpolation for each variable chosen, as discussed in section §3.3.1 above. With regards to the extra-stress tensor we have chosen two low-order element choices, namely: piecewise constant discontinuous Q_0^{disc} and bilinear discontinuous elements Q_1^{disc}. The two choices will allow for comparison with the Q_0^{disc} element known to be a very stable but inaccurate element, while the Q_1^{disc} element is less stable but more accurate. By solving the same problem with both elements we will be able to explore the extent to which this is so. In figure 3.3 the choice of element for each field is shown along with diagrammatic representations.

3.4.1. Natural Boundary Conditions

Before we construct the variational formulation for our problem, some attention should be paid to the definition of boundary conditions. For the system to be well-posed, either essential or traction boundaries should be prescribed for the velocity over the entire boundary and additionally inflow boundary conditions are required for the extra-stress field. The class of geometries that will be used most frequently in this work are flows through channels or pipes. Typically, fully-developed flow conditions (Poiseuille flow) are

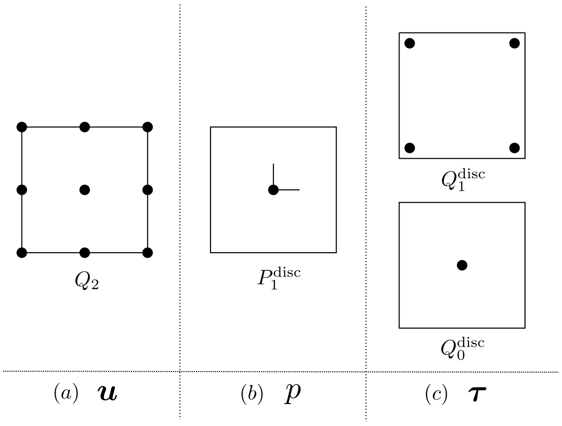

Figure 3.3. – Choice of elements for each field for the GOB problem. (a) Q_2 biquadratic continuous elements for the velocity field. (b) P_1^{disc} linear discontinuous elements for the pressure field. (c) A choice of Q_0^{disc} piecewise constant discontinuous and Q_1^{disc} bilinear discontinuous elements for the extra stress.

set at the inflow boundaries. This requires consistent velocity and stress values which are obtained by solving a 1D system. Details in this regard for the GOB model are presented in appendix A.

At outflow boundaries, many authors set fully-developed conditions for the velocity. This however requires that sufficiently long outflow channels are used to not severely affect the flow in the middle of the domain, near some region of interest. A different approach, as presented in [42], is the so called “do nothing” approach. Here the velocity and stress are treated as variables along the outflow boundary and a datum pressure is set at a point to ensure uniqueness. This is the approach that will be used in this work for all outflow boundaries.

3.4.2. Weak Formulation

To obtain the variational formulation of the generalized Oldroyd-B system, we first discretize the time derivatives with an implicit Euler scheme. To ease the notation, the velocity field is assumed to have homogeneous boundary values over the entire boundary, i.e. $\partial\Omega = \Gamma_{\text{D}}$ and $\boldsymbol{u}|_{\Gamma_D} = \mathbf{0}$; and the extra stress is assumed to have zero inflow boundary conditions along Γ_{IN}. We denote by d the spatial dimension of the domain, i.e. $d = 2$ or 3. We first introduce the spaces in which the solution is sought, these are: $\mathcal{V} = \{\boldsymbol{u} \in [H^1(\Omega)]^d \mid \boldsymbol{u}|_{\Gamma_D} = \mathbf{0}\}$ for the velocity field, $\mathcal{Q} = \{p \in L_2(\Omega)\}$ for the pressure field and $\mathcal{S} = \{\boldsymbol{\tau} \in [L_2(\Omega)]^{\frac{1}{2}d(d+1)} \mid \boldsymbol{\tau}|_{\Gamma_{\text{IN}}} = \mathbf{0}\}$ for the extra-stress field. An inner product of the momentum equation and an arbitrary test function $\boldsymbol{v} \in \mathcal{V}$ is then taken. The result is then integrated over the domain Ω and integration by parts is performed on the last three terms, resulting in

$$\int\limits_{\Omega} \left\{ \frac{\mathrm{Re}}{\Delta t}\, \boldsymbol{u}^n \cdot \boldsymbol{v} + \mathrm{Re}\, (\boldsymbol{u}^n \boldsymbol{\cdot} \boldsymbol{\nabla} \boldsymbol{u}^n) \cdot \boldsymbol{v} - p^n (\boldsymbol{\nabla} \boldsymbol{\cdot} \boldsymbol{v}) + \beta\, \boldsymbol{\nabla} \boldsymbol{u}^n : \boldsymbol{\nabla} \boldsymbol{v} + \boldsymbol{\tau}^n : \boldsymbol{\nabla} \boldsymbol{v} \right\} \mathrm{d}\Omega$$

$$= \int\limits_{\Omega} \frac{\mathrm{Re}}{\Delta t}\, \boldsymbol{u}^{n-1} \cdot \boldsymbol{v}\, \mathrm{d}\Omega + \int\limits_{\Gamma_N} \boldsymbol{n} \cdot (p^n\, \boldsymbol{I} - \boldsymbol{\nabla} \boldsymbol{u}^n - \boldsymbol{\tau}^n) \cdot \boldsymbol{v}\, \mathrm{d}\Gamma_{\mathrm{N}} \tag{3.17}$$

where an additional term on the Neumann boundaries arises following the treatment presented above. We similarly multiply the incompressibility condition by a test function $q \in \mathcal{Q}$ and integrate over the domain to yield the weak continuity equation

$$\int\limits_{\Omega} (\boldsymbol{\nabla} \boldsymbol{\cdot} \boldsymbol{u}^n) q\, \mathrm{d}\Omega = 0. \tag{3.18}$$

Lastly, the constitutive equation is contracted with $\boldsymbol{\sigma} \in \mathcal{S}$ and integrated over the domain, where due to the symmetry of the test function $\boldsymbol{\sigma}$ we simplify the final term to yield

$$\int\limits_{\Omega} \left\{ (1 + \frac{\mathrm{We}}{\Delta t}) \boldsymbol{\tau}^n \boldsymbol{:} \boldsymbol{\sigma} + \mathrm{We} \left\{ (\boldsymbol{u}^n \boldsymbol{\cdot} \boldsymbol{\nabla} \boldsymbol{\tau}^n) : \boldsymbol{\sigma} - (\boldsymbol{\nabla} \boldsymbol{u}^n) \boldsymbol{\tau}^n : \boldsymbol{\sigma} - \boldsymbol{\tau}^n (\boldsymbol{\nabla} \boldsymbol{u}^n)^T : \boldsymbol{\sigma} \right\} \right\} \mathrm{d}\Omega$$

$$+ \int\limits_{\Omega} 2\eta_p(\dot{\gamma}^n)\, (\boldsymbol{\nabla} \boldsymbol{u}^n) : \boldsymbol{\sigma}\, \mathrm{d}\Omega = \frac{\mathrm{We}}{\Delta t} \int\limits_{\Omega} \boldsymbol{\tau}^{n-1} : \boldsymbol{\sigma}\, \mathrm{d}\Omega. \tag{3.19}$$

We proceed by introducing finite dimensional approximations to the trial and test spaces, assuming the choice of finite element spaces are as discussed above. These are defined as

$$\begin{aligned} \mathcal{V}^h &= \mathcal{V} \cap \{ \boldsymbol{u}^h \in [C(\bar{\Omega})]^d \mid \boldsymbol{u}|_{\Omega_e} \in [Q_2(\Omega_e)]^d \}, \\ \mathcal{Q}^h &= \mathcal{Q} \cap \{ p|_{\Omega_e} \in P_1^{\mathrm{disc}}(\Omega_e) \}, \\ \mathcal{S}^h &= \mathcal{S} \cap \{ \boldsymbol{\tau}|_{\Omega_e} \in [Q_1^{\mathrm{disc}}(\Omega_e)]^{\frac{1}{2}d(d+1)} \text{ or } \boldsymbol{\tau}|_{\Omega_e} \in [Q_0^{\mathrm{disc}}(\Omega_e)]^{\frac{1}{2}d(d+1)} \}. \end{aligned}$$

The superscript h will be dropped from all the field variables so as not to cause confusion with the index n which indicates the time step. It follows that the variational formulation for the solution at time step n for the fully discrete problem is then given by:

- Given $(\boldsymbol{u}^{n-1}, \boldsymbol{\tau}^{n-1})$ find $\boldsymbol{u}^n \in \mathcal{V}^h$, $p^n \in \mathcal{Q}^h$ and $\boldsymbol{\tau}^n \in \mathcal{S}^h$ such that (3.17), (3.18) and (3.19) hold for all $\boldsymbol{v} \in \mathcal{V}^h$, $q \in \mathcal{Q}^h$ and $\boldsymbol{\sigma} \in \mathcal{S}^h$ respectively.

The Galerkin formulation above will result in the nonlinear system of equations

$$\begin{pmatrix} A(\boldsymbol{u}) & B & C \\ B^T & 0 & 0 \\ D(\boldsymbol{u}, \boldsymbol{\tau}) & 0 & E(\boldsymbol{u}, \boldsymbol{\tau}) \end{pmatrix} \begin{pmatrix} \boldsymbol{u} \\ p \\ \boldsymbol{\tau} \end{pmatrix} = \begin{pmatrix} R_1 \\ 0 \\ R_2 \end{pmatrix}. \tag{3.20}$$

Clearly this system cannot be solved as is and additional techniques are required to deal with the nonlinearity, stabilize the system and improve the efficiency of the solver. All the techniques which will be used for this purpose are discussed in the next chapter, where modifications made to the original strong formulation, the weak formulation and the resulting linear system will be presented.

3.5. Implementation

To aid in the implementation of the finite element method the Differential Equation Analysis Library (deal.II) [7] was used. This library is object-orientated (written in C++) and is freely available under an open-source license. The library consists of a useful set of tools required for finite element calculations. These include: bookkeeping, simple mesh generation, shape function definitions, various quadrature rules and linear algebra solvers, amongst many others. Additionally, the library may be linked with other open-source libraries and tools such as the GNU Scientific Library (GSL) [38] when additional functionality is needed.

Object orientated programming is a very natural setting for finite elements. This can be seen, for example, in the definition of the elements or cells relative to a parent cell (shown in section §3.1.4). This inherited structure is the essence of object-orientated design, consisting of a class and object definition where each real cell is an object of a general parent cell class. Additionally, other concepts in C++ such as inheritance of classes, allows for very modular design and the ability to reuse large sections of code. This occurs, for example, when using different choices of shape-functions which all derive from the same base element class. It is then possible to change only the definition without affecting the remainder of the code. This makes comparison of different shape functions and p-adaptivity easy to implement. The deal.II library is also focused on h-adaptivity, providing essential and easy to use tools for mesh refinement. Perhaps the most advantageous aspect of the deal.II library, and many other such open-source utilities, is the ability of the user to modify the code at any level and to be able to fully utilize many modern aspects of the C++ language.

Parallelism in finite element calculations is essential for larger problems and is thus incorporated into the library in two ways. Firstly distributed memory parallel computing is incorporated through the use of open MPI and modern linear algebra libraries such as PETSc or Trilinos[3]. Secondly, parallel computing with shared memory, i.e. a single machine with multiple cores, is incorporated using Intel's Threaded Building Blocks (TBB) [80] library. This library manages and optimizes thread usage and memory allocation. In this work only the latter form will be used as it is more simple to incorporate and since all computations were performed only on a single machine.

---

[3] See `www.mcs.anl.gov/petsc/` and `www.trilinos.sandia.gov` respectively

4. Numerical Methods

4.1. Overview

In the previous chapter the finite element method, which forms the backbone of our numerical method, was discussed and in particular its application towards solving the generalized Oldroyd-B problem. Focus was placed on the specific choice of finite element spaces used to interpolate each field. A naive implementation of these principles however yields a very expensive and unreliable scheme, due to various complications arising from the governing equations. Complications arise from the time-dependence, coupling of fields, nonlinearity and hyperbolicity in the constitutive equation. A successful algorithm requires that each of these issues be handled in turn.

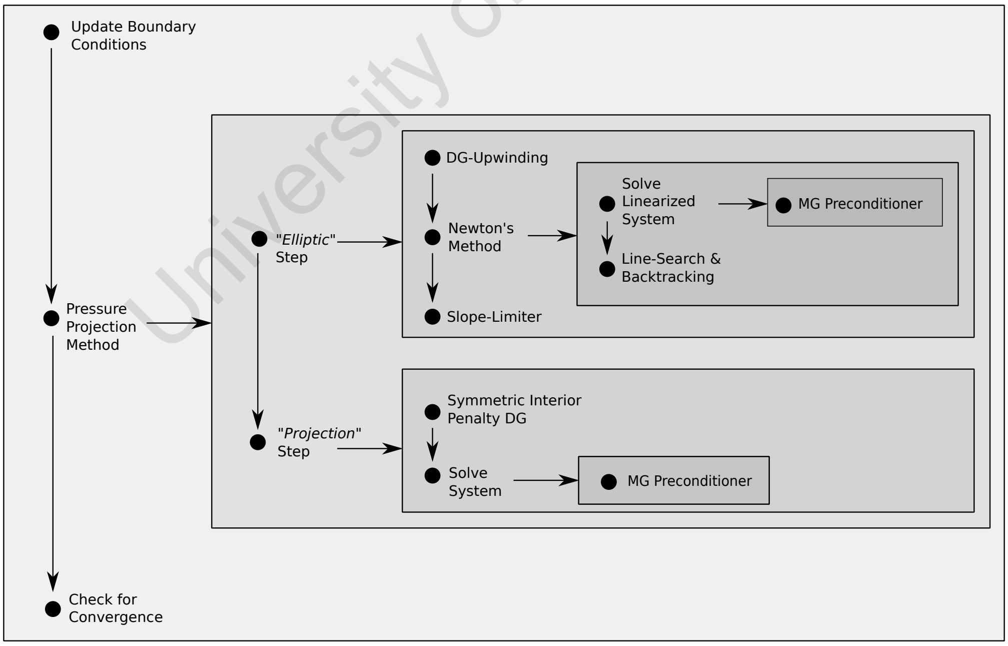

Figure 4.1. – Outline of the algorithm during each time step

We proceed by presenting a summary of the algorithm, which is represented graphically for each time step in figure 4.1, and then treat each aspect in more detail in the sections that follow. The time-dependence of the problem is dealt with by using a backward Euler finite difference scheme to discretize in time. This implicit algorithm, although more expensive, is more stable and circumvents restrictions on the allowed time step. In this manner we are able to solve both time-dependent problems, by updating boundary conditions at each time step, and steady problems by maintaining these conditions constant and time-stepping until the solution has converged.

Within each time step, the resulting system is solved spatially using finite elements. As we consider incompressible flow, we apply a pressure-projection method (section §4.2) to decouple the incompressibility constraint and the pressure variable from the governing system of equations. The pressure-projection method acts as a predictor-corrector scheme and consists of two steps. In the first "elliptic" step we solve the coupled momentum and constitutive equations, which we linearize using a Newton-Raphson scheme (section §4.4), modified to improve convergence properties through the use of a line-search algorithm (section §4.4.4). The hyperbolic terms in the constitutive equation are stabilized through a DG-upwinding scheme (section §4.3). We also introduce a slope limiter (section §4.5) to ensure monotone solutions when using Q_1^{disc} elements for the extra stress. The second "projection" step of the pressure-projection method consists of updating the pressure and enforcing incompressibility by solving a Poisson problem. Due to the discontinuous element choice for the pressure, we use a symmetric interior penalty DG (SIPDG) method (section §4.6.1) to solve this elliptic problem.

Numerical solutions for viscoelastic flows are notoriously expensive for non-trivial flows, and in an attempt to improve the efficiency of our algorithm we have incorporated a multigrid preconditioner to accelerate the linear algebra solvers for both the elliptic and projection step. We reserve the details of multigrid methods and their application to chapter 5.

4.2. Pressure-Projection Method

A common problem associated with solving incompressible flow numerically is the presence of a zero block on the diagonal of the system matrix, as in section §3.3.1. The fractional-step pressure projection method was introduced by Chorin [23] and Temam [85] to specifically solve such problems efficiently and robustly. The method is based on decoupling the pressure and incompressibility constraint from the momentum equations by considering a Helmholtz decomposition of the velocity field into an irrotational and solenoidal part, as

$$\boldsymbol{u} = \boldsymbol{u}_{\text{div}} + \boldsymbol{\nabla}\phi \;\text{ where }\; \boldsymbol{\nabla}\cdot\boldsymbol{u}_{\text{div}} = 0. \tag{4.1}$$

These methods can be expanded to incorporate viscoelasticity as discussed in [70] and implemented in [69]. In light of these references, a similar technique has been used in this work with the exception that the momentum and constitutive equations are not decoupled prior to applying the pressure-projection method.

The method can be viewed as a predictor-corrector scheme, where during the first "elliptic" step the coupled nonlinear momentum and constitutive equations are solved, while the pressure is treated explicitly using the value at the previous time step. Since only "slow" flows will be considered in this work, the convective terms in both equations are linearized using the convective field at the previous time step $\boldsymbol{u}^n$. This may be expressed as

$$\frac{\mathrm{Re}}{\Delta \mathrm{t}}\left(\boldsymbol{u}^{n*}-\boldsymbol{u}^{n}\right)+\mathrm{Re}\;\boldsymbol{u}^{n}\cdot\boldsymbol{\nabla}\boldsymbol{u}^{n*}+\nabla p^{n}-\beta\;\boldsymbol{\nabla}^{2}\boldsymbol{u}^{n*}-\boldsymbol{\nabla}\cdot\boldsymbol{\tau}^{n+1}=0 \tag{4.2}$$

for the momentum equation and

$$\begin{aligned}\boldsymbol{\tau}^{n+1}+\frac{\mathrm{We}}{\Delta t}(\boldsymbol{\tau}^{n+1}-\boldsymbol{\tau}^{n})+\mathrm{We}\;\boldsymbol{u}^{n}\cdot\boldsymbol{\nabla}\boldsymbol{\tau}^{n+1}-\mathrm{We}\left(\boldsymbol{\nabla}\boldsymbol{u}^{n+1}\right)\boldsymbol{\tau}^{n+1}&\\ -\mathrm{We}\;\boldsymbol{\tau}\left(\boldsymbol{\nabla}\boldsymbol{u}^{n+1}\right)^{T}-\eta_{p}(\dot{\gamma}^{n+1})\left\{\boldsymbol{\nabla}\boldsymbol{u}^{n+1}+\left(\boldsymbol{\nabla}\boldsymbol{u}^{n+1}\right)^{T}\right\}&=0\end{aligned} \tag{4.3}$$

for the constitutive equation. Note that we have ignored the incompressibility constraint and obtained expressions for an auxiliary velocity field $\boldsymbol{u}^{n*}$ and the stress at the new time $\boldsymbol{\tau}^{n+1}$.

In the second "projection" step, we ensure a divergence free velocity and update the pressure by solving the system

$$\begin{aligned}\frac{\mathrm{Re}}{\Delta \mathrm{t}}\left(\boldsymbol{u}^{n+1}-\boldsymbol{u}^{n*}\right)+\boldsymbol{\nabla}\phi^{n+1}&=0,\\ \boldsymbol{\nabla}\cdot\boldsymbol{u}^{n+1}&=0\end{aligned} \tag{4.4}$$

where $\phi^{n+1}=p^{n+1}-p^{n}$ is defined as the difference in pressure between time steps. The projection step can be simplified further by taking the divergence of the first equation in (4.4) and enforcing strongly the incompressibility constraint. This yields a Poisson problem for the difference in pressure

$$\boldsymbol{\nabla}^{2}\phi^{n+1}=-\frac{\mathrm{Re}}{\Delta \mathrm{t}}\boldsymbol{\nabla}\cdot\boldsymbol{u}^{n*}. \tag{4.5}$$

The numerical solution of (4.5) is relatively cheap, especially when combined with a multigrid method (chapter 5) which are most efficient for elliptic problems. The elimination of the final-step velocity is considered appropriate as $\boldsymbol{u}^{n*}$ and $\boldsymbol{u}^{n+1}$ converge to each other, and additionally makes the choice of boundary conditions more natural [40].

4.2.1. Boundary Conditions

As discussed in the review of Guermond [40], the definition of the boundary conditions for the elliptic and projection steps require special attention. For the elliptic step, we supply problem-dependent boundary conditions consisting of the Dirichlet boundary Γ_D, the traction boundary Γ_N and the inflow conditions for the stress tensor along Γ_{IN}, summarized as

$$\begin{aligned} \boldsymbol{u}^{n*}|_{\Gamma_D} &= \boldsymbol{b}_D, \\ \Big(p^n - \beta(\boldsymbol{\nabla}\boldsymbol{u}^{n*} + (\boldsymbol{\nabla}\boldsymbol{u}^{n*})^T) - \boldsymbol{\tau}^{n+1}\Big) \cdot \boldsymbol{n}|_{\Gamma_N} &= \boldsymbol{g}_N, \\ \boldsymbol{\tau}^{n+1}|_{\Gamma_{\text{IN}}} &= \boldsymbol{\tau}_{\text{IN}}. \end{aligned} \tag{4.6}$$

The boundary conditions for the projection step however require some manipulation, namely: only the normal component of the Dirichlet boundary can be enforced, hence resulting in a zero Neumann boundary for ϕ^{n+1} on that region

$$\begin{aligned} \boldsymbol{u}^{n+1} \cdot \boldsymbol{n}|_{\Gamma_D} &= \boldsymbol{b}_D \cdot \boldsymbol{n} \\ \Rightarrow \partial_n \phi^{n+1}|_{\Gamma_D} &= 0. \end{aligned} \tag{4.7}$$

Traction boundaries then correspond to zero Dirichlet boundaries for ϕ^{n+1}, shown as

$$\phi^{n+1}|_{\Gamma_N} = 0. \tag{4.8}$$

4.3. DG-Upwinding

4.3.1. Stabilization of Hyperbolic Problems

Obtaining numerical solutions for hyperbolic problems is not trivial, with classical methods such as Galerkin finite elements producing results which suffer from non-physical oscillations. The source of this problem arises from the fact that the truncation error introduced by the Galerkin method introduces negative diffusion into the system. In convection-diffusion equations this under-diffusion will depend on the Péclet number $P_e = ah/2\eta$, where a is the convective field, h is the discretization size and η is the viscosity. When P_e becomes large, i.e. coarse meshes or small viscosity, the nett diffusion may become negative leading to oscillations in solution fields. In equations with no diffusion terms, such as the constitutive equation for the GOB model, this problem is further amplified. These problems are not unique to finite elements, with similar issues occurring in finite difference and volume methods. A general discussion on this topic may be found in [29].

One solution to this problem in a finite element context is the introduction of numerical artificial diffusion in the form of upwinding along the streamlines of the flow. This method, as introduced by Brooks and Hughes [17], is referred to as Streamline-Upwind Petrov-Galerkin (SUPG). Generally speaking, Petrov-Galerkin methods are an extension of the Galerkin formulation, where the weight functions for all the terms in the weak form are chosen from a different class of functions than the test functions. SUPG methods involve choosing weight functions that promote diffusion along the characteristics, expressed as

$$\int_{\Omega} (\boldsymbol{\tau} + \overset{\nabla}{\boldsymbol{\tau}} - \eta_p(\dot{\gamma})(\boldsymbol{\nabla u} + \boldsymbol{\nabla u}^T)) : (\boldsymbol{\sigma} + \kappa \, \frac{\boldsymbol{u}}{\|\boldsymbol{u}\|} \cdot \boldsymbol{\nabla \sigma}) \, \mathrm{d}\Omega \tag{4.9}$$

where κ is a constant of the same order of magnitude as $\|\boldsymbol{u}\|$ and depends on the geometry of each element.

This stabilization technique has been extensively used in simulation of viscoelastic flows, as in [94] and [56] amongst others. A variant on this method is the inconsistent streamline-upwinding (SU) method. In this method, the modified weight functions are applied only to the convective term. An application of this technique to viscoelastic flows may be found in the paper of Marchal and Crochet [62]. Both the SU and SUPG methods introduce numerical blurring which reduces the accuracy of the resulting scheme. An optimal choice of stabilization parameter should thus be made.

Alternatively, there exist other techniques to stabilize hyperbolic problems, and in particular viscoelastic flows. One such approach is the characteristic method, as used in [89]. Here the motion of a collection of particles is tracked through the flow. The history of these particles may then be used to construct a set of characteristics that in turn are used to approximate the material derivative. The Galerkin/Least-Sqaures method, as used in [31], involves solving the least-squares formulation of the problem, which naturally introduces some diffusion.

In this work, following [15], a DG-upwinding stabilization will be used. This method was first applied to solving viscoelastic problems by Fortin [37] and has since received much attention in the computational rheology community. These methods, along with the streamline-upwinding schemes, are by far the most popular choices for stabilizing viscoelastic simulations. In the review [94], a comparative study between both methods is presented.

4.3.2. Derivation

In this section we derive the DG-upwinding method for the GOB equations. Consider a cell K_i as illustrated in figure 4.2, where a given convective field $\boldsymbol{u}$ is illustrated by the dotted arrows. The boundary of the cell can be divided into inflow $\Gamma^-_{K_i}$ (shown in bold) and outflow $\Gamma^+_{K_i}$ segments. Consider next the convective term in the constitutive equation

$$\boldsymbol{u} \cdot \vec{\boldsymbol{\nabla}} \boldsymbol{\tau}. \tag{4.10}$$

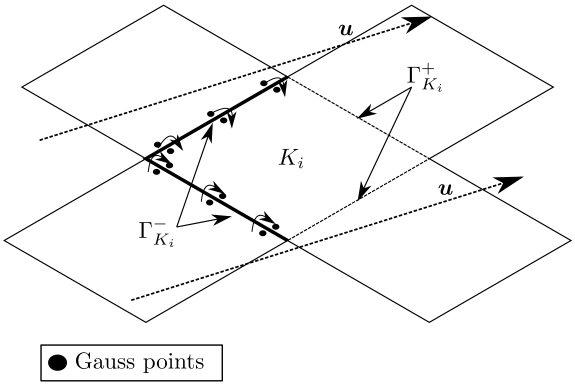

Figure 4.2. – DG-Upwinding for an internal cell K_i with overlaying convective field $\boldsymbol{u}$. The boundary of the cell Γ_{K_i} is decomposed into an inflow segment $\Gamma^{-}_{K_i}$ and outflow segment $\Gamma^{+}_{K_i}$. Jump terms are introduced along $\Gamma^{-}_{K_i}$ as shown at the Gauss points.

Since the stress elements are discontinuous across element boundaries, we may construct the weak formulation for a single cell at a time. We do so by contracting (4.10) with the weighting function $\boldsymbol{\sigma}$ and integrating over the cell K_i. By performing integration by parts we arrive at

$$\int_{K_i} (\boldsymbol{u}\cdot\vec{\boldsymbol{\nabla}}\boldsymbol{\tau}) : \boldsymbol{\sigma}\ \mathrm{d}K \quad = \quad -\int_{K_i} (\boldsymbol{\nabla}\cdot\boldsymbol{u})\,\boldsymbol{\tau} : \boldsymbol{\sigma}\ \mathrm{d}K_i + \int_{\Gamma_{K_i}} (\boldsymbol{u}\cdot\boldsymbol{n})\ \boldsymbol{\tau}^{\text{int}} : \boldsymbol{\sigma}^{\text{int}}\ \mathrm{d}\Gamma_{K_i} \tag{4.11}$$

where an additional boundary integral is introduced on the edges of the cell Γ_{K_i}. The superscript "int" implies that the values of these fields are considered from within the cell K_i. Integration by parts is performed again on the first term in (4.11) to produce

$$\int_{K_i} (\boldsymbol{u}\cdot\vec{\boldsymbol{\nabla}}\boldsymbol{\tau}) : \boldsymbol{\sigma}\ \mathrm{d}K = \int_{K_i} (\boldsymbol{u}\cdot\vec{\boldsymbol{\nabla}}\boldsymbol{\tau}) : \boldsymbol{\sigma}\ \mathrm{d}K_i + \int_{\Gamma_{K_i}} (\boldsymbol{u}\cdot\boldsymbol{n})\ \left(\boldsymbol{\tau}^{\text{int}} - \boldsymbol{\tau}^{\text{inflow}}\right) : \boldsymbol{\sigma}^{int}\ \mathrm{d}\Gamma_{K_i}. \tag{4.12}$$

In this instance, for the boundary integral, the value of stress is chosen such as to promote the flow of information with the convective field, i.e. upstream. This corresponds to choosing $\boldsymbol{\tau}^{\text{inflow}} = \boldsymbol{\tau}^{\text{int}}$ along the outflow boundary $\Gamma^{+}_{K_i}$ and $\boldsymbol{\tau}^{\text{inflow}} = \boldsymbol{\tau}^{\text{ext}}$, the value in the upstream cell, along the inflow boundary $\Gamma^{-}_{K_i}$. This choice is illustrated in figure 4.2, where upstream values at gauss points contribute to cell K_i. The expression (4.12) can then be simplified by considering

$$\int_{\Gamma_{K_i}} (\boldsymbol{u}\cdot\boldsymbol{n}) \left(\boldsymbol{\tau}^{\text{int}} - \boldsymbol{\tau}^{\text{inflow}}\right) : \boldsymbol{\sigma}^{\text{int}}\ \mathrm{d}\Gamma_{K_i} = \int_{\Gamma^{-}_{K_i}} (\boldsymbol{u}\cdot\boldsymbol{n})\ \left(\boldsymbol{\tau}^{\text{int}} - \boldsymbol{\tau}^{ext}\right) : \boldsymbol{\sigma}^{\text{int}}\ \mathrm{d}\Gamma^{-}_{K_i} \tag{4.13}$$

since the left hand side is non-zero only along the inflow boundary. Thus the DG-upwinding method consists of adding the above expression to the weak form of the convective term, as

$$\int_{K_i} (\boldsymbol{u} \cdot \vec{\boldsymbol{\nabla}} \boldsymbol{\tau}) : \boldsymbol{\sigma} \, \mathrm{d}K \to \int_{K_i} (\boldsymbol{u} \cdot \vec{\boldsymbol{\nabla}} \boldsymbol{\tau}) : \boldsymbol{\sigma} \, \mathrm{d}K + \int_{\Gamma^-_{K_i}} (\boldsymbol{u} \cdot \boldsymbol{n}) \, \left(\boldsymbol{\tau}^{\mathrm{int}} - \boldsymbol{\tau}^{\mathrm{ext}} \right) : \boldsymbol{\sigma}^{\mathrm{int}} \, \mathrm{d}\Gamma^-_{K_i}. \quad (4.14)$$

The second term in (4.14) may be interpreted as representing the Dirac jump in the field over the cell boundary. Furthermore, when using Q_0^{disc} elements, these “jump” integrals are the only source of convection in the equation as the first term in (4.14) is identically zero for these piecewise constant elements.

4.4. Newton-Raphson Method

4.4.1. Dealing with Non-linearity

In both the classical Oldroyd-B and the generalized model, the constitutive equation is nonlinear and hence has to be linearized in order to be treated numerically. This is most commonly done by either a fixed point iterative method, such as a Picard method, or by using a Newton-Raphson scheme. Although the Picard method is easy to implement, since no analytical derivatives of the governing equations are required, it converges linearly at best. The Newton-Raphson method, on the other hand, exhibits faster convergence and experience in the literature shows (see [70]) that it converges for higher We numbers and is typically more stable. For these reasons we will linearize the system of equations using a Newton-Raphson method as discussed below. It should be noted that since we consider only “slow” flows, we linearize the convective terms in the momentum and constitutive equations using a one-step Picard method, i.e. using the velocity values at a previous time.

The Newton-Raphson method is not unconditionally convergent, with the success of the method depending on the initial starting guess as well as properties of the system, depending on higher order derivatives which are typically unknown beforehand. There exists a radius of convergence centered at the solution point from which all initial guesses will converge. As Newton's method will be applied within a time-stepping scheme, the solution at a previous time will provide the initial guess. Hence provided the time step chosen is small enough, the solution should converge. The radius of convergence may also be expanded to allow for larger time steps by incorporating various globalization techniques, such as a line-search algorithm as discussed in section §4.4.4. In the sections that follow we introduce the Newton-Raphson method initially in an abstract setting in section §4.4.2 and then in its application to the GOB model in section §4.4.3.

4.4.2. Newton's Method

The Newton-Raphson method is a popular iterative root-finding method for nonlinear systems of equations and is presented in most introductory texts on numerical methods (see for example [19]). The popularity of this method is due to the potential quadratic convergence, when the initial "guess" is chosen sufficiently close to the actual solution. The algorithm can be derived as follows: consider a system of equations $\boldsymbol{R}(\boldsymbol{x}) = 0$, where an initial guess to solution $\boldsymbol{x}^n$ is available. A truncated Taylor series around this point can then be formulated as

$$\boldsymbol{R}(\boldsymbol{x}) = \boldsymbol{R}(\boldsymbol{x}^n) + \left.\frac{\partial \boldsymbol{R}}{\partial \boldsymbol{x}}\right|_{\boldsymbol{x}^n} \delta\boldsymbol{x} + \mathcal{O}(\delta\boldsymbol{x}^2). \tag{4.15}$$

By dropping all higher order terms in (4.15) and setting $\boldsymbol{R}(\boldsymbol{x}) = 0$ an iterative scheme is formed, expressed as

$$\begin{aligned} \left.\frac{\partial \boldsymbol{R}}{\partial \boldsymbol{x}}\right|_{\boldsymbol{x}^n} \delta\boldsymbol{x}^n &= -\boldsymbol{R}(\boldsymbol{x}^n), \\ \boldsymbol{x}^{n+1} &= \boldsymbol{x}^n + \delta\boldsymbol{x}^n \end{aligned} \tag{4.16}$$

where the matrix $\left.\frac{\partial \boldsymbol{R}}{\partial \boldsymbol{x}}\right|_{\boldsymbol{x}^n}$ denotes the Jacobian matrix. The procedure in (4.16) is then repeated until $\|\delta\boldsymbol{x}^n\|$ falls below a user-defined tolerance and convergence is achieved.

4.4.3. Newton's Method for the "Elliptic" Step

As discussed in section §4.2, the first step of the Pressure-Projection method involves solving the coupled nonlinear momentum and constitutive equations. Following the notation in section §4.4.2, the residuals for these equations are defined in block form as

$$\boldsymbol{R}(\boldsymbol{x}_k^n) := \begin{bmatrix} \boldsymbol{R}_u(\boldsymbol{x}_k^n, \boldsymbol{x}^{n-1}) \\ \boldsymbol{R}_\tau(\boldsymbol{x}_k^n, \boldsymbol{x}^{n-1}) \end{bmatrix} \text{ where } \boldsymbol{x}_k^n = \begin{bmatrix} \boldsymbol{u}_k^n \\ \boldsymbol{\tau}_k^n \end{bmatrix} \tag{4.17}$$

where the first component, representing the momentum equations, is defined as

$$\boldsymbol{R}_u = \frac{\mathrm{Re}}{\Delta t}(\boldsymbol{u}_k^n - \boldsymbol{u}^{n-1}) + \mathrm{Re}\, \boldsymbol{u}^{n-1} \cdot \boldsymbol{\nabla} \boldsymbol{u}_k^n + \boldsymbol{\nabla} p^{n-1} - \beta\, \nabla^2 \boldsymbol{u}_k^n - \boldsymbol{\nabla} \cdot \boldsymbol{\tau}_k^n \tag{4.18}$$

and the second component, representing the constitutive equation, is defined as

$$\begin{aligned} \boldsymbol{R}_\tau = {} & \boldsymbol{\tau}_k^n + \frac{\mathrm{We}}{\Delta t}(\boldsymbol{\tau}_k^n - \boldsymbol{\tau}^{n-1}) + \mathrm{We}\, \boldsymbol{u}^{n-1} \cdot \boldsymbol{\nabla} \boldsymbol{\tau}_k^n - \mathrm{We}\, (\boldsymbol{\nabla} \boldsymbol{u}_k^n) \boldsymbol{\tau}_k^n \\ & - \mathrm{We}\, \boldsymbol{\tau}_k^n (\boldsymbol{\nabla} \boldsymbol{u}_k^n)^T - \eta_p(\dot{\gamma}_k^n)(\boldsymbol{\nabla} \boldsymbol{u}_k^n + (\boldsymbol{\nabla} \boldsymbol{u}_k^n)^T). \end{aligned} \tag{4.19}$$

Linearizing the Shear-Rate-Dependent Viscosity

Prior to formulating the Jacobian of this system, special attention should be paid to the linearization of the polymeric viscosity function $\eta_p(\dot{\gamma})$. Only the Carreau-Yasuda function will be considered, which we recall for convenience is defined as

$$\eta_p(\dot{\gamma}) = (\alpha - \beta) + (1 - \alpha)(1 + (\lambda\dot{\gamma})^a)^{\frac{n-1}{a}}. \tag{4.20}$$

To linearize this function we seek to express it in the form

$$\eta_p\left(\dot{\gamma}_k^{n+1}\right) \simeq \eta_p\left(\dot{\gamma}_k^n\right) + \delta\eta_p(\dot{\gamma}_k^n) \tag{4.21}$$

where $\delta\eta_p(\dot{\gamma}_k^n)$ is in terms of the velocity field. Since the viscosity function depends on $\dot{\gamma}$, which itself depends on $\boldsymbol{u}$, we initially linearize the shear-rate by using a binomial expansion of the square root to yield

$$\begin{aligned} \delta\dot{\gamma}_k^n &= \frac{1}{2}\left(\dot{\gamma}_k^n\right)^{-1} B_k^n, \\ \text{where } B_k^n &:= 2\boldsymbol{\nabla u}_k^n : \boldsymbol{\nabla \delta u}_k^n + \boldsymbol{\nabla u}_k^n : (\boldsymbol{\nabla \delta u}_k^n)^T + \boldsymbol{\nabla \delta u}_k^n : (\boldsymbol{\nabla u}_k^n)^T \end{aligned} \tag{4.22}$$

where the additional variable B_k^n is introduced to ease notation. We are now in a position to linearize the viscosity function (4.20) by once again using a binomial expansion, which results in

$$\delta\eta_p(\dot{\gamma}_k^n) = \frac{\lambda(1-\alpha)(n-1)}{2}(1 + (\lambda\dot{\gamma}_k^n)^a)^{\frac{(n-1)-a}{a}} B_{k+1}^{n+1}. \tag{4.23}$$

Lastly, to improve readability, the function $L_p(\dot{\gamma})$ can be defined as

$$L_p(\dot{\gamma}) = \frac{\lambda(1-\alpha)(n-1)}{2}(1 + (\lambda\dot{\gamma})^a)^{\frac{(n-1)-a}{a}}. \tag{4.24}$$

Linearizing the Generalized Oldroyd-B Model

With the expressions and definitions above it is now possible to determine the Jacobian matrix for the elliptic step, which has a block structure

$$\frac{\partial \boldsymbol{R}(\boldsymbol{x}^n)}{\partial \boldsymbol{x}^n}\delta\boldsymbol{x}^n = \begin{bmatrix} J_{uu}(\boldsymbol{u}_k^n) & J_{u\tau} \\ J_{\tau u}(\boldsymbol{u}_k^n, \boldsymbol{\tau}_k^n) & J_{\tau\tau}(\boldsymbol{u}_k^n) \end{bmatrix} \begin{bmatrix} \delta\boldsymbol{u}^n \\ \delta\boldsymbol{\tau}^n \end{bmatrix}. \tag{4.25}$$

Each component of this structure is then defined as

$$
\begin{aligned}
J_{uu}(\boldsymbol{u}_k^n)\delta\boldsymbol{u}_k^n &= \frac{Re}{\Delta t}\delta\boldsymbol{u}_k^n + \mathrm{Re}\ \boldsymbol{u}^{n-1}\cdot\vec{\boldsymbol{\nabla}}\delta\boldsymbol{u}_k^n - \beta\ \vec{\nabla}^2\delta\boldsymbol{u}_k^n,\\
J_{u\tau}\delta\boldsymbol{\tau}_k^n &= -\vec{\boldsymbol{\nabla}}\cdot\delta\boldsymbol{\tau}_k^n,\\
J_{\tau u}(\boldsymbol{u}_k^n,\boldsymbol{\tau}_k^n)\delta\boldsymbol{u}_k^n &= -\mathrm{We}\ \boldsymbol{\nabla}\delta\boldsymbol{u}_k^n\boldsymbol{\tau}_k^n - \mathrm{We}\ \boldsymbol{\tau}_k^n(\boldsymbol{\nabla}\delta\boldsymbol{u}_k^n)^T\\
&\quad - \eta_p(\dot{\gamma}_k^n)(\boldsymbol{\nabla}\delta\boldsymbol{u}_k^n + (\boldsymbol{\nabla}\delta\boldsymbol{u}_k^n)^T) - L(\dot{\gamma}_k^n)\ B_k^n\ (\boldsymbol{\nabla}\boldsymbol{u}_k^n + (\boldsymbol{\nabla}\boldsymbol{u}_k^n)^T),\\
J_{\tau\tau}(\boldsymbol{u}_k^n)\delta\boldsymbol{\tau}_k^n &= (1+\frac{\mathrm{We}}{\Delta\mathrm{t}})\delta\boldsymbol{\tau}_k^n + \mathrm{We}\ \boldsymbol{u}_k^n\cdot\vec{\boldsymbol{\nabla}}\delta\boldsymbol{\tau}_k^n - \mathrm{We}\ \boldsymbol{\nabla}\boldsymbol{u}_k^n\delta\boldsymbol{\tau}_k^n\\
&\quad - \mathrm{We}\ \delta\boldsymbol{\tau}_k^n(\boldsymbol{\nabla}\boldsymbol{u}_k^n)^T.
\end{aligned}
\tag{4.26}
$$

4.4.4. Globalization of Newton's Method

It is known that while Newton's method will converge quickly when the initial choice is sufficiently close to the real solution, it will often diverge when this is not the case. In this work, the Newton method is incorporated inside a time-stepping scheme which usually provides sufficiently accurate starting solutions by using the value at the previous time step as an initial guess. However, during times of rapid activity this requires that the time step becomes appropriately small, which may increase the computational cost dramatically. One solution to this problem is to introduce a globalization modification to Newton's method which increases the convergence radius of the method. The line-search and backtracking method will be used in this case. Details of this technique will be presented below following the work in [78].

Line Search and Backtracking

The line-search and backtracking method seeks to globalize Newton's method by exploiting the fact that each root of $\boldsymbol{R}(\boldsymbol{x})$ is also a minimum of $r(\boldsymbol{x})$, which is defined as

$$
r(\boldsymbol{x}) := \frac{1}{2}\boldsymbol{R}^T(\boldsymbol{x})\boldsymbol{R}(\boldsymbol{x}). \tag{4.27}
$$

Convergence of the scheme can then be ensured by requiring that after each step of the Newton-Raphson scheme, r is reduced, i.e.

$$
r(\boldsymbol{x}_{k+1}^n) < r(\boldsymbol{x}_k^n). \tag{4.28}
$$

It is advantageous to preserve the quadratic convergence properties of the Newton method and avoid excessive dampening. Thus initially a full Newton step (i.e.(4.16)) is attempted. If the new approximation satisfies (4.28), no dampening is necessary. However if this is not the case, the correction to the initial solution must be damped by a parameter λ, as in

$$
\boldsymbol{x}_{k+1}^n = \boldsymbol{x}_k^n + \lambda\delta\boldsymbol{x}_k^n \tag{4.29}
$$

until this condition is satisfied. It should be noted that the search direction $\delta\boldsymbol{x}_k^n$ determined by (4.25) is the minimization direction of r. This may be seen by noting that

$$\boldsymbol{\nabla} r \cdot \delta\boldsymbol{x}_k^n = -\boldsymbol{R}^T\boldsymbol{R} < 0. \tag{4.30}$$

The "distance" traveled along this direction may, however, overshoot the minimum. Nonetheless, the minimum will lie somewhere along this direction and thus the globalization technique reduces to finding the distance, or amount of dampening λ, which minimizes r. To do so, we define a quadratic polynomial approximation with respect to λ *viz.* the function $g(\lambda)$, expressed as

$$\begin{aligned} g(\lambda) &= r(\boldsymbol{x}_k^n + \lambda\delta\boldsymbol{x}_k^n) \approx [g(1) - g(0) - g'(0)]\lambda^2 + g'(0)\lambda + g(0) \\ \text{where } g'(0) &= -\boldsymbol{R}^T(\boldsymbol{x}_k^n)\boldsymbol{R}(\boldsymbol{x}_k^n). \end{aligned} \tag{4.31}$$

The minimum of this function occurs at $\lambda = \lambda_{\min}$, which may be expressed as

$$\lambda_{\min} = -\frac{g'(0)}{2[g(1) - g(0) - g'(0)]}. \tag{4.32}$$

If the new approximation $\boldsymbol{x}_{k+1}^n = \boldsymbol{x}_k^n + \lambda_{\min}\delta\boldsymbol{x}_k^n$ satisfies the condition (4.28), then the line-search algorithm may terminate. However, it may turn out that the quadratic approximation in (4.31) is insufficient, and so additional back-tracking may be necessary to minimize r.

This occurrence is dealt with by successively approximating $g(\lambda)$ with a cubic polynomial with respect to λ and fitting the coefficients from the best available data, i.e. $g(0)$, $g'(0)$ and the values of g at the last two choices of dampening parameter, $g(\lambda_1)$ and $g(\lambda_2)$. The minimum of the fitted cubic polynomial is then determined explicitly and the new corrected approximation to the root is made. This process is then repeated until the condition (4.28) is satisfied. It may occur that the dampening parameter that minimizes g is so small as to make Newton's method stagnant. To avoid this, an additional check that the dampening parameter is larger than a user-set minimum is incorporated. Were this to occur, the time step is reduced and Newton's method is restarted.

With regards to efficiency, it should be mentioned that an optimal choice of time step would avoid excessive dampening in each Newton iteration, since evaluation of the residual is a costly process. The line-search method should only be required to act as a fail-safe in improving the robustness of the method.

4.5. Slope Limiter

4.5.1. Introduction

A frequent occurrence when solving hyperbolic problems is the presence of shocks and sharp gradients in the solution. These regions are prone to non-physical oscillations when discretization is done using discontinuous elements of higher order than piecewise constant. The presence of these non-physical oscillations not only destroy the accuracy of the method, but may also lead to a loss of stability. Slope limiters or "flux limiters" are sometimes applied to curb this problem. An example of this may be found in [26], where a nonlinear convection-diffusion problem was studied.

With regard to the GOB model, the hyperbolic character of the constitutive equation leads to the emergence of sharp stress-gradients especially near walls and geometric singularities. The preservation of the monotonicity of the stress components of the solution has been shown to be related to the stability of the method [5]. This monotonicity is guaranteed by using piecewise constant elements, which may explain the observed robustness when applied to solving viscoelastic flow. It was shown in [5] that by applying a slope limiter these oscillations can be controlled and the stability of the method is extended to larger Weissenberg numbers.

Preliminary numerical experiments for this work showed that although piecewise interpolations for the stress components produced a stable and efficient method for solving the OB and GOB systems, the lack of accuracy incurred from this low-order would become prohibitive when seeking quantitative results. Alternatively, we may seek to improve the accuracy by using higher-order piecewise-bilinear elements Q_1^{disc}, as was done in [4]. In this work a slope limiter was introduced to control the non-physical oscillations. The slope limiter chosen for this work is based on the paper of Hoteit *et.al.* [43] for quadrilateral elements. The details of this limiter and its implementation are discussed in the sections below.

4.5.2. One Dimensional Slope Limiters

Consider the one-dimensional discretization shown in figure 4.3, where a segment of three consecutive cells K_{i-1}, K_i and K_{i+1} is shown along with labeled vertices. A linear-discontinuous interpolation will be considered with solutions ω_i^0 and ω_i^1 representing the value at the left and right vertex respectively for the i^{th} cell, while $\langle\omega_i\rangle$ represents the average solution over that cell. An example of loss of monotonicity can be seen as highlighted in gray in figure 4.3, where w_i^1 is smaller than the average in the neighboring cell $\langle w_{i+1}\rangle$. The purpose of the slope limiter is to smooth the solution such that the value at each vertex, from each cell lies between the averages of its neighbouring cells. Additionally, the average over each cell should be maintained and the solution changed as little as possible.

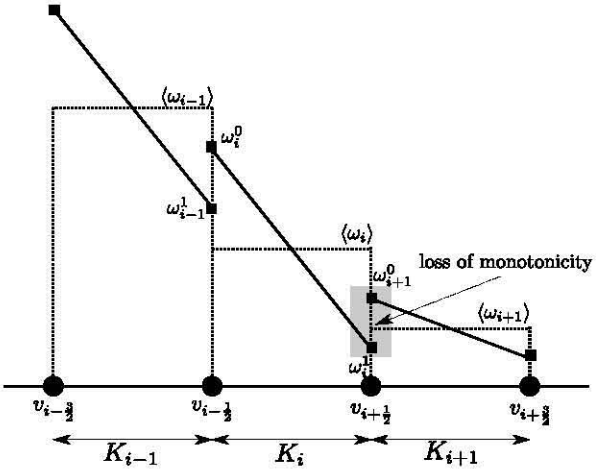

Figure 4.3. – An example of linear 1D elements exhibiting loss of monotonicity in the highlighted region, where the use of a slope limiter would be appropriate

In section §4.5.3 below, the definition and notations required for a slope limiter will be introduced for rectangular Q_1^{disc} elements.

4.5.3. Two Dimensional Slope Limiter for Q_1^{disc} elements

Definition

The slope limiter may be defined as follows: consider a solution $\boldsymbol{u}$, with u_i representing the solution value at each degree of freedom i. Assuming u_i lies in the cell A_i, we denote by $\langle A_i \rangle$ the solution average over that cell. Furthermore, assume that u_i is associated with the vertex v_i and $\mathcal{F}_i$ is the set of all cells that contain v_i. The slope limiter then seeks to produce the solution $\boldsymbol{w}$ which solves

$$\min_{\boldsymbol{w}} \frac{1}{2} \|\boldsymbol{u} - \boldsymbol{w}\|_2^2 \tag{4.33}$$

subject to the constraints

$$\begin{aligned} \langle w \rangle_{A_i} = \langle u \rangle_{A_i} \qquad & \forall i = 1..N_{\text{cells}}, \\ \eta_i \leq w_i \leq \xi_i \qquad & \forall i = 1..N_{\text{dofs}} \end{aligned} \tag{4.34}$$

where the bounds above are defined as

$$\eta_i = (1 - \alpha_{\text{SL}}) \langle \boldsymbol{w} \rangle_{A_i} + \alpha_{\text{SL}} \min_{A_k \in \mathcal{F}_i} \langle \boldsymbol{w} \rangle_{A_k}, \tag{4.35}$$

$$\xi_i = (1 - \alpha_{\text{SL}}) \langle \boldsymbol{w} \rangle_{A_i} + \alpha_{\text{SL}} \max_{A_k \in \mathcal{F}_i} \langle \boldsymbol{w} \rangle_{A_k}. \tag{4.36}$$

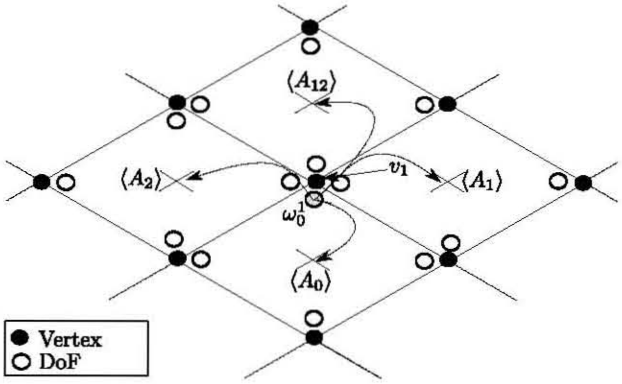

Figure 4.4. – Dependence of the bounds on degrees of freedom for a 2D quadrilateral element. A degree of freedom ω_0^1 lying within cell A_0 and associated with the vertex v_1 will be bounded by the averages in the cells which share v_1, i.e. $\langle A_0 \rangle$, $\langle A_1 \rangle$, $\langle A_{12} \rangle$ and $\langle A_2 \rangle$.

The parameter α_{SL} denotes the extent to which the solution is limited, where $\alpha_{\mathrm{SL}} = 0$ produces piecewise constant approximations.

To illustrate this consider figure 4.4, where a segment of the mesh is shown. Consider the degree of freedom ω_0^1 which resides in the cell A_0 and is associated with the vertex v_1. The bounds of this degree of freedom will then depend on the solution averages over the cells which share v_1, i.e. $\langle A_0 \rangle, \langle A_1 \rangle, \langle A_{12} \rangle$ and $\langle A_2 \rangle$, as shown in figure 4.4.

Implementation

1D slope limiters are defined by an explicit rule, however in higher dimensions this is not the case. To apply the slope limiter (4.33) and (4.34), a quadratic programming problem needs to be solved. Such problems arise frequently in different contexts and hence many different methods exist for tackling them. Since the limiter needs to be applied at each time step, an efficient and robust method is required. An active-set algorithm was chosen for this purpose, which is an extension of the Theil-Van de Panne procedure (see [13]).

The basis of this method is that equality constrained minimization problems can be easily solved using Lagrange multipliers, as described below. The optimal solution will have a subset of the inequality constraints acting as active, i.e. as equalities. It then remains to find this subset of active constraints while ensuring that the solution remains feasible, i.e. all the bounds are satisfied. The details of the algorithm follow [43] and are presented below.

Minimization Subject to Linear Equality Constraints

To minimize (4.33) under some set of linear constraints we express this function in the form

$$\min_{\boldsymbol{w}} \left\{ \frac{1}{2}\boldsymbol{w}^T\boldsymbol{w} - \boldsymbol{u}^T\boldsymbol{w} + \frac{1}{2}\boldsymbol{u}^T\boldsymbol{u} \right\} \quad \text{subject to } C\boldsymbol{w} = \boldsymbol{b} \tag{4.37}$$

by expanding the L2-norm, while the linear constraints are expressed in a matrix form. As before it will be assumed that $\boldsymbol{w}, \boldsymbol{u} \in \mathbb{R}^{N_{dofs}}$ and that there are N_{cnstr} constraints, hence $C \in \mathbb{R}^{N_{\text{cnstr}} \times N_{\text{dofs}}}$ and $\boldsymbol{b} \in \mathbb{R}^{N_{cnstr.}}$. To solve this problem the method of Lagrange multipliers will be used. The Lagrangian

$$\mathcal{L}(\boldsymbol{w}, \boldsymbol{\lambda}) = \frac{1}{2}\boldsymbol{w}^T\boldsymbol{w} - \boldsymbol{u}^T\boldsymbol{w} + \frac{1}{2}\boldsymbol{u}^T\boldsymbol{u} + \boldsymbol{\lambda}(C\boldsymbol{w} - \boldsymbol{b}) \tag{4.38}$$

is introduced, where $\boldsymbol{\lambda}$ is the vector of Lagrange multipliers for each constraint. To minimize this function the derivatives of (4.38) are taken with respect to $\boldsymbol{w}$ and $\boldsymbol{\lambda}$ and equated to zero to form the resulting system of equations

$$\begin{aligned} \boldsymbol{w} + C^T\boldsymbol{\lambda} &= \boldsymbol{u}, \\ C\boldsymbol{w} &= \boldsymbol{b}. \end{aligned} \tag{4.39}$$

The solution of this system produces the minimizing vector $\boldsymbol{w}$ and the Lagrange multipliers $\boldsymbol{\lambda}$ which correspond to “forcing” terms that maintain the constraints.

To solve the saddle point problem (4.39), a Schur complement technique is used. This consists of multiplying the first system in (4.39) by C from the left and then substituting the second system to obtain

$$CC^T\boldsymbol{\lambda} = C\boldsymbol{u} - \boldsymbol{b}. \tag{4.40}$$

Once (4.40) is solved for $\boldsymbol{\lambda}$, it is then possible to obtain $\boldsymbol{w}$ by substituting the previous solution into

$$\boldsymbol{w} = \boldsymbol{u} - C^T\boldsymbol{\lambda}. \tag{4.41}$$

Numerically, C is very sparse and hence CC^T is not formed explicitly. Instead the action of this compound matrix on a vector is used within an iterative solver. A conjugate gradient solver is used which exploits the symmetry of CC^T.

Active-Set Algorithm

We proceed by describing the active-set algorithm used to solve the quadratic programming problem: (4.33) and (4.34).

Let $\boldsymbol{u}$ be the initial unlimited solution and let $\boldsymbol{z}$ be the result of assigning the cell-average value to each degree of freedom. The vector $\boldsymbol{z}$ will naturally satisfy the bounds (4.34) but not necessarily minimize (4.33). Additionally we define the active-set as all the degrees of freedom which satisfy their bound in (4.34) (b) exactly, i.e. with equality. The algorithm then successively "improves" $\boldsymbol{z}$ by solving (4.37) where the matrix C consists of the constraints in (4.34) (a) and also a set of constraints that require all the degrees of freedom in the active-set to remain constant.

If the resulting solution is infeasible, i.e. a constraint in (4.34) (b) is violated, then additional constraints are added to the active-set. The degree of freedom which least violates its constraint is added to the set. On the other hand, if the solution is feasible, some of the active-constraints may not be optimal. For an active constraint to be satisfied optimally, it is required that for the lower-bounnd constraint, η_i, the Lagrange multiplier which "forces" this constraint is negative; and vice-versa for the upper-bound constraint, ξ_i, the Lagrange multiplier must be positive. All non-optimal constraints are dropped from the active-set and the process is repeated until the solution is feasible and all active constraints are optimal. It should be mentioned that although the algorithm appears iterative, it is guaranteed to terminate successfully within a finite number of steps[1].

Pseudo-code is presented in algorithm 4.1 to fully describe the procedure, based on [43]. The following definitions are required for the pseudo-code: the function $\boldsymbol{w} \leftarrow \text{CellAve}(\boldsymbol{u})$ assigns to each degree of freedom in $\boldsymbol{w}$ its cell average. The active-set is defined as S and contains the degrees of freedom which are constrained actively, while the function $S(i)$ provides the index of the Lagrange multiplier concerning the i^{th} degree of freedom. The function $S \leftarrow \text{ActiveConstr.}(\boldsymbol{w})$ is defined to fill the active-set with all actively constrained degrees of freedom, within some floating-point tolerance.

---

[1] Assuming no floating point truncation

Algorithm 4.1 Active-Set Slope Limiter

```
function SLOPE LIMITER($\boldsymbol{u}$)
    $\boldsymbol{w} \leftarrow$ CellAve($\boldsymbol{u}$)        ▷ set solution to cell averaged values
    $S \leftarrow$ ActiveConstr.($\boldsymbol{w}$)        ▷ update active set
    while $\boldsymbol{w}$ not optimal do
        solve the constrained minimization problem :
            $$\min_{\boldsymbol{z}} \|\boldsymbol{z}-\boldsymbol{u}\|_2^2 \quad \langle z_i \rangle = \langle u_i \rangle \quad \forall i = 1..N_{\text{dofs}} \quad z_i = w_i \quad \forall i \epsilon S$$
        if $\boldsymbol{z}$ is feasible then
            $\boldsymbol{z}$ is optimal $\Leftrightarrow \begin{cases} \text{if } z_i = \eta_i & \text{then } \lambda_{S(i)} \leq 0 \\ \text{if } z_i = \xi_i & \text{then } \lambda_{S(i)} \geq 0 \end{cases} \forall i \in S$
            if $\boldsymbol{z}$ is optimal then
                $\boldsymbol{w} \leftarrow \boldsymbol{z}$        ▷ solution found exit function
            else
                $\lambda_{S(j)} = \max_{i \in S} \begin{cases} |\lambda_i| & \lambda_i \text{ is not optimal} \\ 0 & \lambda_i \text{ is optimal} \end{cases}$
                $S \leftarrow S/\{j\}$
                $\boldsymbol{w} \leftarrow \boldsymbol{z}$        ▷ remove non-optimal constraint from active set
            end if
        else
            $T = \{i|\lambda_i \text{ is not feasible}\}$        ▷ set of constraints not satisfied
            $\delta_j = \min_{i \in T} \begin{cases} \frac{w_i-\eta_i}{w_i-z_i} & z_i < \eta_i \\ \frac{w_i-\xi_i}{w_i-z_i} & z_i > \xi_i \end{cases}$        ▷ constraint least offended
            $\boldsymbol{w} \leftarrow \boldsymbol{w} - \delta(\boldsymbol{w}-\boldsymbol{z})$        ▷ update solution
            $S \leftarrow$ ActiveConstr.($\boldsymbol{w}$)        ▷ update active set
        end if
    end while
    return $\boldsymbol{w}$        ▷ the limited solution
end function
```

4.6. Projection Step

Each time step in the pressure-projection method section §4.2 requires solving a Poisson problem of the form

$$\begin{aligned} \nabla^2 \phi &= -f \ \ \forall \boldsymbol{x} \in \Omega, \\ \phi|_{\Gamma_D} &= 0, \\ \partial_n \phi|_{\Gamma_N} &= 0 \end{aligned} \tag{4.42}$$

to update the pressure and enforce the incompressibility of the velocity. Due to the compatibility requirement for the velocity and pressure finite element spaces, as discussed in section §3.3.1, P_1^{disc} discontinuous elements are used to approximate the pressure and hence also ϕ. As discussed in [81], elliptic problems such as (4.42), require additional stabilization when discontinuous elements are used. A symmetric interior penalty DG method (SIPDG) will be used which stabilizes the problem through the introduction of flux terms or jump penalties across the element boundaries.

4.6.1. Symmetric Interior Penalty DG (SIPDG)

The problem is formulated in its weak form using the same discontinuous spaces for the weight functions φ. Since all degrees of freedom lie within a cell, we may integrate (4.42) multiplied by the weight function φ over an internal cell K_i with boundary Γ_{K_i} to yield

$$\int\limits_{K_i} \nabla^2 \phi \, \varphi \, \mathrm{d}K_i = -\int\limits_{K_i} f \varphi \, \mathrm{d}K_i. \tag{4.43}$$

Integration by parts is performed on the integral on the left-hand-side to result in

$$\int\limits_{K_i} \boldsymbol{\nabla}\phi \cdot \boldsymbol{\nabla}\varphi \, \mathrm{d}K_i - \int\limits_{\Gamma_{K_i}} (\boldsymbol{\nabla}\phi \, \varphi) \cdot \boldsymbol{n}_{K_i} \, \mathrm{d}\Gamma_{K_i} = \int\limits_{K_i} f\varphi \, \mathrm{d}K_i. \tag{4.44}$$

An additional boundary integral over Γ_{K_i} emerges taken in a positive orientation, i.e anticlockwise, such that $\boldsymbol{n}_{K_i}$ represents the outward normal. Let the mesh be defined as the set of cells $\mathcal{T}_h = \{K_i \mid i = 1..N_{\text{cells}}\}$ and additionally define the set of edges $\mathcal{E}_h = \{e_j \mid i = 1..N_{\text{edges}}\}$. Furthermore, consider the division of edges into the sets of internal edges $\mathcal{E}_h^{\text{I}}$, edges along Neumann boundaries $\mathcal{E}_h^{\text{N}}$ and edges along Dirichlet boundaries $\mathcal{E}_h^{\text{D}}$ such that $\mathcal{E}_h = \mathcal{E}_h^{\text{I}} \cup \mathcal{E}_h^{\text{D}} \cup \mathcal{E}_h^{\text{N}}$. If we then add the contributions of (4.44) from each cell, the boundary integrals on these cells can be grouped together with respect to edges and not cells. Additionally, an integral to enforce the Dirichlet conditions is introduced. This results in the system

$$\sum_{K\in\mathcal{T}_h}\int\limits_K \boldsymbol{\nabla}\phi\cdot\boldsymbol{\nabla}\varphi\,\mathrm{d}K-\sum_{e\in\mathcal{E}_h^{\mathrm{I}}}\int\limits_{\Gamma_e}\left\{\boldsymbol{\nabla}\phi^{+}\varphi^{+}\cdot\boldsymbol{n}^{+}+\boldsymbol{\nabla}\phi^{-}\varphi^{-}\cdot\boldsymbol{n}^{-}\right\}\,\mathrm{d}\Gamma_e$$

$$-\sum_{e\in\mathcal{E}_h^{\mathrm{N}}}\int\limits_{\Gamma_e}\boldsymbol{\nabla}\phi\;\varphi\cdot\boldsymbol{n}\,\mathrm{d}\Gamma_e+\sum_{e\in\mathcal{E}_h^{\mathrm{D}}}\int\limits_{\Gamma_e}(\phi-0)\varphi\,\mathrm{d}\Gamma_e=\sum_{K\in\mathcal{T}_h}\int\limits_K f\varphi\,\mathrm{d}K \tag{4.45}$$

where each internal edge is shared by two cells labeled by + and − with outward normals $\boldsymbol{n}^{+}$and $\boldsymbol{n}^{-}$ respectively. The discontinuous functions ϕ and φ have two values along each edge, corresponding to their value in either cell. These are denoted with the appropriate superscript. The choice of which cell is defined as positive or negative is irrelevant within this formulation.

Definitions for the averages and jumps over edges can then be introduced as

$$\{\!\{\boldsymbol{\nabla}\phi\}\!\}\equiv\frac{1}{2}\{\boldsymbol{\nabla}\phi^{+}+\boldsymbol{\nabla}\phi^{-}\}\quad\text{and}\quad\{\!\{\varphi\}\!\}\equiv\frac{1}{2}\{\varphi^{+}+\varphi^{-}\}$$

$$[\![\boldsymbol{\nabla}\phi]\!]\equiv\{\boldsymbol{\nabla}\phi^{+}\cdot\boldsymbol{n}^{+}+\boldsymbol{\nabla}\phi^{-}\cdot\boldsymbol{n}^{-}\}\quad\text{and}\quad[\![\varphi]\!]\equiv\{\varphi^{+}\boldsymbol{n}^{+}+\varphi^{-}\boldsymbol{n}^{-}\}. \tag{4.46}$$

It should be noted that whereas the averages of scalars and vectors are defined as scalars and vectors respectively, the jump of a vector quantity is defined as a scalar and similarly the jump of a scalar is defined as a vector. With the definitions in (4.46) and recalling that for any edge $\boldsymbol{n}^{+}=-\boldsymbol{n}^{-}$, it is possible to transform (4.45) into

$$\sum_{K\in\mathcal{T}_h}\int\limits_K \boldsymbol{\nabla}\phi\cdot\boldsymbol{\nabla}\varphi\,\mathrm{d}K-\sum_{e\in\mathcal{E}_h^{\mathrm{I}}}\int\limits_{\Gamma_e}\{\!\{\boldsymbol{\nabla}\phi\}\!\}\cdot[\![\varphi]\!]\,\mathrm{d}\Gamma_e-\sum_{e\in\mathcal{E}_h^{\mathrm{I}}}\int\limits_{\Gamma_e}[\![\boldsymbol{\nabla}\phi]\!]\{\!\{\varphi\}\!\}\,\mathrm{d}\Gamma_e$$

$$-\sum_{e\in\mathcal{E}_h^{\mathrm{N}}}\int\limits_{\Gamma_e}\boldsymbol{\nabla}\phi\;\varphi\cdot\boldsymbol{n}\,\mathrm{d}\Gamma_e+\sum_{e\in\mathcal{E}_h^{\mathrm{D}}}\int\limits_{\Gamma_e}\sigma_e\;\phi\varphi\,\mathrm{d}\Gamma_e=\sum_{K\in\mathcal{T}_h}\int\limits_K f\varphi\,\mathrm{d}K. \tag{4.47}$$

This method is referred to as a *symmetric* interior penalty method as the definitions in (4.46) render the final weak formulation (4.47) symmetric. This symmetry is advantageous as more efficient iterative linear algebra solvers such as the conjugate gradient method may be used to solve the resulting linear system. The edge terms in (4.47) are referred to as flux terms as they pass "information" from neighboring cells, which would otherwise be completely independent. Additionally, assuming the classical solution to (4.42) is smooth and continuous, then as the mesh is refined the discrete discontinuous solution should approach the real continuous solution. The jump terms may thus be interpreted as penalties, since they are all identically zero for the continuous solution. As discussed in [81], for the method to be stable an additional penalty term

$$J(\phi,\varphi)\;=\;\sum_{e\in\mathcal{E}_h^{\mathrm{I}}}\int\limits_{\Gamma_e}\sigma_e\,[\![\phi]\!][\![\varphi]\!]\,\mathrm{d}\Gamma_e \tag{4.48}$$

must be introduced to the left-hand-side of (4.47). This additional term penalizes the jumps across cells and forces the solution to be more “continuous” . The jump penalty parameter σ_e over an edge e is defined as

$$\sigma_e = \frac{1}{2}\{\frac{p^+(p^+ + 1)}{h^+} + \frac{p^-(p^- + 1)}{h^-}\} \tag{4.49}$$

where Ω_e^+ and Ω_e^- denote the two cells which share the edge, while p^+ and p^- refer to the polynomial approximation orders in each cell respectively. In this work this is constant for all cells with $p = 1$. Additionally, h^+ and h^- are an estimate of the length of the cell, normal to the edge. These can be approximated by the area of the cell divided by the length of the edge, i.e. $h^{\pm} = |\Omega_e^{\pm}| \,/\, |e|$, where $|\Omega_e^{\pm}|$ is the area of each cell and $|e|$ is the length of the edge.

5. Multigrid Methods

5.1. Numerical Linear Algebra Solvers

Most numerical schemes used to solve differential equations, despite the choice of discretization, result in large linear systems of equations of the form

$$A\boldsymbol{x} = \boldsymbol{b}. \tag{5.1}$$

Linear systems arising from finite element methods are typically very sparse and symmetric for certain problems. They may also possess other favourable properties such as positive-definiteness, which can be exploited in solving the equations numerically. Theory and implementation of most common numerical linear algebra techniques can be found in any reference on numerical analysis/methods (see for example [19]).

Direct methods, such as Gauss elimination, have been traditionally used to solve (5.1). Additionally, variants such as LU factorization, LL^TCholesky factorization for symmetric matrices, and Crout factorization for banded matrices have also been applied. These methods are robust and fast for smaller systems. However, these methods scale as $O(n^3)$ for full systems, where n is the number of degrees of freedom, and thus becomes prohibitive at larger scales. Nonetheless, they remain extremely popular in the computational community, with modern sparse and parallel implementations such as the open-source Unsymmetric MultiFrontal package (UMFPACK)[28].

Iterative techniques provide an alternative to direct methods, where successively better approximations to the solution are produced until a convergence criterion is met. These methods allow for larger systems to be solved. Although the work required for using these methods scales better than for direct methods, they are not unconditionally stable and all require a sufficiently *good* initial approximation to converge. The success of these methods typically depends on matrix properties such as the spectral radius, which is typically not known beforehand. These techniques can be split into two groups: stationary and Krylov subspace techniques.

Stationary methods such as Jacobi, Gauss-Seidel, successive over relaxation (SOR) and symmetric successive over relaxation (SSOR) are easy to implement in both full and sparse systems; although parallelization is not always trivial. Krylov subspace methods include, amongst others: the conjugate gradient method (CG) for symmetric positive-definite systems and the general minimal residual method (GMRES) and the biconjugate gradient stabilized method (BiCGSTAB) for non-symmetric matrices. Preconditioners based on stationary iterative methods or approximate matrix decomposition are typically used to improve the convergence rates of Krylov methods.

The ever increasing size of problems being tackled in the computational community and the pitfalls of traditional solvers, as discussed above, has led to the emergence and much gained popularity of a new class of solvers called multigrid methods (MG). This class of solvers was initially developed by Federenko [34] for elliptic boundary value problems and later extended by Brandt [16]. Extensions of these methods to handle parabolic, hyperbolic and mixed type systems has broadened the range of applications. The main advantage of these methods is that they theoretically scale as $O(n)$, hence their increasing popularity in many fields - especially in computational fluid dynamics (see for example [88]) .

The simulation of viscoelastic flows is known to be computationally expensive, so the incorporation of an efficient solver is key when attempting to extend these algorithms to handle realistic geometries and 3D flows (see Lee [57]). We seek to similarly develop an efficient and stable method to accelerate the algorithm presented in chapter 4 through the incorporation of a MG method.

5.2. Multigrid Methods

5.2.1. Fundamental Principles

When stationary iterative methods are applied to solving discretized operators, which arise from finite element schemes, they tend to converge slowly. Furthermore, they exhibit deteriorating convergence rates as the discretization size decreases, i.e. $h \to 0$. If the solution is represented as a Fourier series it can be shown that a stationary iterative method will decrease the residual in the higher frequencies of the series faster than the lower frequencies. These stationary iterative methods can then be seen to act as smoothers, rapidly reducing the higher frequency residuals. This is shown in many introductory texts on MG methods (see for example [90]), where typically Fourier analysis is applied to a 1D finite difference discretization of the Poisson equation with periodic boundary conditions.

Spatial discretization of a domain often consists of levels of refinement, where cells are divided into smaller cells in order to improve the resolution of the method, as shown in figure 5.1. Since working on a coarse mesh is less computationally expensive, the principle of MG methods is to use the coarser mesh to represent the smooth components of the solution, i.e. the lower frequencies in the Fourier representation, and the finer mesh to resolve the higher frequencies. The higher frequencies may be cheaply resolved by using stationary iterative methods acting as smoothers to decrease the higher frequencies of the residual. The smooth residual can then be represented on a coarser mesh, where it is cheaper to work with. The above procedure is the essence of multigrid methods as presented in Brandt [16]. The following sections will discuss the details of this method and its application to the GOB problem.

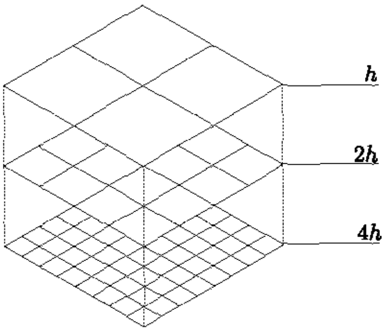

Figure 5.1. – Family of meshes with three levels of refinement h, $2h$ and $4h$. Refinement is performed by subdividing each cell into four equal subcells.

5.2.2. Two-Level Multigrid Methods

To illustrate MG methods initially two levels of discretization will be considered: a coarse mesh $2h$ and a fine mesh h. If we then consider the linear system (5.1) described on each level as $\boldsymbol{A}_{2h}$ and $\boldsymbol{A}_h$ respectively, we may describe a typical two-level MG cycle consisting of three steps :

1. **Pre-smoothing**
   On the fine mesh h, the initial guess $\boldsymbol{x}_h^0$ is smoothed N_1 times using a stationary iterative solver $\hat{S}_1$ to produce

   $$\boldsymbol{x}_h^{N_1} = \hat{S}_1^{\,N_1} \boldsymbol{x}_h^0. \tag{5.2}$$

   A Gauss-Seidel or Jacobi solver are popular options for smoothers.

2. **Coarse-Grid Correction (CGC)**
   Initially the residual on the fine mesh, $\boldsymbol{r}_h = \boldsymbol{b}_h - \boldsymbol{A}_h \boldsymbol{x}_h^{N_1}$, is determined. Using the restriction operator $\hat{I}^{2h\leftarrow h}$, the residual is transfered to the coarse grid $2h$, where the system is solved for coarse error $\boldsymbol{e}_{2h}$ by considering

   $$\boldsymbol{A}_{2h} \boldsymbol{e}_{2h} - = \hat{I}^{2h\leftarrow h} \boldsymbol{r}_h. \tag{5.3}$$

   Using the prolongation operator $\hat{I}^{h\leftarrow 2h}$, the coarse-grid error is transfered to the fine mesh h, where it is used to correct $\boldsymbol{x}_h^{N_1}$, resulting in

   $$\boldsymbol{x}_h^{N_1+1} = \boldsymbol{x}_h^{N_1} + \hat{I}^{h\leftarrow 2h} \boldsymbol{e}_{2h}. \tag{5.4}$$

3. **Post-Smoothing**
   The corrected solution is then smoothed N_2 times using a stationary solver $\hat{S}_2$ to produce the final solution

   $$\boldsymbol{x}_h^{N_1+N_2+1} = \hat{S}_2^{N_2} \boldsymbol{x}_h^{N_1+1}. \tag{5.5}$$

The above described cycle is then repeated until the residual or difference between cycles falls below a predefined limit. Alternatively, the multigrid cycle can be incorporated as a preconditioner within a global solver, where the inverse of the global system is approximated by a number of multigrid cycles within each iteration. This can be extremely efficient when acting in combination with a Krylov solver. Of particular importance in the above cycle is the choice of smoothers $\hat{S}_1$and $\hat{S}_2$. They should be chosen to exploit any advantageous properties of the system, such as symmetry. Typically the pre- and post-smoothers are chosen to be the same and the number of smoothing steps is set at 1 or 2.

5.2.3. General Multigrid Methods and V-Cycles

To extend the method above to handle a general number of levels of refinement, a recursive formulation is favoured. The simplest MG cycle is known as a V-cycle, wherein the two-level algorithm in section §5.2.2 is modified such that the coarse error in step 2 is not solved for exactly, but rather an approximation is made by an additional two-level cycle over that mesh and one even coarser. This process is carried on recursively until the coarsest mesh is reached, where the system is solved exactly using any traditional solver.

Psuedo-code for the V-cycle is presented in algorithm 5.1. Within this algorithm we assume the following notation: consider a family of N meshes $\{\Omega_i \mid i = 1..N\}$ and also a family of discretized systems $\{\boldsymbol{A}_i \mid i = 1..N\}$. With each of these systems there corresponds a pre-smoother $\{\hat{S}_{1i}^{N_1} \mid i = 2..N\}$ and post-smoother $\{\hat{S}_{2i}^{N_2} \mid i = 2..N\}$, each performing N_1 and N_2 smoothing steps respectively. Additionally, consider a family of restriction $\{\hat{I}^{i \leftarrow i+1} \mid i = 1..N-1\}$ and prolongation $\{\hat{I}^{i \leftarrow i-1} \mid i = 2..N\}$ operators between each pair of consecutively refined levels. Lastly, on a global level, consider a family of restriction and solution vectors $\{\boldsymbol{r}_i \mid i = 1..N\}$ and $\{\boldsymbol{x}_i \mid i = 1..N\}$ respectively. A single V-cycle then approximates the solution of the system $\boldsymbol{A}_N \boldsymbol{x}_N = \boldsymbol{b}_N$ as $\boldsymbol{x}_N \leftarrow$ VCYCLE$(N, 1, \boldsymbol{x}_N^0, \boldsymbol{b}_N)$, where $\boldsymbol{x}_N^0$ is the best known approximation of the solution.

A diagram representing a single V-cycle for a mesh with three levels of refinement is shown in figure 5.2. In light of this diagram the name “V-cycle” is also more apparent. Additionally, there exist variants of the V-cycle such as the W-cycle, where 2 coarse-grid corrections are performed successively. Despite the heavier computational cost of the W-cycle it has been shown to converge faster than the V-cycle in some situations. Alternatively, there is also the F-cycle, appropriate when good initial approximations are not available; a scenario which may cause the V and W-cycles to diverge. In this cycle, coarser level solutions are projected to finer meshes where they serve as initial approximations.

Algorithm 5.1 Recursively Defined Multigrid V-Cycle

```
function VCycle($l, l_{low}, \boldsymbol{x}_l, \boldsymbol{r}_l$)

    Input
      $l$ - Current Level,    $l_{low}$ - Lowest Refinement Level
      $\boldsymbol{x}_l$ - Current Level Solution,    $\boldsymbol{r}_l$ - Current Level Defect

    if $l = l_{low}$ then
        return $\boldsymbol{x}_l \leftarrow \boldsymbol{A}_l^{-1}\boldsymbol{r}_l$                ▷ Solve System on Coarsest Mesh
    else
        $\boldsymbol{x}_l \leftarrow \hat{S}_{1l}^{N_1}\boldsymbol{x}_l$                              ▷ Pre-Smoothing
        $\boldsymbol{r}_l \leftarrow \boldsymbol{r}_l - \boldsymbol{A}_l\boldsymbol{x}_l$                              ▷ Get Residual
        $\boldsymbol{r}_{l-1} \leftarrow \hat{I}^{l-1 \leftarrow l}\boldsymbol{r}_l$                         ▷ Restrict the Residual
        $\boldsymbol{x}_{l-1} \leftarrow 0$                             ▷ Zero the Next Coarse Solution
        $\boldsymbol{x}_l \leftarrow \boldsymbol{x}_l + \hat{I}^{l \leftarrow l-1}$VCYCLE$(l-1, l_{low}, \boldsymbol{x}_{l-1}, \boldsymbol{r}_{l-1})$    ▷ CGC
        $\boldsymbol{x}_l \leftarrow \hat{S}_{2l}^{N_2}\boldsymbol{x}_l$                              ▷ Post-Smoothing
        return $\boldsymbol{x}_l$
    end if
end function
```

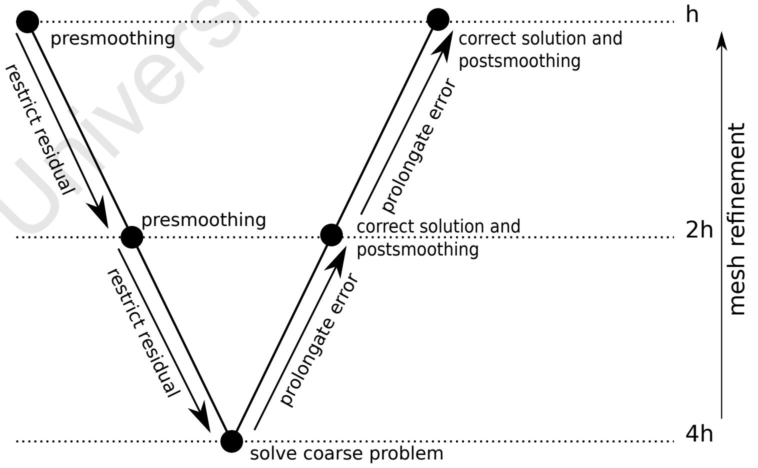

Figure 5.2. – Diagram representing a single V-cycle for a mesh with three levels of refinement h, $2h$ and $4h$.

The two fundamental components of the multigrid method which determine the convergence and success are: the restriction and prolongation operators which move solutions between levels of refinement and the smoothers acting on each level. The first will be discussed in section §5.3 and the second in section §5.5, with specific relevance to mixed methods in solving the coupled nonlinear momentum and constitutive equations and also the more typical elliptic system which arises from the projection step. The implementation of parallelism in multigrid methods will be discussed in section §5.7, while the treatment of non-uniformly refined meshes will be dealt with in section §5.8.

5.3. Restriction and Prolongation Operators

As can be seen in algorithm 5.1, solutions must be frequently transferred between two consecutively refined meshes over the same domain Ω. This requires some form of interpolation, which in the context of finite elements will be provided by the same shape functions which interpolate the solution across the domain.

Consider a segment of two consecutively refined 1D meshes in figure 5.3, where linear shape functions are shown above each node. The coarse mesh will be defined using the set of nodal points $\{\xi_i^{2h} \mid i = 1..N_{2h}\}$, while the fine mesh is defined using the corresponding set $\{\xi_i^h \mid i = 1..N_h\}$. A finite-dimensional space is associated with each of these meshes. For the coarse mesh this will be denoted as $\mathcal{V}_{2h}$, with the set $\{\Phi_i^{2h} \mid i = 1..N_{2h}\}$ of shape functions forming its basis, and similarly $\mathcal{V}_h$ with basis $\left\{\Phi_i^h \mid i = 1..N_h\right\}$ for the fine mesh. It should be recalled that these basis functions possess the Kronecker delta property with regards to their correspondence to the set of nodal points, expressed as

$$\Phi_i^{2h}(\xi_j^{2h}) = \delta_{ij} \tag{5.6}$$

for the coarse mesh. Numerically, these solutions are represented as a vector of coefficients for each of the basis functions, i.e. $\boldsymbol{a}_h \in \mathbb{R}^{\mathrm{N_h}}$ and $\boldsymbol{b}_{2h} \in \mathbb{R}^{N_{2h}}$ for the fine and coarse mesh respectively.

5.3.1. Prolongation Operators

The prolongation operator $\hat{I}^{h\leftarrow 2h}$ may be defined as the operator which produces the vector solution $\boldsymbol{a}_h = \begin{pmatrix} a_1 & a_2 & \cdots & a_{N_h} \end{pmatrix} \in \mathbb{R}^{N_h}$, corresponding to the fine mesh h, given a vector $\boldsymbol{b}_{2h} = \begin{pmatrix} b_1 & b_2 & \cdots & b_{N_{2h}} \end{pmatrix} \in \mathbb{R}^{N_{2h}}$ such that

$$u_h(x) = \sum_{i=1}^{N_h} a_i \Phi_h^i(x) = u_{2h}(x) = \sum_{i=1}^{N_{2h}} b_i \Phi_{2h}^i(x) \;\; \forall x \in \Omega \tag{5.7}$$

holds throughout the domain. Due to the definition of these nodal finite element spaces, it holds that $\mathcal{V}_{2h} \subset \mathcal{V}_h$. Thus any basis function in $\mathcal{V}_{2h}$ can be expressed as a linear

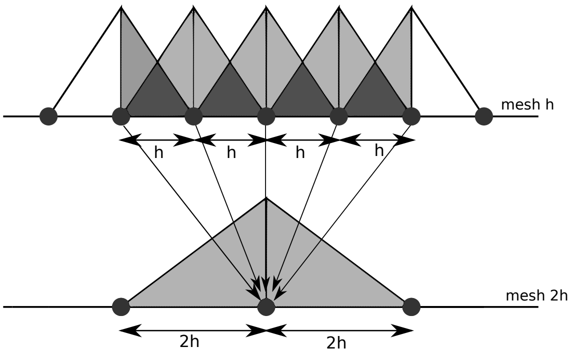

Figure 5.3. – A segment of 1D coarse mesh $2h$ and a once refined mesh h with linear finite element shape function. The dependence of the degree of freedom at the middle node on the coarse mesh is indicated with arrows to the degrees of freedom on the fine mesh.

combination of the basis functions of $\mathcal{V}_h$ as

$$\Phi_{2h}^{i}(x) = \sum_{k=1}^{N_h} \gamma_{(k,i)} \Phi_h^k(x). \tag{5.8}$$

To determine the coefficients of this linear relationship, the nodal points of the fine mesh are inserted into the relation (5.8) and by using the Kronecker delta property (5.6), we obtain

$$\begin{aligned} \therefore \Phi_{2h}^{i}(\xi_j^h) &= \sum_{j=1}^{N_h} \gamma_{(k,i)} \Phi_h^k(\xi_j^h) \\ &= \sum_{j=1}^{N_h} \gamma_{(k,i)} \delta_{kj} = \gamma_{(j,i)}. \end{aligned} \tag{5.9}$$

Thus in light of the requirement (5.7) and the definitions of $\gamma_{(i,j)}$ in (5.9), the expression (5.10) below follows.

$$\begin{aligned} u_{2h}(x) &= \sum_{i=1}^{N_{2h}} b_i \Phi_{2h}^i(x) \\ &= \sum_{j=1}^{N_h} \left(\sum_{i=1}^{N_{2h}} \gamma_{(j,i)} b_i \right) \Phi_h^j(x) \end{aligned} \tag{5.10}$$

Furthermore, by reconciling this expression with the expansion of u_h in (5.7), we may express the coefficients a_j as

$$a_j = \sum_{i=1}^{N_{2h}} \gamma_{(j,i)} b_i. \tag{5.11}$$

From (5.11) above, it follows that the prolongation operator $\hat{I}^{h\leftarrow 2h}$ can be expressed as a matrix $\left[\hat{I}^{h\leftarrow 2h}\right]_{(i,j)} \in \mathbb{R}^{N_h \times N_{2h}}$, defined as

$$\boldsymbol{a}_h = \left[\hat{I}^{h\leftarrow 2h}\right] \boldsymbol{b}_{2h} \quad \text{where} \left[\hat{I}^{h\leftarrow 2h}\right]_{(i,j)} = \gamma_{(i,j)}. \tag{5.12}$$

This matrix will be very sparse due to the compact support of the shape functions. This can be seen in (5.3), where the value at the node i will only influence the values of the five indicated nodes on the finer mesh and vice versa. This renders the mesh transfer action cheap to execute and the transfer matrix cheap to store. The above definition is general enough to hold for other order nodal based shape functions and discontinuous shape functions, and requires little modification to handle more general elements. Some smoothing will occur from this procedure and has led to some authors using alternative prolongation operators where, for example, bias is introduced according to a convective field for hyperbolic problems.

5.3.2. Restriction Operator

In addition to moving solutions from coarser to finer meshes, the reverse operation is also required within the MG method. This is accomplished by a restriction operator $\hat{I}^{2h\leftarrow h}$, defined as the adjoint of the prolongation operator, which we express as

$$\left(\boldsymbol{a}_h, \hat{I}^{h\leftarrow 2h}\boldsymbol{b}_{2h}\right)_{\mathbb{R}^{N_h}} = \left(\hat{I}^{2h\leftarrow h}\boldsymbol{a}_h, \boldsymbol{b}_{2h}\right)_{\mathbb{R}^{N_{2h}}} \quad \forall \boldsymbol{a}_h \in \mathbb{R}^{N_h}\ ,\ \boldsymbol{b}_{2h} \in \mathbb{R}^{N_{2h}}. \tag{5.13}$$

Since these operators are linear, it is sufficient to show that (5.13) holds for a general pair of basis vectors $\boldsymbol{e}_h^i$ and $\boldsymbol{e}_{2h}^j$ to make the definition of the restriction operator concrete. Substituting these basis vectors into (5.13) and using the matrix definition of the prolongation operator yields[1]

$$\begin{aligned} \sum_k \sum_l \delta_{ik}\gamma_{(k,l)}\delta_{lj} &= \sum_k \sum_l \left[\hat{I}^{2h\leftarrow h}\right]_{kl} \delta_{li}\delta_{kj} \\ \therefore \left[\hat{I}^{2h\leftarrow h}\right]_{ji} &= \gamma_{(i,j)}. \end{aligned} \tag{5.14}$$

It can now be seen that the restriction operator is simply the transpose of the prolongation operator and hence no additional construction or memory allocation is required.

---

[1] Contraction with a basis vector is equivalent to the action of Kronecker delta. An example of this can be seen in the expression below.

$$\boldsymbol{a} \cdot \boldsymbol{e}_h^i = \sum_k a_k (e_h^i)_k = \sum_k a_k \delta_{ik}$$

5.4. Nonlinear Problems

Multigrid methods have been used successfully to tackle a variety of nonlinear problems. The Newton-Raphson method is typically used to handle nonlinearity and can be combined with multigrid methods in one of two ways:

1. **Multigrid-Newton Method**
   In this method the multigrid method is applied directly to the nonlinear problem and the smoother is replaced with a nonlinear variant, such as the Newton-Vanka smoother. However, the full solution is required on each level for the linearization terms and hence the full approximation storage (FAS) formulation is then applied in these instances.

2. **Newton-Multigrid Method**
   In this method the nonlinearity is first treated using a Newton-Raphson method and then MG methods are used to solve the resulting linearized system.

Since the GOB problem is time-dependent, and generally good initial guesses are available, few Newton iterations are required for each time step. This makes the Newton-Multigrid method a more attractive option, as it is efficient and easier to implement.

5.5. Smoothers

5.5.1. Elliptic Step

The choice of smoother in a MG method can severely affect the convergence properties of the resulting method. Although typically a few iterations of a stationary iterative solver are used to this effect, special consideration needs to be made for the matrix block structure that arises in the elliptic step of the pressure-projection method (see section §4.2)

$$\begin{pmatrix} J_{uu} & J_{u\tau} \\ J_{\tau u} & J_{\tau\tau} \end{pmatrix} \begin{pmatrix} \boldsymbol{\delta u} \\ \boldsymbol{\delta \tau} \end{pmatrix} = \begin{pmatrix} -R_u \\ -R_\tau \end{pmatrix}. \tag{5.15}$$

The diagonal dominance of a matrix will determine the rate of convergence of a stationary iterative solver and hence the efficiency when used as a smoother. The off-diagonal blocks in (5.15) will thus render this problem very inefficient for traditional smoothers. Various ways of dealing with this problem have been proposed in the literature, with a few described below:

- **Schur complement**
  The mixed problem is solved with a Schur complement technique, on which a MG solver is used. This is typically used as a preconditioner to another global method.

- **Outer Gauss-Seidel**
  In systems with fairly weak coupling, i.e. there is diagonal dominance with respect to the block structure, a block-wise Gauss-Seidel iterative scheme may be applied, expressed as

$$\begin{aligned} J_{uu}\boldsymbol{\delta u}^{k+1} &= -R_u - J_{u\tau}\boldsymbol{\delta\tau}^{k} \\ J_{\tau\tau}\boldsymbol{\delta\tau}^{k+1} &= -R_\tau - J_{\tau u}\boldsymbol{\delta u}^{k+1}. \end{aligned} \tag{5.16}$$

  A MG method may then be applied to each of the systems using a traditional smoother.

- **Vanka Smoother**
  The Vanka smoother acts as a block Gauss-Seidel method, where all degrees of freedom on a cell are treated simultaneously. These degrees of freedom are extracted for each cell and the resulting cell-sized system is solved using Gauss elimination. The smoother is described in algorithm 5.2, where we assume the following notation: the global solution is represented by $\boldsymbol{x}_g$ and the local solution on the k^{th} cell is represented by $\boldsymbol{x}_c^k$. Additionally, a projection operator from the global to cell system is defined as $\hat{P}^{c\leftarrow g}$ and the reverse operator as $\hat{P}^{g\leftarrow c}$.

  A single step of the Vanka smoother consists of treating each cell on a particular level of refinement once. This type of smoother is particularly efficient at solving saddle-point problems, such as those that arise in incompressible flow. This is because only small cell-sized indefinite systems need to be solved. The highly parallelizable nature of this smoother is an additional advantage.

From a number of preliminary tests of solving the generalized Oldroyd-B system, it was observed that the Vanka smoother had the best performance of the above options. However, at higher We numbers the increased convection in the constitutive equation results in a restrictive maximum time step. It is expected that by using a better ordering of cells, i.e. streamline ordering, or by treating larger patches of cells at a time, this problem may be alleviated. Such a study will hopefully form part of future work.

5.5.2. Projection Step

When applying the MG method to solving the projection step, 2 iterations of a SSOR solver with the relaxation parameter set at 1.2 is chosen to act as a smoother. This choice will exploit the symmetry of the system and has been shown extensively in the literature to be efficient and robust for this common problem.

5.6. Coarse Solver

During a V-cycle of a MG method, the system on the coarsest mesh must be solved *exactly*. Since multiple V-cycles will be completed during a single matrix solve, it is

Algorithm 5.2 Vanka Smoother Algorithm

```
function VANKA($l$)

    input
        $l$ - Refinement Level

    for all cells $k$ with refinemenet level $l$ do
        $\boldsymbol{x}_c^k \leftarrow \hat{P}^{c\leftarrow g}\boldsymbol{x}_g$                                          ▷ Extract Local Cell Solution
        $\boldsymbol{x}_c^{k'} \leftarrow \left(\hat{P}^{c\leftarrow g}A\right)^{-1}\hat{P}^{c\leftarrow g}\left(\boldsymbol{b} - A\boldsymbol{x}_g\right)$        ▷ Solve Local Cell System
        $\boldsymbol{x}_g \leftarrow \boldsymbol{x}_g + \hat{P}^{g\leftarrow c}\left(\boldsymbol{x}_c^{k'} - \boldsymbol{x}_c^k\right)$            ▷ Update Global Solution
    end for
end function
```

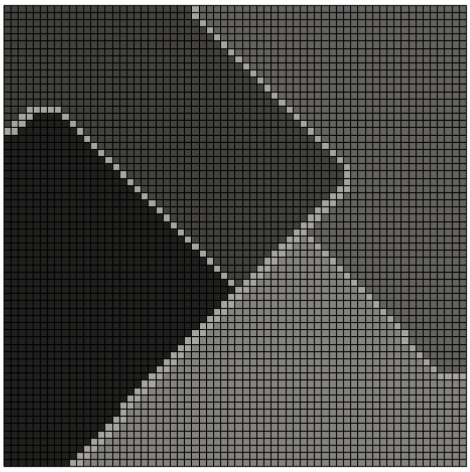

Figure 5.4. – Partitioning of a square mesh into four, using the METIS library. Each segment is represented by a different shade with all cells with neighbors belonging to different partitions placed in a separate partition.

advantageous to initially factorize the coarse mesh matrix using an LU factorization and then cheaply solve the system for various right-hand-side vectors. The coarsest level may be extremely coarse, consisting of only a few elements for simple geometries, or fairly large for more complex geometries. In the latter case, a sparse LU factorization is carried out using the UMFPACK library. This is done for the problems of flow over a cylinder section §6.1 and pulsatile flow in a stenotic channel in chapter 7.

5.7. Parallelization

Parallelization of MG methods can be highly successful, although not trivial. Most of the base operations of mesh transference and residual evaluation consists of sparse-matrix vector multiplications, which are easily parallelizable. However, the most time consuming element is the action of the smoother. Most stationary solvers are not easily parallizable, with the exception of the Jacobi method. The Vanka smoother, presented in section §5.5 is on the other hand a good candidate for parallelization. Furthermore, since its action requires a large number of small problems to be solved, this is an attractive problem for modern computer architectures such as GPUs.

The Vanka smoother is parallelized using the Intel TBB [80] libraries, by allowing multiple threads to visit cells simultaneously. We avoid the need to synchronize the updating of the global solution by initially partitioning the mesh into as many parts as there are available threads. Then all cells which have neighbors belonging to different partitions are set as a separate partition. This is shown in figure 5.4 for a square mesh and four threads. Each thread then visits only cells belonging to its partition. Once all the threads have completed, the cells between partitions - which were set as a separate partition - are visited by a single thread. The partitioning of the mesh is done using the METIS library [54].

5.8. Non-Uniformly Refined Meshes

Despite the improvement in performance of MG preconditioning, problems with complex features may require very fine meshes in regions of high activity. This is accomplished by refining cells in the region of this activity, while leaving the remaining mesh coarse to reduce the computational cost. This is illustrated in figure 5.5, where a square mesh is refined only in the top right corner. This non-uniform refinement introduces hanging nodes in these meshes, as indicated in figure 5.5 (a) and requires additional treatment when continuous elements are chosen. Continuity of these fields is enforced by setting the solution at those nodes as in the coarser neighbouring cell. In the context of multigrid methods, additional treatment is required as described in [50] for continuous and [53]

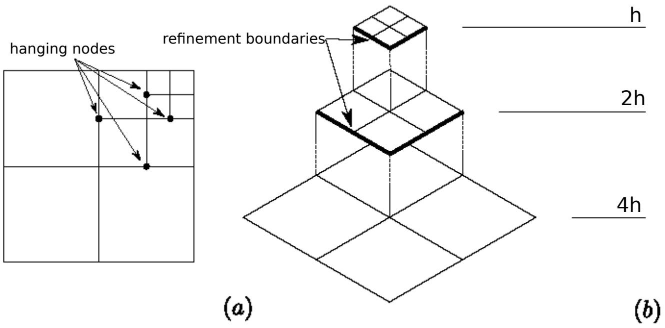

Figure 5.5. – Non-uniformly refined mesh with a twice refined upper left corner. (a) The active or global level with indicated hanging-nodes. (b) Cells belonging to each level of refinement $4h$, $2h$ and h.

for discontinuous elements; both of which are required for this problem. For the sake of completeness and clarity, the general principle of this treatment will be presented below[2].

In situations as in figure 5.5, we refer to a level of refinement as all cells which have been refined the same number of times, as shown in (b). Additionally we refer to the active level of cells as those that at each point are most refined, as shown in (a). In the MG method, the smoother then acts only on cells of the same level, referred to as local-smoothing. The refinement boundaries are treated as Dirichlet boundaries, using the coarser solution at these boundaries. Additionally, when transferring solutions between refinement levels, the flux through the refinement boundary must to added to the solution and residual vector. This interpretation is most easily seen in the DG context where the jump terms over these edges directly constitute flux. This requires a slight modification to the V-cycle (algorithm5.1) and the additional storage of flux matrices for each pair of consecutively refined meshes. These flux matrices are however very sparse, as they involve only degrees of freedom around these refinement boundaries.

Unfortunately an additional complication arises, namely: the finest mesh does not cover the entire domain. Hence a MG cycle would not resolve the solution in all regions. This issue may be treated by using a Full Approximation Storage (FAS) formulation. An attractive alternative is to also construct the system of equations on the active level of cells, i.e. as though without MG. This system can then act as a go-between when transferring residuals and solutions between levels. The large global system can be solved with an outer iterative solver, where each step is preconditioned with a number of cycles of the MG method. The residual at each outer-step exists on the active level, and hence the entire domain. During preconditioning, a V-cycle would pass the residual from a finer to a coarser mesh but only over areas where they overlap. In areas where they do not

---

[2] The full details are available in [50] and [53]. These treatments were suggested by the contributors to the finite element library used in this work, DEAL.II . Hence incorporation into the algorithm is additionally described in the user manual with only slight modifications required to handle problems with multiple fields.

overlap, the cells on the coarser mesh are active and hence the global residual is present. Similarly, after each MG cycle the global solution can be extracted from the active level and passed to the outer solver.

A summary of this procedure is shown in algorithm 5.3, where an outer Richardson solver is used. In this algorithm the following notation is assumed: let A represent the "global" system matrix, i.e. on the active level, and $\boldsymbol{x}_i$ represent the global solution at the i^{th} Richardson iteration. Similarly, let $\boldsymbol{b}$ be the global right-hand-side vector. A superscript index j on any of these quantities denotes their correspondence to the j^{th} level of refinement, where n is the highest and 0 is the coarsest mesh.

More complex outer iterative solvers, such as GMRES or BiCGSTAB, may be used in place of the Richardson solver in algorithm 5.3. In particular, the BiCGSTAB solver will be used in this work due to the non-symmetric global system.

Algorithm 5.3 Multigrid Algorithm - Outer Richardson Solver

```
$m \leftarrow 0$
while $|\boldsymbol{x}_m - \boldsymbol{x}_{m-1}| < \varepsilon_{tol}$ do
    $m \leftarrow m + 1$
    $A\boldsymbol{x}_m = \boldsymbol{b} - A\boldsymbol{x}_{m-1}$                          ▷ one step of Richardson's method
    ↳ $\{\ \boldsymbol{b}^n \quad \boldsymbol{b}^{n-1} \cdots \boldsymbol{b}^0\ \} \leftarrow (\boldsymbol{b} - A\boldsymbol{x}_{m-1})$     ▷ transfer residual to active cells
      $\{\ \boldsymbol{x}^n \quad \boldsymbol{x}^{n-1} \cdots \boldsymbol{x}^0\ \} \leftarrow \boldsymbol{0}$                     ▷ zero solution on all levels
      VCYCLE($n$)                                           ▷ one V-cycle starting on finest level
      $\boldsymbol{x}_m \leftarrow \{\ \boldsymbol{x}^n \quad \boldsymbol{x}^{n-1} \quad \ldots \quad \boldsymbol{x}^0\ \}$           ▷ extract all active cell solutions
end while
```

Part III.

Results and Conclusions

6. Benchmark Problems

With the introduction of the new numerical method in part 2, validation should first be performed before any confidence may be placed on results produced by this method. For simple models this is often done by the *method of constructed solutions*, where a problem with a known/manufactured analytical solution is solved. Unfortunately for more complicated models, such as the GOB model, this is not always possible in non-trivial geometries. For this reason a set of benchmark problems are solved which have been dealt with previously in the literature, and thus provide a basis to compare the validity, accuracy and stability of a newly developed numerical scheme.

The generalized Oldroyd-B model is a relatively recent model and hence little literature exists to compare to. Hence we will focus on popular benchmark problems for the Oldroyd-B model to test the purely viscoelastic limit of our model. We can then extend the benchmark problems to the generalized model and observe the qualitative difference in behaviour. The first problem we consider is flow over a confined cylinder: a steady-state problem on which there exists extensive literature. The second problem is the start-up driven cavity problem, which although less popular, will help to illustrate the stability of our method as well as provide a time-dependent case study.

6.1. Flow Over a Cylinder

6.1.1. Introduction

An established benchmark problem for the numerical simulation of viscoelastic flows is creeping flow over a confined cylinder in a channel. This problem was initially proposed in [18]. Apart from acting as a basis for comparison, this problem has industrial applications in heating and cooling systems as well as the food processing industry (see [1]). Although this problem has a relatively simple geometry with no singularities, it is a stringent test for any numerical scheme. This is due to the difficulty in capturing the very steep stress boundary layer which develops on the cylinder surface, as well as the longitudinal stress wake which occurs behind the obstruction. In the literature review that follows only works concerning the Oldroyd-B model will be discussed.

In much of the literature to date, the focus has been on solving this problem for ever increasing Weissenberg number using different schemes and methods. However it has been observed by most authors that numerical schemes typically fail for We $\gtrsim 0.7/0.8$.

After this point the algorithms fail to converge, or show great mesh sensitivity, where the loss of convergence tends to first occur in the wake of the cylinder. In the numerical works where mesh convergent results were obtained at higher We, the accuracy of the solutions is typically questioned by the authors. These numerical issues are a good example of the high Weissenberg number problem faced in computational rheology (see section §2.8).

A study of this problem within a finite element context may be found in the paper of Fan *et.al.* [31], where a h-p FE method in combination with a Galerkin/least-squared formulation and SUPG stabilization for the constitutive equation was developed and applied. In the work of Kim *et.al.* [56], a FE method based on a DEVSS-G/SUPG scheme was used on very refined meshes. In this work a limiting $\mathrm{We} = 0.7$ was observed. Alternatively, an approach using the log-conformation tensor formulation may be found in the work of Coronado *et.al.* [27], where a DEVSS-TG/SUPG scheme was used to simulate flow at very high We. However, despite the increased stability of the log-conformation formulation, mesh convergent results were not obtained for $\mathrm{We} > 0.6$.

Approaches based on finite volume methods (FV) may be found in the paper of Alves. *et.al.* [1], where an upwinded FV scheme was used and in Dou *et.al.* [30], where an unstructured FV scheme using an explicit discrete vorticity field was used. In both these works, compatibility between the velocity and stress spaces is ensured through a DAVSS scheme. Although they achieved converged solutions for $\mathrm{We} = 1.8$, they also stated that the large amount of adaptive viscosity at these values of We renders the accuracy of the scheme questionable. Spectral methods were used in the work of Owens *et.al.* [68], where a new locally upwinded spectral method was developed. More recently an extended finite element method (XFEM) was used in conjunction with a DEVSS-G/SUPG scheme in the work of Choi *et.al.* [22].

A very different approach was used by Hulsen *et.al.* [46], where the stress was treated in a stochastic manner by introducing an ensemble of configuration fields. This was then coupled to a finite element approximation of the velocity and pressure fields. However, in this work different parameters were chosen and only a single We number was considered making comparison to these results difficult.

Although these works present results on the numerical instabilities which occur, there has also been experimental work on the physical emergence of elastic instability for Boger fluids in this geometry, such as in [83] and others. A thorough review on viscoelastic flow over a cylinder may be found in chapter 9 of [70].

6.1.2. Problem Definition

We define the geometry in 2D as shown in figure 6.1, consisting of a rectangular channel of width $4r$ and a symmetrically placed cylinder of radius r. We allow for sufficiently long inlet and outlet lengths $15r$ to ensure that the boundary conditions do not influence the results. We impose fully-developed Poiseuille flow boundary conditions for the velocity and stress at the inflow boundary (A) and natural boundary conditions (see

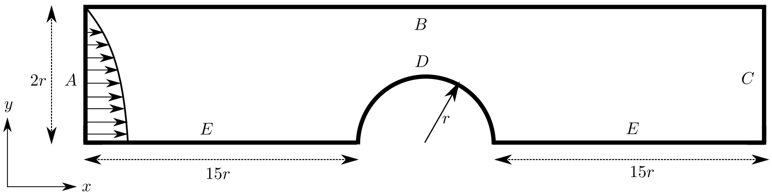

Figure 6.1. – Computational geometry of the flow over a cylinder in a channel problem

section §3.4.1) at the outflow (C). No-slip boundary conditions are applied along the channel wall (B) and the cylinder surface (D). Since the problem is symmetric around the axis of the channel, we impose a symmetry boundary $\left.\frac{\partial \boldsymbol{u}}{\partial y}\right|_{\partial\Omega_B} = \left.\frac{\partial \boldsymbol{\tau}}{\partial y}\right|_{\partial\Omega_B} = 0$ and $\boldsymbol{u} \cdot \boldsymbol{n}|_{\partial\Omega_B} = 0$ on the central channel axis (E). Analytical results for Poiseuille flow for a Oldroyd-B and generalized Oldroyd-B fluid may be found in appendix A.

Following the literature, we approximate creeping-flow by prescribing a very small Reynolds number ($\mathrm{Re} = 0.01$)[1]. We also set the ratio of the solvent to total viscosity as $\beta = 0.59$ and increment the Weissenberg number from 0.1 until the algorithm diverges. We use a transient algorithm to obtain steady-state solutions by time-stepping towards equilibrium with constant boundary conditions. The solutions were considered as converged once the L_2 norm of the difference in all fields fell beneath $10^{-6}\Delta t$. A constant time step of $\Delta t = 0.01$ was used in all simulations. To decrease the computational time, the steady-solution obtained at a lower We number was used as an initial condition for simulations at higher We. The characteristic length is set to the cylinder radius ($L = r$) and the characteristic velocity U is set as the average velocity at the inflow, both set to unity in our simulations.

6.1.3. Oldroyd-B Results

Solution Profiles

Steady solutions were obtained when using both Q_1^{disc} and Q_0^{disc} stress elements. The algorithm failed using Q_1^{disc} elements for $\mathrm{We} > 0.7$, while the solutions using Q_0^{disc} elements showed no signs of divergence in the range of considered Weissenberg numbers $0.1 \leq \mathrm{We} \leq 1.2$. However, due to the increased relaxation time at higher We, computation past this range becomes prohibitively expensive, particularly with finer meshes.

To provide a general understanding of the flow characteristics, we present solution profiles at $\mathrm{We} = 0.6$ near the cylinder in figure 6.2. In (a) the velocity magnitude is shown superimposed with a representative vector plot. The flow is not dissimilar to Newtonian

---

[1] The pressure-projection method we employ does not allow for zero Reynolds number

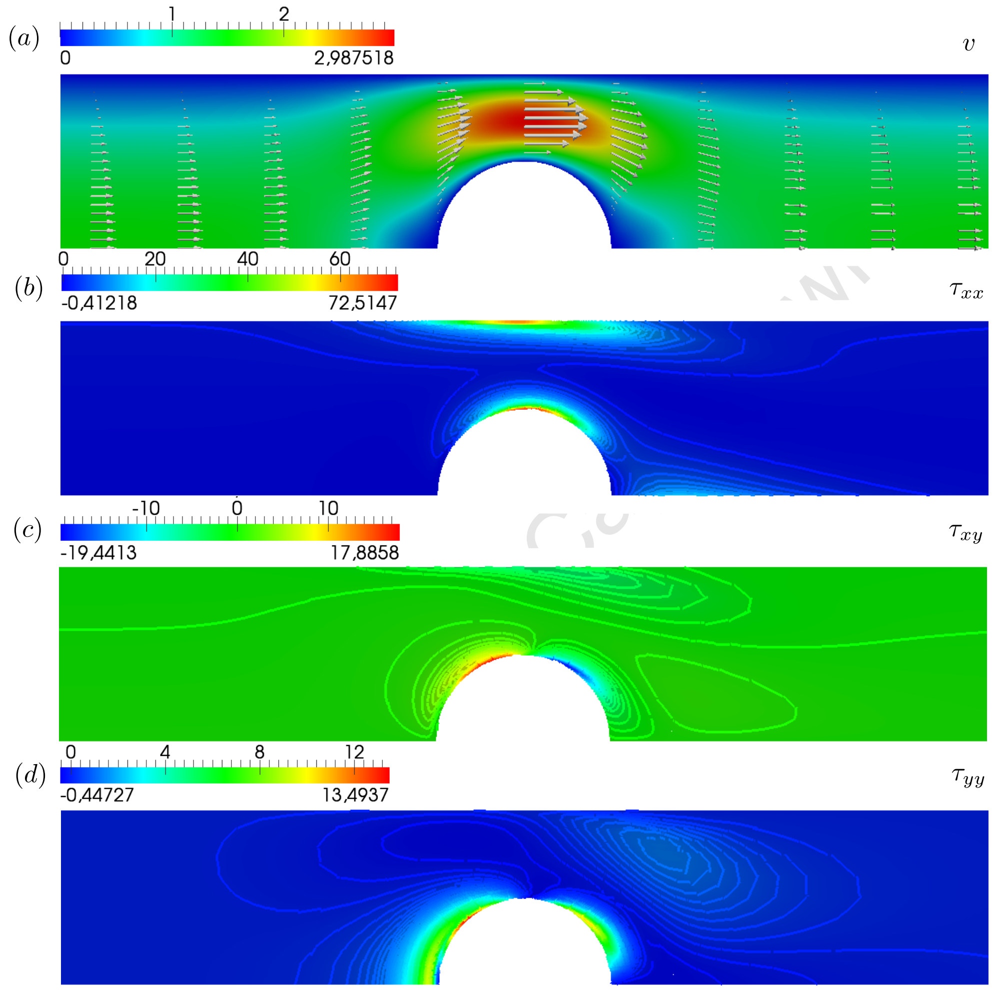

Figure 6.2. – Steady Oldroyd-B profiles for We=0.6 on finest mesh using Q_1^{disc} elements. (a) Velocity profiles. (b) τ_{xx} stress profiles. (c) τ_{xy} stress profiles. (d) τ_{yy} stress profiles.

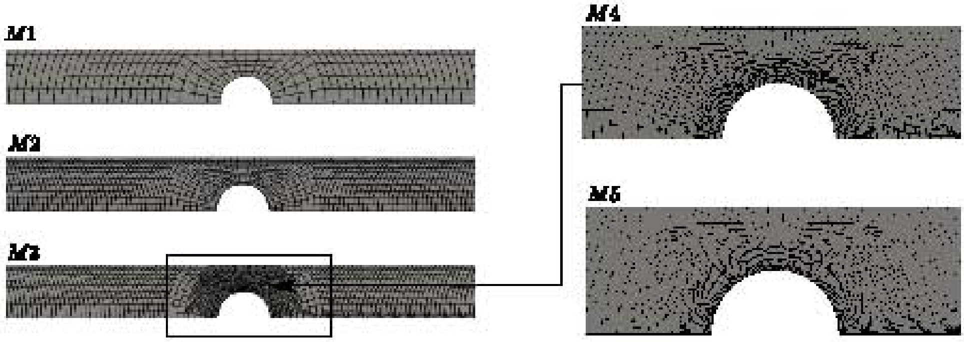

Figure 6.3. – Sequences of refined meshes M1-M5 for the problem of flow over a confined cylinder. M1 is the coarsest mesh while M5 is the most refined. Meshes M4 and M5 are only shown in the vicinity of the cylinder where additional refinement is performed.

flow, with the flow-rate in the constricted region being roughly twice that in the open channel. The polymeric extra-stress components τ_{xx}, τ_{xy} and τ_{yy} are shown in (b),(c) and (d) respectively. Qualitatively the profiles have very similar shape to those presented in [46] for the τ_{xx} field and in [27] for all extra-stress fields[2].

We proceed by describing physical interpretations for the solution profiles. Beginning with the τ_{xx} component of stress, which represents stretching of the dumbbells along the flow, in figure 6.2 (b) we observe regions of high stretching along the cylinder surface and the opposite channel wall. An additional feature, characteristic of viscoelastic flow, is a wake region of high τ_{xx} stress corresponding to stretching as the fluid accelerates away from the obstruction. The shear-stress τ_{xy} in (c) exhibits high values on the upstream half of the cylinder and along the opposite channel wall, where it is convected downstream. Lastly, the normal stress τ_{yy} in (d) shows high values on either side of the cylinder where compression and stretching in the vertical direction occurs. The τ_{yy} stress appears convected along the cylinder wall and additionally we observe a detached region near the stagnation point, in front of the cylinder.

Mesh Convergence Study

We proceed by performing a mesh-dependence study, which involves solving the problem under identical conditions on a sequence of refined meshes. It was observed in this study, and in the literature, that the τ_{xx} extra-stress component is particularly difficult to capture numerically, as it exhibits very sharp gradients along the cylinder and in its wake. We consider a sequence of 5 meshes, shown in figure 6.3, where the most refined meshes are only refined in these regions of high activity. The mesh convergence study will additionally provide a platform for comparison of the accuracy and validity for each

---

[2] In [27] results were presented for We = 1.0

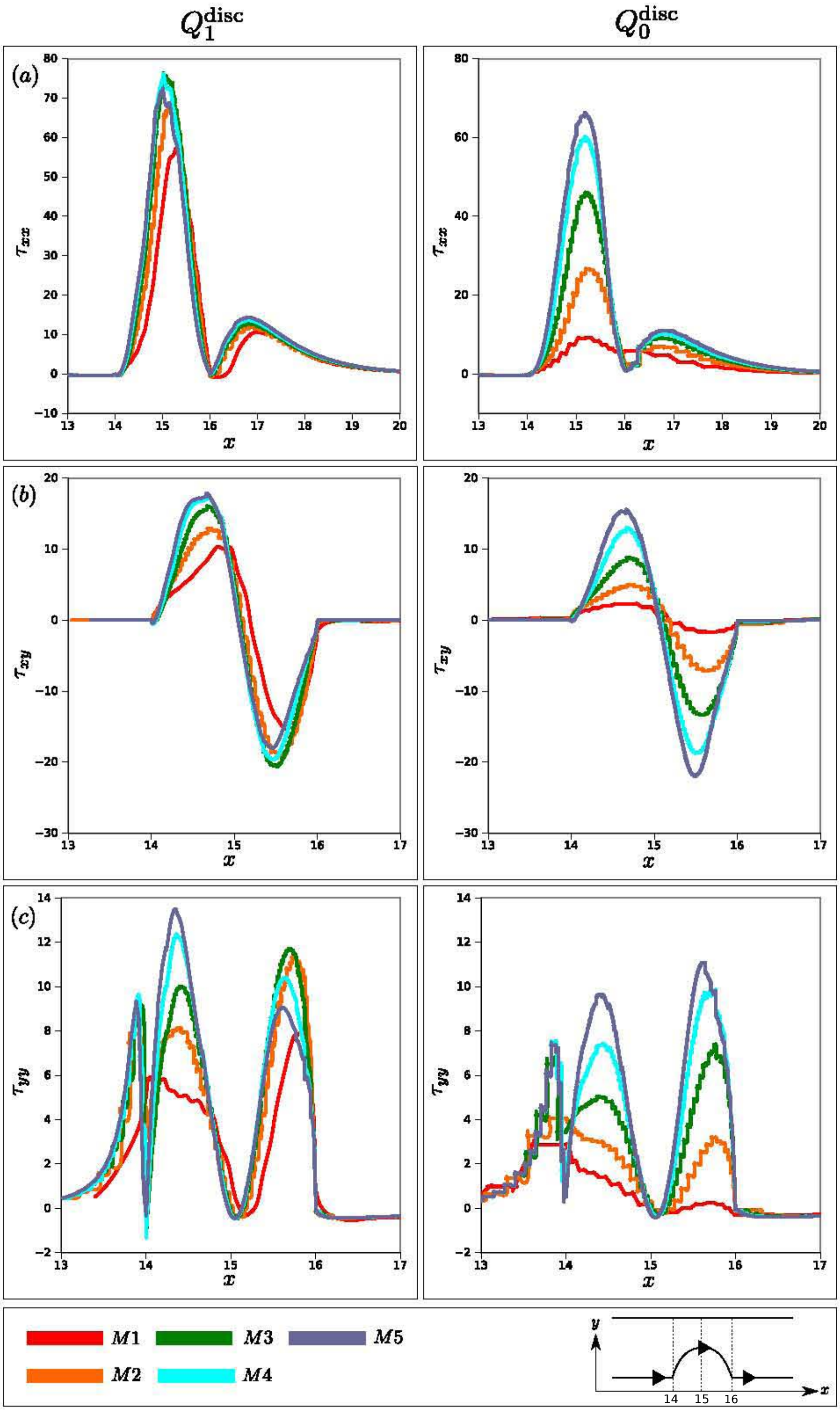

Figure 6.4. – Steady stress profiles along the symmetry axis and cylinder surface for Q_1^{disc} and Q_0^{disc} stress elements on five levels of refinement M1-M5. (a) Horizontal normal stress τ_{xx}. (b) Shear stress τ_{xy}. (c) Vertical normal stress τ_{yy}.

			DoFs			
Mesh	# Cells	h	Q_2- $\boldsymbol{u}$	$P_1^{\text{disc}} - p$	$Q_0^{\text{disc}} - \boldsymbol{\tau}$	$Q_1^{\text{disc}} - \boldsymbol{\tau}$
M1	502	0.2080	4446	1506	1506	6024
M2	2008	0.0983	16922	6024	6024	24096
M3	3040	0.0478	25950	9120	9120	36480
M4	5566	0.0235	47720	16698	16698	66792
M5	8989	0.0117	78184	26967	26967	107868

Table 6.1. – Mesh refinement details for flow over a cylinder. A summary of the number of degrees of freedom for each field, number of cells and characteristic scale h of each mesh.

extra-stress element choice. We $= 0.6$ is set constant for this study as it is near the limiting value for the Q_1^{disc} elements.

Due to the high computational cost, and slow convergence to equilibrium at higher We numbers, all the meshes used are relatively modest. Nonetheless, due to the manner of refinement we obtain very fine resolution in the region of interest. The details of these meshes is summarized in table 6.1, where h denotes the characteristic length of the smallest cell.

Concerning the physical fields, we observe that there is little variability of the velocity or pressure field beyond M3, due to the higher order interpolation of these fields. The largest variability occurs for the extra stress, particularly along the cylinder wall. In figure 6.4 we compare the convergence of the Q_0^{disc} and Q_1^{disc} elements by showing each component of extra stress for each level of refinement. Generally, the Q_1^{disc} elements show better convergence than the Q_0^{disc}elements, which appear to under-predict. This is particularly true for the τ_{xx} component shown in (a). This lower level of accuracy is expected for these lower order elements and is further amplified by comparing solutions on the domain boundary (this issue will be discussed further in section §7.3.1). The τ_{xx} profile correlates qualitatively with that presented in [31], showing the same shape with a slightly lower average value. In the literature, loss of convergence is typically observed in the wake region. It is thus promising that both Q_1^{disc} and Q_0^{disc} solutions appear near-converged in this region.

Typically, profiles for τ_{xx} are presented in the literature as a test of convergence. However, it is interesting to note that in (c) the τ_{yy} stress component exhibits a higher level of mesh sensitivity than the τ_{xx} component. The source of this sensitivity appears to be the difficulty in capturing the region of detached stress at the stagnation point using coarse meshes, and to an even larger degree with the lower-order Q_0^{disc} elements.

Dimensionless Drag

The non-dimensional drag

$$\begin{aligned} F_D &= \int_C \boldsymbol{e}_x \cdot \boldsymbol{\Sigma} \cdot \boldsymbol{n} \, \mathrm{d}\Gamma \\ &= \int_C \boldsymbol{e}_x \cdot \left(-p\boldsymbol{I} + \beta \left(\boldsymbol{\nabla u} + \boldsymbol{\nabla u}^T \right) + \boldsymbol{\tau} \right) \cdot \boldsymbol{n} \, \mathrm{d}\Gamma \end{aligned} \tag{6.1}$$

over the cylinder C at varying We number is a commonly used value to compare solutions obtained by different numerical schemes throughout the literature. In table 6.2, the drag F_D is tabulated for a range of We using both Q_0^{disc} and Q_1^{disc} elements alongside values obtained from numerous sources in the literature (as cited). The values presented were obtained on mesh M3 for consistency.

The drag values obtained using Q_1^{disc} elements very closely correlate to those presented in the literature, particularly in the lower We range. However the low limiting We number for these elements prevents us from observing the full profile, where a minimum drag is observed in the range We $\in (0.6, 0.8)$ after which the drag increases again. Although the drag values determined using Q_0^{disc} elements show a greater discrepancy to the literature, they do predict this parabolic trend correctly. The drag values are however significantly larger than in the literature, and more so for higher We. As the inaccuracy of solutions tends to increase with We, the solutions using Q_0^{disc} elements at We > 0.8 should be treated as merely preliminary. It has been noted in [56] that as the the drag is an integral quantity, it may average out any inaccuracies of the solution over the cylinder and so it should not be used as a sole indicator of the accuracy of a method.

In figure 6.5 we plot F_D vs. We for both element choices superimposed with the literature values from [31]. The parabolic shape may be clearly seen for the Q_0^{disc} elements, although the minimum appears at a lower We value than in [31]. The close correlation between solutions using Q_1^{disc} elements and the literature values is also observed.

We	M3 Q_0^{disc}	M3 Q_1^{disc}	Kim [56]	Fan [31]	Alves [1]	Hulsen [46]
0.1	129.183	130.558	130.359	130.36	130.355	130.363
0.2	125.116	126.629	126.622	126.62	126.632	126.626
0.3	121.655	123.089	123.188	123.19	123.210	123.193
0.4	119.26	120.393	120.589	120.59	120.596	120.596
0.5	117.983	118.656	118.824	118.83	118.832	118.836
0.6	117.819	117.752	117.774	117.77	117.786	117.792
0.7	118.746	117.596	117.315	117.32	117.328	117.340
0.8	120.790		117.351	117.36	117.370	117.373
0.9	124.108			117.79	117.87	117.787
1.0	128.836			118.49	118.59	118.501

Table 6.2. – Dimensionless drag F_D for Q_0^{disc} and Q_1^{disc} on M3 compared to literature values

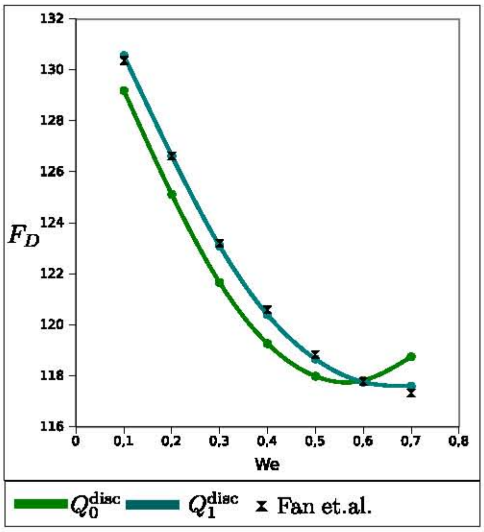

Figure 6.5. – Variation of F_D with We for both Q_0^{disc} and Q_1^{disc} elements as compared to values from Fan et.al. [31]

Dependence on We

The next aspect of this investigation is to observe the variation of the flow fields with increasing We number. The velocity field shows little noticeable difference with increasing We, with the most noticeable variation occurring in the wake of the cylinder. This is similarly observed in [56]. There is also little variation in the pressure field with increasing We as may be seen in figure 6.6 (a), where a plot of the variation of the pressure along the channel wall is shown. We observe that with increasing We the pressure drop over the obstructed region tends to decrease, while there is little difference in the inlet and outlet regions. Although these physical fields show little variation, the polymeric extra stress shows much larger variation. In figure 6.6 (b), a plot of the variation of the normal τ_{xx} stress along the cylinder and symmetry boundary is shown. We observe general growth both along the cylinder and in the wake. While on the cylinder surface the peak stress appears to asymptote with increasing We; no such behaviour is observed in the wake. It is in this wake that most authors (for example [56, 30]) observe the first loss of convergence at higher We numbers.

Stability

In section §6.1.3 we observed that although using Q_0^{disc} elements produced a very stable algorithm, which attained stable solutions at high We numbers, the solutions were slow to converge with mesh refinement. Using Q_1^{disc} elements on the other hand, produced a more accurate algorithm, but diverged for We ≥ 0.8. When using these elements, the algorithm first diverges in the region just behind the cylinder where τ_{xx} becomes

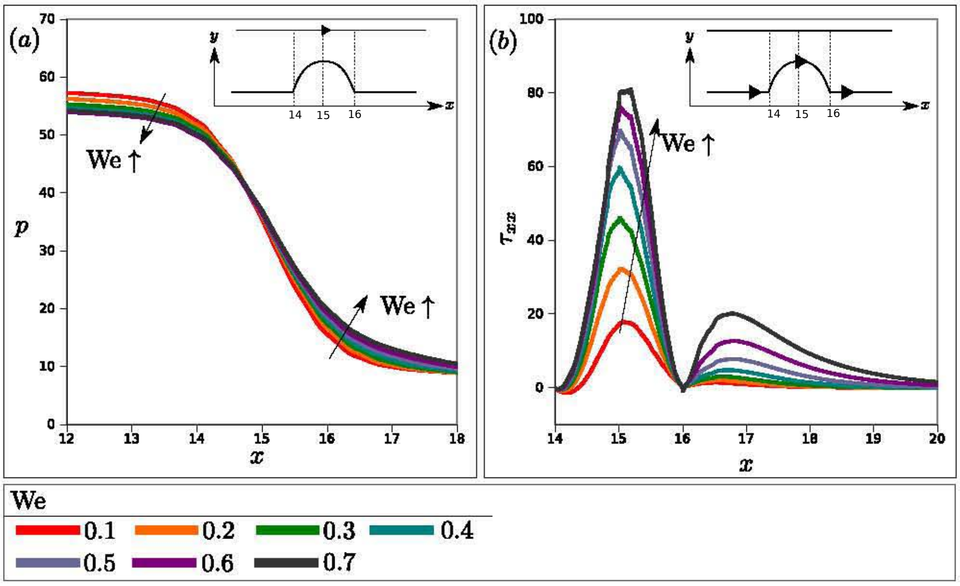

Figure 6.6. – Variation of flow field with increasing We. (a) Pressure profile along the channel wall. (b) Normal stress τ_{xx} along the symmetry axis and cylinder surface.

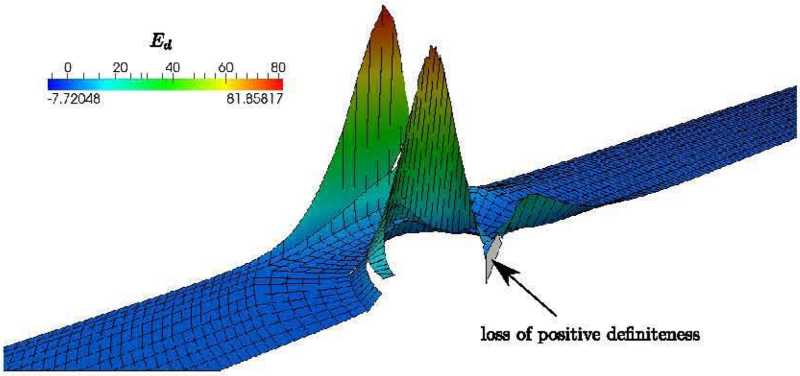

Figure 6.7. – Surface plot of E_2 vs. (x, y) just before the onset of instability at We $= 0.8$ using Q_1^{disc} elements on M2.

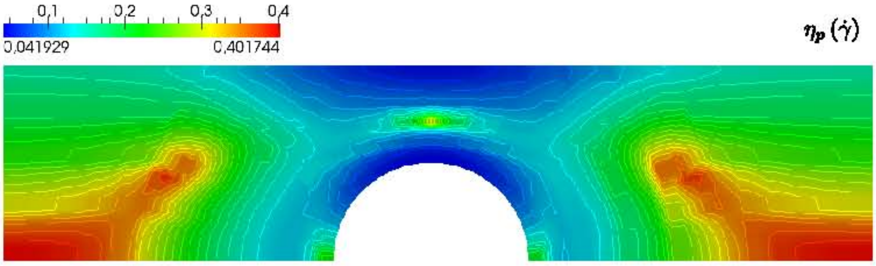

Figure 6.8. – Polymeric viscosity $\eta_p(\dot{\gamma})$ steady-state profile for We = 0.7 and $\alpha = 0.6$ using Q_1^{disc} elements on M3.

increasing negative. A surface plot of E_2 (defined in (2.38)) vs. (x, y) is shown in figure 6.7 when using Q_1^{disc} elements on M2 when We = 0.8. We observe that energy density is negative only in this same region (indicated in grey) that instability first arises. This region also corresponds to the area where the stress solution first loses monotonicity. Furthermore, it is in this region where a loss in positive-definiteness of $\boldsymbol{\sigma}$ (2.30) is first observed, which has been previously linked to the onset of instability. This negative energy density and loss of positive-definiteness is only a point-wise feature, with the cell averaged solution remaining monotone and $\boldsymbol{\sigma}$ remaining positive-definite. This suggests that the apparent stability of the Q_0^{disc} elements is strongly related to the preservation of monotonicity in the resulting solution.

6.1.4. Generalized Oldroyd-B Results

To this point, only the classical Oldroyd-B model has been considered, with good agreement to literature solutions shown. There is unfortunately very little literature to date on the generalized Oldroyd-B model with which to compare. Nonetheless, it may prove rewarding to explore what effects are produced by incorporating shear-thinning into the Oldroyd-B model. To do so, we consider only the case We = 0.7 using Q_1^{disc} stress elements on M3. We use the Carreau-Yasuda viscosity function (2.15), and set the fitted parameters of this function as in table 7.2, which will be used later in chapter 7 to simulate blood flow. The amount of shear-thinning present will be controlled by varying the parameter α, where $\alpha = 1$ corresponds to the classical non-shear-thinning model. [3].

In figure 6.8 we present the profile of the polymeric viscosity $\eta_p(\dot{\gamma})$ with $\alpha = 0.6$, which is just above the minimum allowed value of α. In the inlet and outlet channels, where the flow is fully developed, we observe a linear variation in η_p, with low viscosity along the wall and high values near the central symmetry axis. It is this variation which is responsible for the blunted velocity profile typically observed with shear-thinning fluids. In the constricted region, near the cylinder, the profile appears more complex, with regions of very low viscosity near the top of the cylinder and the opposite channel wall. In addition,

---

[3] Since $\alpha > \beta$ and $\beta = 0.59$ we treat the range $0.6 < \alpha < 1.0$ using increments of $\Delta\alpha = 0.1$

regions of higher viscosity are present at the stagnation point of the cylinder and also just behind it. Since $(\alpha - \beta) \sim 0$ the amount of variation of the polymeric viscosity is high. The profile is furthermore symmetric, which indicates that viscoelasticity has little role in this range of parameters and that shear-thinning has a predominant influence.

To examine this notion further, we show in figure 6.9 the variation with α of the two normal stress components τ_{xx} in (a) and τ_{yy} in (b) along the cylinder surface and symmetry boundary. We observe diminishing stress with increasing α in both the τ_{xx} and τ_{yy} stress components. Nearly an order of magnitude difference in stress values is observed between the purely viscoelastic solution $\alpha = 1$ and when $\alpha = 0.6$. This further reinforces the notion that shear-thinning is by far a stronger property than viscoelasticity and appears to diminish viscoelastic influence with increasing presence.

Following the results above, which show decreasing extra stress with increasing shear-thinning, we expect that there will be a similar dependence on the drag over the cylinder F_D. In [66] a power-law non-Newtonian fluid was treated in an identical geometry. In that study, a power dependence was observed between the drag and the power-law parameter n. This is equivalent to an inversely proportional relationship between F_D and α. This dependence is physically reasonable, as the low regions of viscosity occur precisely over the cylinder surface where the shear-rate is highest - resulting in a lower drag. We expected this result to carry through to the generalized Oldroyd-B model and investigate this by plotting $\ln(F_D)$ vs. $\ln(\alpha)$ in figure 6.10. A near-linear relationship is evident, which reinforces the power-law type dependence on drag to the amount of shear-thinning. Although the number of data points are few and the computational mesh used is relatively coarse, the fitted linear function has a goodness of fit value $R^2 = 0.97$, which is promisingly high. An investigation on the dependence of drag on the other shear-thinning parameters may form part of future work.

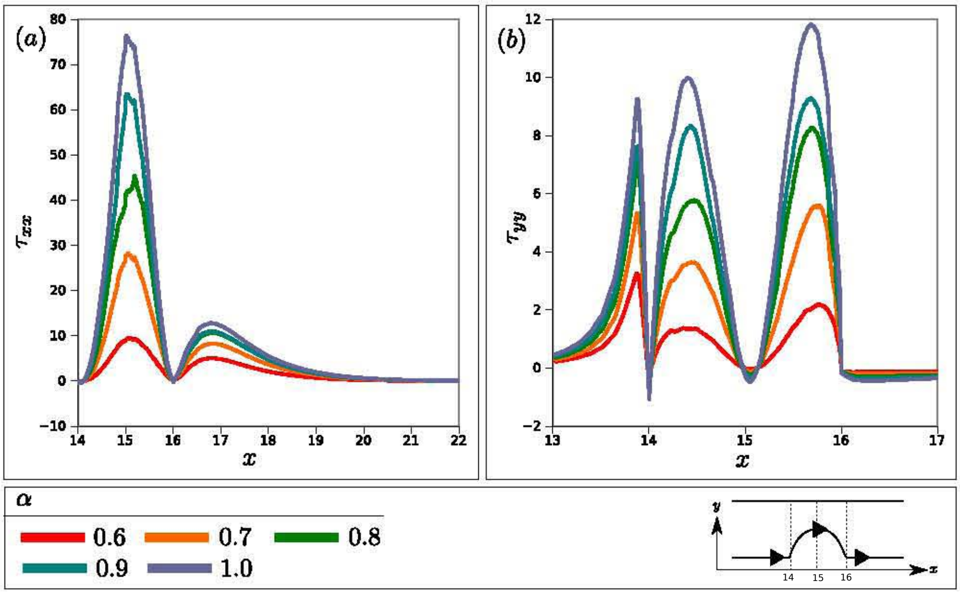

Figure 6.9. – Variation of extra stress with α along the symmetry boundary and cylinder surface. (a) Horizontal normal stress τ_{xx} (b) Vertical normal stress τ_{yy}.

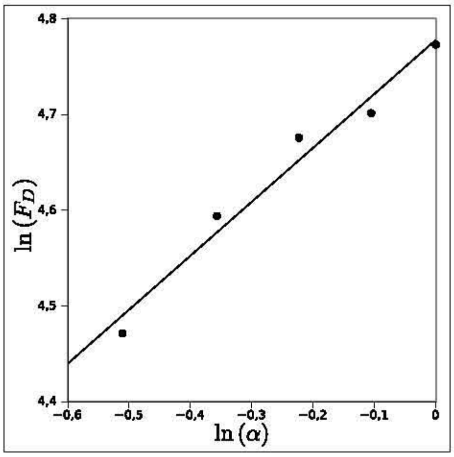

Figure 6.10. – Variation of drag F_D with increasing shear-thinning α. A log-log plot of F_D vs. α exhibiting a linear relationship as indicated by superimposed trend-line.

6.2. Driven Cavity Problem

6.2.1. Introduction

Many of the popular benchmark tests for viscoelastic flows are steady problems, with little numerical work available on time-dependent flows. Frequently the “start-up” variants of these steady problems are used for testing time-dependent methods. In this section we consider the 2D start-up driven cavity problem, which although not as popular a benchmark has received some attention, particularly for Newtonian fluids. This is mostly due to the simplicity of the geometry and the yet complex resulting flow. Additionally, there are numerous industrial applications for this problem such as mixing and coating, where a thorough understanding and prediction of rheological flows is important [72]. The problem may be defined as a fluid confined in a square cavity, where along one side a constant tangential velocity is prescribed, while no-slip conditions are set on all other boundaries.

There are two main challenges when solving this problem: the first is dealing with the singularity in boundary conditions at both top corners where $\boldsymbol{\nabla u}$ is singular. The second problem concerns the emergence of purely elastic instability at arbitrarily low Re numbers. The elastic instabilities were observed experimentally by Pakdel *et.al.* [71] where digital particle image velocimetry (DVIV) was used to show and identify the instability for an ideal Boger fluid.

Computationally, in [39] an hp-FE method was used to simulate a FENE-CR viscoelastic fluid within a driven cavity. In that study, the problem was modified to alleviate the geometric singularity by allowing some leakage of the fluid near the lid corners. Despite these modifications, convergent results were only obtained for $\mathrm{We} \leq 0.2$. The problem is clearly a stringent test and has more recently been tackled within a log-conformation tensor formulation using finite differences in [33] and finite elements in [73]. In both these works, a quartic start-up driving velocity was used to avoid the singularities at the corners and solutions were obtained for high Weissenberg numbers $\mathrm{We} \leq 3$. In [33] oscillations in the energy were observed at higher We, while in [73] stable solutions and monotone energy evolution was achieved using their numerical scheme. In the work of Boyaval [14], the same problem using the same boundary conditions and modifications was treated using low order finite elements, in line with their previous work in [15]. The focus of this study was to investigate the convergence of a defined free energy (2.35) within the range $0.8 \leq \mathrm{We} \leq 2.0$.

In this section we will follow a similar approach as [14], using the same driving velocity initially for the Oldroyd-B model, and then present some extensions by considering the generalized model. This will also provide an opportunity to investigate the numerical consequences of the theoretical results discussed in section §2.8.

6.2.2. Problem Definition

We define the geometry, as shown in figure 6.11, as a square domain of unit length $(x, y) \in [0, 1]^2$. The top edge ($y = 1$) acts as the driven lid by prescribing the time dependent velocity

$$\boldsymbol{u} = \begin{bmatrix} u(x,t) \\ 0 \end{bmatrix} \quad \text{where } u(x,t) = 8x^2 (x-1)^2 \{1 + \tanh(8t - 4)\} \tag{6.2}$$

along this side. No-slip boundary conditions are applied on all other boundaries. We once again approximate creeping flow by setting $\mathrm{Re} = 0.01$ to make inertial effects negligible. Keeping in line with [14, 33], we set equal quantities of polymeric and solvent viscosity, i.e. $\beta = 0.5$. Using zero velocity, pressure and stress profiles as initial conditions, transient solutions are obtained by time-stepping using $\Delta t = 0.01$ until the solutions have converged for lower We numbers, and until $t = 20$ for higher We.

Solutions will be obtained on a sequence of three meshes M1-M3, each defined by subdividing the unit square into 2^n equal sized squares. Both Q_0^{disc} and Q_1^{disc} elements were considered for the stress. The details of these meshes are presented in table 6.3, where h again represents the characteristic length of the cells.

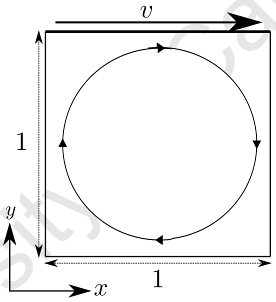

Figure 6.11. – Computational geometry for the driven cavity problem.

			DoFs			
Mesh	# Cells	h	Q_2- $\boldsymbol{u}$	$P_1^{\text{disc}} - p$	$Q_0^{\text{disc}} - \boldsymbol{\tau}$	$Q_1^{\text{disc}} - \boldsymbol{\tau}$
M1	256	0.0625	2178	768	768	3072
M2	1024	0.0312	8450	3072	3072	12288
M3	4096	0.0156	33282	12288	12288	49152

Table 6.3. – Mesh refinement details for driven cavity flow. Summary of the number of degrees of freedom for each field, number of cells and characteristic scale h for each mesh.

6.2.3. Oldroyd-B Results

Low We

Initially a low range of We numbers ($0.1 \leq \text{We} \leq 0.4$) was considered and the time-dependent simulations were allowed to continue until all the fields had sufficiently converged[4]. The time required to achieve this convergence increased with both We number and mesh refinement. The solutions obtained using Q_1^{disc} elements diverged (blew up) at $\text{We} = 0.4$ on M2 and M3, while solutions using Q_0^{disc} elements showed no such trends, even at much higher We values. In figure 6.12 we present the converged steady profiles using Q_0^{disc} elements on M3 at $\text{We} = 0.4$. In (a) we plot the velocity magnitude superimposed with a sample of streamlines of the flow. A central vortex of clockwise flow is present with slight left-right asymmetry, characteristic of a viscoelastic fluid. Additionally, there are two faint secondary vortices in the bottom corners, which are only resolved on the two finer meshes M2 and M3.

In (b), the normal τ_{xx} stress profile is shown. A region of high stress is present at top boundary, where stretching occurs along the driven edge and some convection is observed along the primary vortex. Even at this moderate We number the stress gradient is very sharp near the driven boundary. In (c), the shear stress τ_{xy} profile is shown exhibiting high values near both top corners where the flow changes direction. This is similar to the τ_{yy} profile in (d), where compression and stretching in the vertical direction occurs as the fluid is pushed towards the lid on the left and then away from the lid on the right.

We examine the convergence and stability in this range of We by plotting the energy E_2 as a function of time in figure 6.13, when using both (a) Q_1^{disc} stress elements and (b) Q_0^{disc} stress elements. The energy is plotted for all solutions on all three meshes M1-M3 using different line styles as indicated in the key, with different colours used to distinguish between different We numbers. It is clear from these plots that for $\text{We} \leq 0.3$, using both Q_1^{disc} and Q_0^{disc} elements produces identical profiles, each plateauing to a converged steady-state. The Q_0^{disc} solutions are slower to converge with refinement and with time than the corresponding Q_1^{disc} solutions, although the final energy levels are the same. For $\text{We} = 0.4$, the Q_1^{disc} solutions diverge at refinement higher than M2, as can be seen by the spike in the energy profile. The Q_0^{disc} solutions on the other hand, are stable but exhibit large mesh sensitivity. This is most prevalent in the start-up phase, with the converged steady solutions (outside of the time scale in (b)) showing good agreement between refinement levels.

---

[4] As before, the solutions were considered as converged once the L_2 norm of the difference in all fields fell beneath $10^{-6}\Delta t$.

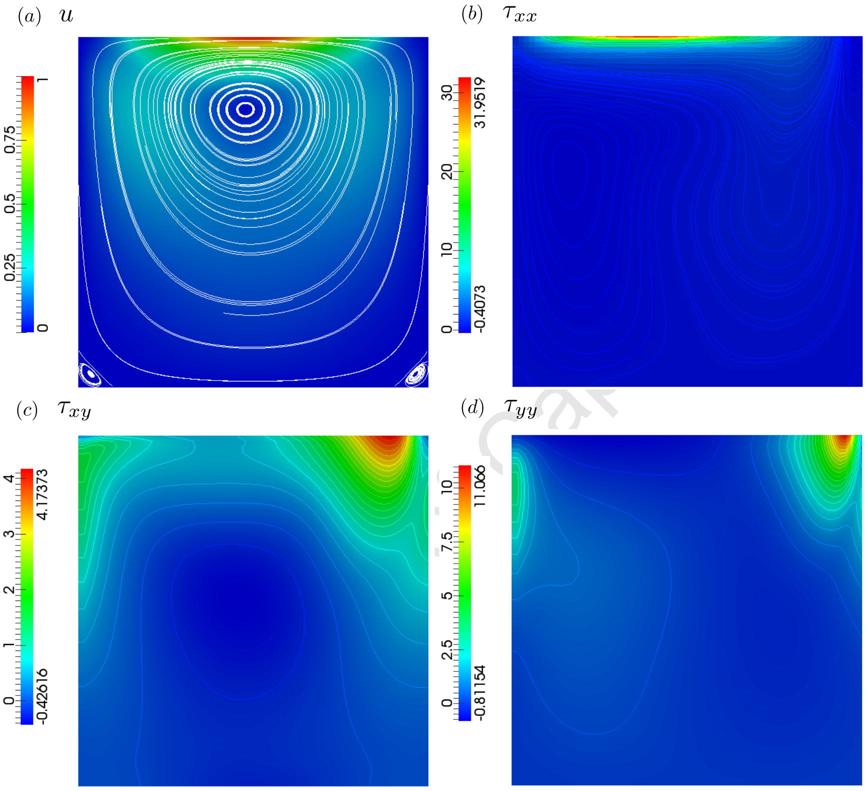

Figure 6.12. – Steady-state solution profiles for Oldroyd-B fluid at We = 0.4 on M3 using Q_0^{disc} stress elements. (a) Velocity field with superimposed streamlines. (b) Horizontal normal stress τ_{xx} . (c) Shear stress τ_{xy}. (d) Vertical normal stress τ_{yy}.

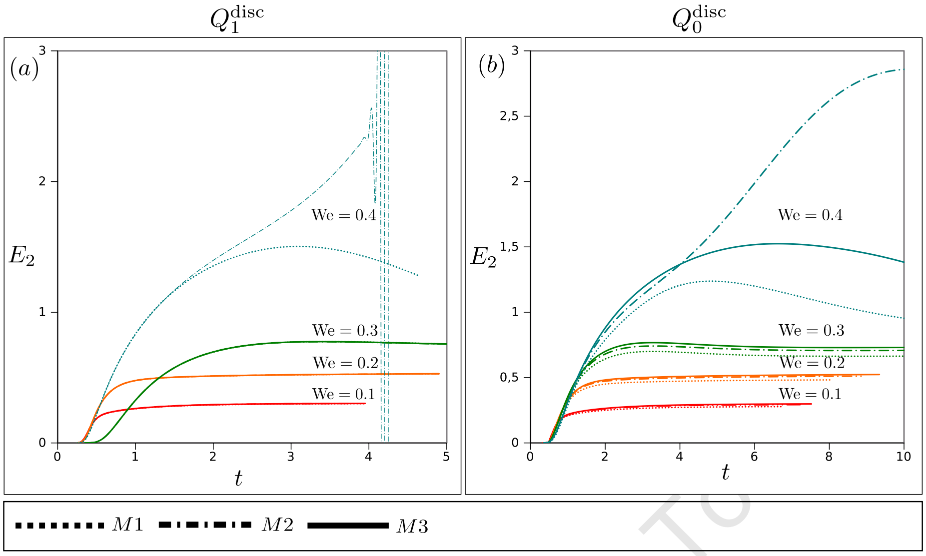

Figure 6.13. – Evolution of the energy E_2 with time for We $= 0.1, 0.2, 0.3$ and 0.4 and on three levels of refinement M1,M2 and M3 using (a) Q_1^{disc} stress elements and (b) Q_0^{disc} stress elements.

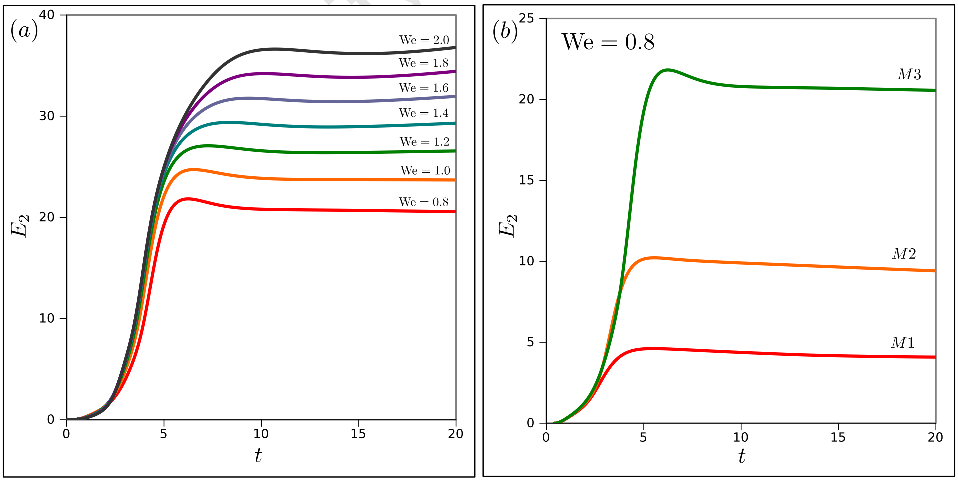

Figure 6.14. – Evolution of the energy E_2 with time at high We numbers using Q_0^{disc} stress elements. (a) Energy evolution on M3 for $0.8 \leq$ We ≤ 2.0. (b) Energy evolution at We $= 0.8$ on three levels of refinement M1,M2 and M3

High We

We turn our attention now to a higher range of We numbers, namely $0.8 \leq \mathrm{We} \leq 2.0$, following the work presented in [14]. The start-up problem is solved for $\mathrm{We} = [0.8, 1.0, 1.2, 1.4, 1.6, 1.8, 2.0]$, allowing the simulations to run until a final time $T_{\mathrm{fin}} = 20$ by which time the solutions are near-converged. Since when using Q_1^{disc} elements the solutions do not converge past $\mathrm{We} = 0.4$, we use only Q_0^{disc} elements in this section. In figure 6.14 (a) a plot of the evolution of the energy E_2 with respect to time on M3 for each We number is presented. We observe that the steady energy grows with increasing We number and the relaxation time to convergence similarly increases, as expected. Furthermore, the conformation tensor $\boldsymbol{\sigma}$ never loses positive-definiteness throughout the simulation.

The accuracy of these solutions is, however, somewhat questionable with additional refinement required to produce converged solutions. This may be observed in figure 6.14 (b), where a plot of E_2 vs. time for $\mathrm{We} = 0.8$ on each mesh M1-M3 is shown. The solutions are clearly very mesh sensitive and the trend with refinement appears divergent. This trend is further amplified at higher We. Nonetheless, within each refinement level the solutions are stable. This brings into question the distinction between “energy-stability” and “accuracy” in the context of the high Weissenberg number problem. These results correspond with the findings in [14], although the increased complexity and modifications to our algorithm ensure that positive-definiteness is preserved for higher We, compared to the limiting We=1.0 observed in that study. Irrespective of this, from both this study and that in [14], it appears that a combination of DG-upwinding and piecewise constant elements for stress produce a very stable method for simulating viscoelastic flow.

6.2.4. Generalized Oldroyd-B Results

In this section we focus on the generalized Oldroyd-B model for the driven cavity problem, and in particular the numerical consequences of the theoretical results discussed in section §2.8. Transient solutions were obtained using Q_0^{disc} stress elements on three levels of refinement M1-M3 for the higher range of We numbers, i.e. $\mathrm{We} \in [0.8, 2.0]$. Shear-thinning was incorporated using the Carreau-Yasuda viscosity function, using the same parameters as in table 7.2 with the “amount” of shear-thinning controlled by the parameter α. Simulations were carried out for $\alpha \in [0.5, 1.0]$, where $\alpha = 1$ corresponds to the classical Oldroyd-B model.

We seek to explore the behaviour of ζ (2.37) by obtaining a numerical estimate of this quantity. This is done by first obtaining $\ln \mu_p(\dot{\gamma}^n)$ at quadrature points at each time n, and then projecting onto the space of Q_1^{disc} finite element functions $\mathcal{S}$ to obtain a numerical approximation to this variable λ^n. This may be expressed in variational formulation

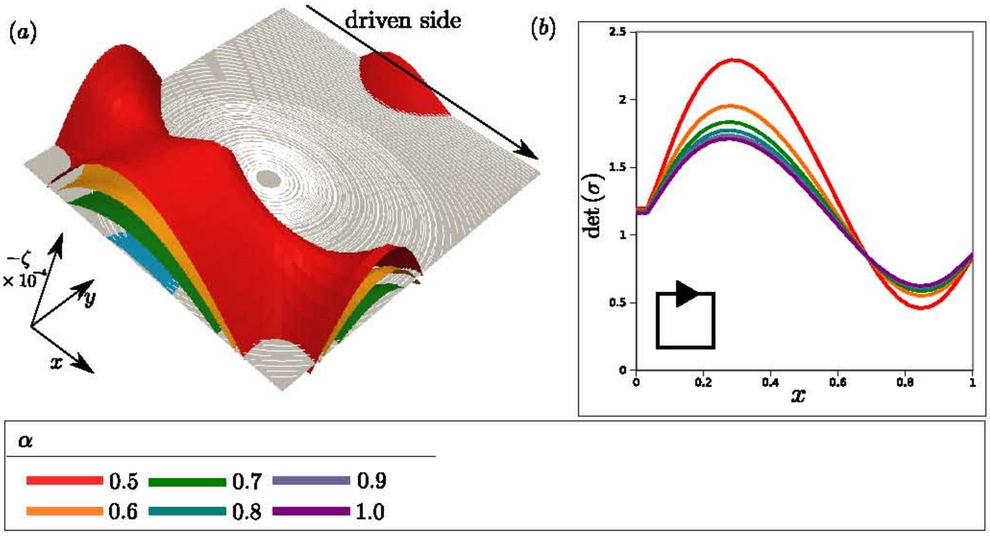

Figure 6.15. – Variation of ζ and $\det(\boldsymbol{\sigma})$ with α for the GOB model at $t = 0.6$ and We $= 0.8$ on M3 using Q_0^{disc}elements. (a) Surface plot of $-\zeta$ vs. (x, y). (b) Plot of $\det(\boldsymbol{\sigma})$ along the driven edge.

as: find $\lambda^n \in \mathcal{S}$ such that

$$\int_\Omega \lambda^n \nu \,\mathrm{d}\Omega = \int_\Omega \ln \mu_p\left(\dot{\gamma}^n\right) \nu \,\mathrm{d}\Omega \;\; \forall \nu \in \mathcal{S}. \tag{6.3}$$

A numerical estimate for ζ at a time n is then obtained by approximating the material derivative in (2.37) using a backward Euler finite difference scheme and again projecting onto the space of Q_1^{disc} finite element functions $\mathcal{S}$, expressed weakly as: find $\zeta^n \in \mathcal{S}$ such that

$$\int_\Omega \zeta^n \nu \,\mathrm{d}\Omega = \int_\Omega \left\{ \frac{1}{\mathrm{We}} + \frac{\lambda^n - \lambda^{n-1}}{\Delta t} + \boldsymbol{u}^n \cdot \boldsymbol{\nabla} \lambda^n \right\} \nu \,\mathrm{d}\Omega \;\; \forall \nu \in \mathcal{S}. \tag{6.4}$$

Of particular interest is to observe the consequences that arise to the positive-definiteness of the conformation tensor $\boldsymbol{\sigma}$ with the emergence of negative ζ values. In section §2.8.1, two results were obtained for the GOB model. Firstly, if $\zeta(t) > 0 \; \forall t \in \mathbb{R}^+$ and $\boldsymbol{\sigma}(t = 0)$ is positive-definite, then $\boldsymbol{\sigma}(t)$ will remain positive-definite for all time, i.e. $\det(\boldsymbol{\sigma}) > 0$ and $\sigma_{xx} > 0 \; \forall t \in \mathbb{R}^+$, $\boldsymbol{x} \in \Omega$. The second result was a stricter form of the first, where if in addition $\zeta(t)$ is small and $\det(\boldsymbol{\sigma}(t = 0)) \geq 1$, then in addition it holds that $\det(\boldsymbol{\sigma}(t)) \geq 1 \; \forall t \in \mathbb{R}^+$, $\boldsymbol{x} \in \Omega$. Both these results were used to define corresponding free energies and ensure their dissipation and hence ensuring the stability of solutions.

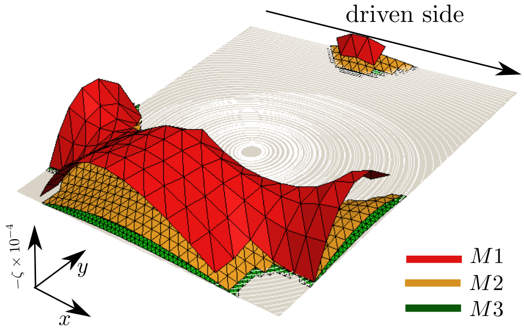

Figure 6.16. – A surface plot of $-\zeta$ vs. (x, y) to illustrate the variation of ζ with mesh refinement for the GOB model at $t = 0.6$, $\mathrm{We} = 0.8$ and $\alpha = 0.5$ using Q_0^{disc} elements.

It was observed that during the simulations at $t = 0.6$, near the middle of the start-up phase, the condition $\zeta > 0$ is most violated for all values of We and α. In figure 6.15 a surface plot of $-\zeta$ vs. (x, y) is presented in (a) at $t = 0.6$ and $\mathrm{We} = 0.8$ for varying α. It can be seen that ζ is most negative near the bottom of the cavity and along the driving side. Furthermore, ζ is most negative for $\alpha = 0.5$, with no regions of negative ζ experienced for $\alpha > 0.8$. However despite these negative ζ values, no loss of positive-definiteness of $\boldsymbol{\sigma}$ is observed. The lowest values of $\det(\boldsymbol{\sigma})$ are present along the driven side, which is plotted in figure 6.15 (b). The condition $\det(\boldsymbol{\sigma}) \geq 1$ is violated on the right half of this edge and increasingly so at lower α values. This is not a consequence of the GOB model as $\det(\boldsymbol{\sigma}) < 1$ at $\alpha = 1$, which is the limit of the classical Oldroyd-B model. It should also be noted that the magnitude of these $-\zeta$ values is very small ($\sim 10^{-4}$) and hence conclusions from these results should be treated with care.

As the ζ values obtained above are themselves numerical estimates, it is necessary to perform a mesh sensitivity study to measure the extent to which these values depend on the discretization. Such a result can be seen in figure 6.16, where a surface plot of $-\zeta$ vs. (x, y) at $\mathrm{We} = 0.8$, $\alpha = 0.5$ and $t = 0.6$ is presented on three levels of refinement M1-M3. The regions exhibiting negative ζ appear to diminish with refinement, as does the magnitude of $-\zeta$ in these regions. The general shape of these plotted surfaces, however, appear similar. From this result it is clear that the estimates for ζ are sensitive to refinement, with additional numerical work required to fully ascertain the extent and limit of this sensitivity. Such a study however falls outside the scope of this work.

The final aspect which we will consider is the variation of the $-\zeta$ values with increasing We number. To do so, we consider the plot of ζ along the line $y = 0.25$ shown in figure 6.17, at $t = 0.6$ and $\alpha = 0.5$ for varying We numbers on M3. It is along this line, as can be seen in figure 6.15, that ζ is most negative. The profile of ζ shows little variation in shape with increasing We, although a generally decreasing average value is observed. This average also appears to converge as $\mathrm{We} \to 2.0$, although the small magnitude of the scale $\sim 10^{-5}$ should be considered before any significant trends may be extracted.

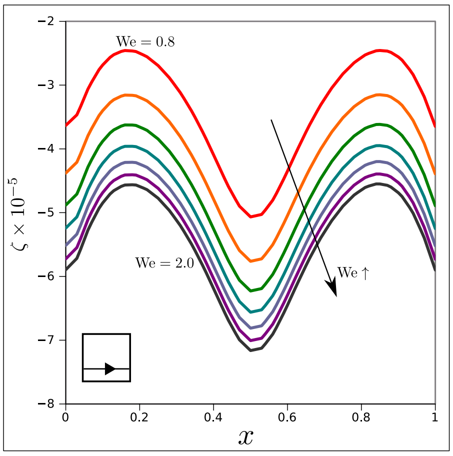

Figure 6.17. – Plot of ζ along the line $y = 0.25$ at $t = 0.6$, $\alpha = 0.5$ with varying We numbers using Q_0^{disc} elements on M3.

In summary, within the range of considered parameters and refinement levels: the algorithm using Q_0^{disc} produced stable results for the GOB driven cavity problem. Although the numerical quantity ζ exhibits regions of negative value, this did not lead to a loss in positive-definiteness of the conformation tensor $\boldsymbol{\sigma}$. Furthermore, although the condition $\det(\boldsymbol{\sigma}) \geq 1$ is violated during the simulation, the solutions obtained did not diverge. This is as expected following the discussion in section §2.8.1. This may be seen as a preliminary study, with future work perhaps focusing on the dependence on the other shear-thinning parameters in the Carreau-Yasuda model. Further numerical studies on the influence of the time step may be fruitful, particularly when considering more extreme flow regimes.

7. Pulsatile Blood Flow through a Stenotic Arteriole

7.1. Introduction

The importance of blood throughout the human body has led to its study for thousands of years: from the early measurements of the pulse by ancient Chinese practitioners, to the anatomical studies of the arteries by Aristotle, and later still to the study of the heart and circulatory system by Leonardo da Vinci. In modern times the availability of new technologies for measurement and experiment has led to a greater understanding of the dynamics of the vascular system, and in particular the pulsatile dynamics of pressure and flow [60]. Numerical simulation of blood flow in conjunction with physiological experiment is essential to a further understanding of the underlying fundamental properties of blood. Numerical studies allow for investigations of blood flow in non-trivial geometries as well as in diseased systems. Further applications include design-by-computation, such as in [8] where an assisted circulation medical device was considered. Such numerical methods require models which accurately describe the characteristics of blood, as well as appropriate geometries and flow conditions as found in the vascular system.

One application of the generalized Oldroyd-B model is simulating blood flow in small arteries and arterioles, where the shear-thinning and viscoelastic nature of blood is significant while the continuum approximation for blood is still appropriate [91, 75, 47, 65, 12]. An important physiological scenario in blood flow, where non-Newtonian and viscoelastic properties are significant, is flow through an obstructed stenosed channel. The pulsatile nature of blood circulation makes the simulation of this problem naturally unsteady and thus a good example to illustrate the applicability of our numerical method. Additionally, physiologically realistic parameters can be set for the model which will illustrate the functionality of our numerical method within a *useful* range of parameters and allow for comparison to other numerical studies [32, 48].

7.1.1. Characteristics of Blood

Blood is a complex suspension of red blood cells (erythrocytes), white blood cells (leukocytes) and platelets suspended in a plasma of organic molecules and electrolytes, consisting mostly of water [82]. Although the plasma is Newtonian, the presence of the suspended particles introduces certain non-Newtonian properties. The red blood cells, being in majority, are mostly responsible for the mechanical properties of blood. They are effectively elastic membranes filled with a saturated solution of hemoglobin which can store and release elastic energy. Furthermore, they tend to aggregate and form long chains called *rouleaux.* This occurs when the shear-rate is low enough compared to the characteristic time of formation of these structures (less than $10s^{-1}$). The presence of these *rouleaux* increases the viscosity of the blood at low shear-rates, while at higher shear-rates they tend to break up and align with the flow, decreasing the viscosity. This introduces a shear-thinning character to blood which was first discovered by Chien *et.al.* [21].

In addition, the elasticity of the formed *rouleaux* and the individual red blood cells introduces viscoelastic properties, first recognized by Thurston [86]. The magnitude of these viscoelastic properties is small and most prevalent in smaller arteries and regions of recirculation, where the aggregated red blood cell formations are more stable. Other more complex properties, such as thixotropy, platelet activation and clotting have also been observed (see [82]).

7.1.2. Models for Blood

In larger arteries, blood has been traditionally modelled as an incompressible Newtonian fluid and has been experimentally validated in these flow regimes by [93], amongst others. Although this assumption provides sufficient accuracy in most of the vascular system, much attention has nonetheless been placed on a non-Newtonian description of blood. To this end, generalized Newtonian models where the viscosity is treated as a function of the shear-rate have dominated the literature. In [77], the viscosity function (2.32) was used in conjunction with the Navier-Stokes equations to describe the shear-thinning behavior of blood. Similarly in [12] and [59] the Cross model was applied to similar effect, while in [87] the Herschel-Buckley model was used. Other generalizations have been based on the Casson and Carreau-Yasuda viscosity functions in [82, 65].

In more recent works, viscoelasticity has also been incorporated into models for blood. In [91], an empirically fitted viscosity function was used within a generalized Oldroyd-B model and was experimentally validated by an *in vitro* experiment of porcine blood through a glass tube. The numerical predictions with this model showed far better correlation with the experimental results than predictions made with a Newtonian model. Due to this good correlation, many authors have chosen to use this model for numerical work [75, 47, 76]. Alternatively, in [2] a different viscoelastic model based on a thermodynamic framework was developed and showed good agreement with the experimental work in [86]. In [84], a FENE viscoelastic model was used which naturally exhibits shear-thinning behavior. An extension to the generalized Oldroyd-B model which incorporates thixotropy, was presented in [32]. In this work an additional reaction-diffusion equation was coupled to the system, which represented the formation and destruction of the *rouleaux* and influenced the polymeric viscosity.

7.1.3. Arterial Stenosis

Atherosclerosis is a common condition where stenotic obstructions in arteries form from fat deposits and plaque build-up on blood vessel walls (see [93]), as represented in figure 7.1. Understanding and being able to predict the flow properties in these constricted channels is important to understanding the formation and further evolution of the plaque deposits and is thus very medically relevant. Although much work on this topic is concerned with larger arteries, where a Newtonian description of blood is appropriate, the inclusion of additional material properties is necessary for a fuller description [9]. For this reason, flow through a stenotic channel has received much attention in the literature from experimental and physiological perspectives (see [93, 92]) as well as in numerical and modeling studies (see [12]). The vascular walls will be treated as rigid walls in this work although material specific treatment of the vascular wall and plaque deposits should be considered, as stated in the review [9]. This has been done by a deformable, viscoelastic treatment of the arterial wall in previous numerical studies where a simpler description for blood was used. Such treatment however falls outside the scope of this work and will not be considered further.

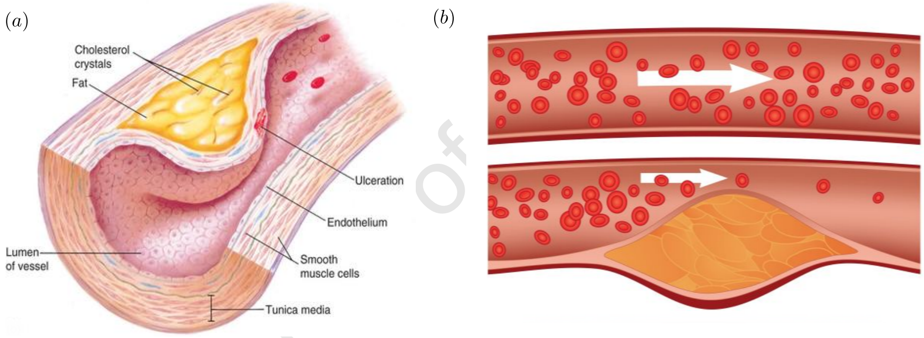

Figure 7.1. – Representation of atherosclerosis obtained from (a) `http://humanphysiology2011.wikispaces.com/06.+Cardiology` and (b) `http://www.omnimedicalsearch.com/conditions-diseases/angina-introduction.htm`

7.2. Problem Definition

The purpose of this section is to simulate, under physiologically realistic parameters and conditions, steady and pulsatile blood flow through a stenotic channel in 2D using the generalized Oldroyd-B model with the Carreau-Yasuda viscosity function. This will provide an example of applicability of the numerical methods in this work to a realistic setting. Additionally, this will illustrate the influence of viscoelasticity and shear-thinning, individually and in conjunction. This will be done by treating the Newtonian, generalized Newtonian, Oldroyd-B and generalized Oldroyd-B models simultaneously and thus allow for comparisons between them. Despite simplifications made in the geometry and the definition of the pulsatile flow, qualitative features and interesting model behaviour can be extracted.

7.2.1. Geometry, Boundary Conditions and Model Parameters

The geometry of the problem is a rigid symmetrically stenosed channel as shown in figure 7.2, where the top boundary is defined by the curve

$$f(x) = \begin{cases} 1 - \frac{1}{2}\cos^2(\frac{\pi}{4}(x - 7.5)) & 5.5 < x < 9.5 \\ 1 & \text{elsewhere} \end{cases} . \tag{7.1}$$

This corresponds to a rectangular channel with blockage ratio of 1/2. The boundaries are assumed to be rigid, with pulsatile inflow boundary conditions set as

$$\boldsymbol{u}(y,t) = \begin{bmatrix} u_1(y)(1 + 0.8\sin(\omega' t)) \\ 0 \end{bmatrix} \tag{7.2}$$

where $u_1(y)$ is the horizontal component of steady Poiseuille flow for the GOB model (see section §A.4). This velocity and corresponding polymeric stress is prescribed along the inflow boundary (A). A sufficiently long inlet is then chosen to minimize the effects of this approximation in inflow boundary conditions. Additionally only half the channel is modelled, assuming a symmetry boundary $\frac{\partial \boldsymbol{u}}{\partial y}|_{\partial\Omega_B} = \frac{\partial \boldsymbol{\tau}}{\partial y}|_{\partial\Omega_B} = 0$ and $\boldsymbol{u} \cdot \boldsymbol{n}|_{\partial\Omega_B} = 0$ on (B). No-slip boundary conditions $\boldsymbol{u}|_{\partial\Omega_D} = \boldsymbol{0}$ are applied along the channel walls (D). Natural boundary conditions (see section §3.4.1) consisting of $\boldsymbol{u}\perp\boldsymbol{n}|_{\partial\Omega_C} = 0$ and $\boldsymbol{u}\|\boldsymbol{n}|_{\partial\Omega_C}$ and $\boldsymbol{\tau}|_{\partial\Omega_C}$ as variable as well as a zero datum pressure are applied along the outflow boundary (C).

Physiologically realistic parameters for the flow are set as in [84], while parameters concerning the infinite and zero shear-rate viscosity function are used as in [48], where a similar shear-thinning viscoelastic model was used to simulate flow through an aneurytic channel. Specific parameters for the Carreau-Yasuda model are used as prescribed in the review by Robertson [82]. The dimensional quantities are summarized in table 7.1, where from the scale of the channel L it can be seen that we are describing small arteries or larger arterioles (see [48]). The dimensionless equivalents that will be used in the numerical methods are summarized in table 7.2.

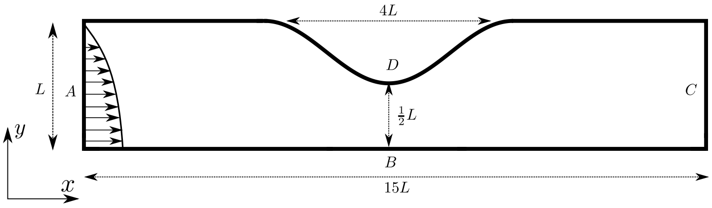

Figure 7.2. – Stenosed channel computational geometry.

Physiological Parameters	Value	Unit	Description
U	0.01	$m.s^{-1}$	Characteristic Velocity
L	0.0016	m	Characteristic Length (half-height of channel)
ρ	1053.6	$kg.m^{-3}$	Plasma Fluid Density
λ	0.06	s	Viscoelastic Relaxation Time
η_N	0.001	$kg.s^{-1}.m^{-1}$	Newtonian Plasma Viscosity
η_0	0.0326	$kg.s^{-1}.m^{-1}$	Zero-shear Viscosity
η_∞	0.003	$kg.s^{-1}.m^{-1}$	Infinite Shear Viscosity
ω	2π	$rad.s^{-1}$	Angular Frequency of Pulsatile Flow

Table 7.1. – Physiological parameters chosen for the model to realistically describe pulsatile flow in a small stenosed artery.

Dimensionless Parameter	Relation	Value	Description
Re	$\frac{\rho U L}{\eta_0}$	0.517	Reynolds Number
We	$\frac{\lambda U}{L}$	0.375	Weissenberg Number
α	η_∞/η_0	0.092	Amount of Shear-Thinning
β	η_N/η_0	0.031	Newtonian\Viscoelastic Influence
Λ	fitted [82]	1.902	Carreau-Yasuda Parameter
a	fitted [82]	1.25	Carreau-Yasuda Parameter
n	fitted [82]	0.22	Carreau-Yasuda Parameter
ω'	$\omega/(\frac{L}{U})$	1.005	Dimensionless Angular Frequency

Table 7.2. – Dimensionless parameters as used in the numerical model, with included definitions of non-dimensional groups/parameters and values determined from the physiologically realistic set in table 7.1

Initially a steady-state solution is obtained by time-stepping towards equilibrium, with constant boundary conditions, corresponding to the velocity and stress values of equation (7.2) at $t = 0$. The solution was considered as converged when the difference in solution between time steps fell below the value $10^{-6}\Delta t$. The obtained steady solutions were then used as initial conditions for the pulsatile flow in the transient simulations. These simulations were allowed to continue for a total dimensionless time of 20, over which multiple oscillations could occur. A time step of $\Delta t = 0.01$ was used in all the calculations.

In order to compare solutions using different models, the velocity boundary conditions are normalized to have unit average velocity across the open channel. This is necessary since for shear-thinning fluids the same pressure gradient will result in higher flow rates.

7.3. Results

7.3.1. Steady-State Results

The steady-state solutions for the GOB model under the above mentioned parameters and boundary conditions are shown in figure 7.3. In (a), the velocity magnitude is shown superimposed with a vector plot. In (b),(c) and (d) the τ_{xx}, τ_{xy} and τ_{yy} components of extra stress are represented respectively.

In figure 7.3 (a) a blunted parabolic velocity profile can be seen in the unconstricted channel, characteristic of a shear-thinning fluid. Furthermore, due to the low Reynolds number, there is no recirculation downstream from the constriction. In (b) the τ_{xx} component of stress exhibits the largest values near the middle of the obstruction, where the flow velocity is highest and stretching along the flow would occur. In (c) the shear component τ_{xy} shows pronounced maximum and minimum near the exit and entry of the stenosis respectively. This corresponds to the region where the vertical component of velocity is highest as the fluid moves around the constriction and is related to a stretching of the fluid perpendicular to the flow. Lastly, in (d) the τ_{yy} stress component exhibits high positive values along the channel wall at the entry to the constriction and along the symmetry axis just past it. This corresponds to vertical stretching and compression of the fluid. A slight amount of asymmetry downstream can be seen in the profiles of all the polymeric stress components.

Mesh Sensitivity Study

To test the validity of our solution and to provide a comparison of the performance of the two extra-stress element choices (Q_0^{disc} and Q_1^{disc}), the problem was solved on a sequence of six meshes denoted as M1-M6 and shown in figure 7.4. M1 is the coarsest mesh and acts as a base from which the remaining meshes will be defined. Mesh M2 consists of a once global refinement of M1, while M3-M6 are produced by systematically refining in the region of high stress-activity, i.e. along the channel wall. A summary of the mesh details is presented in table 7.3.

It can be seen that even though the finest mesh M6 has a modest number of cells, the computational cost is high even at this level of refinement as the number of coupled degrees of freedom is large and the maximum allowed time step decreases with mesh-refinement. Nonetheless, due to the nature of the refinement we are able to capture the steep stress gradients and obtain convergent results.

By considering the solutions across the various meshes, we observe that the velocity and pressure fields show little variability with refinement. This is due to the smooth solution and higher-order elements used to approximate these fields. The extra-stress field does however exhibit some mesh sensitivity, particularly on the wall of the channel inside the

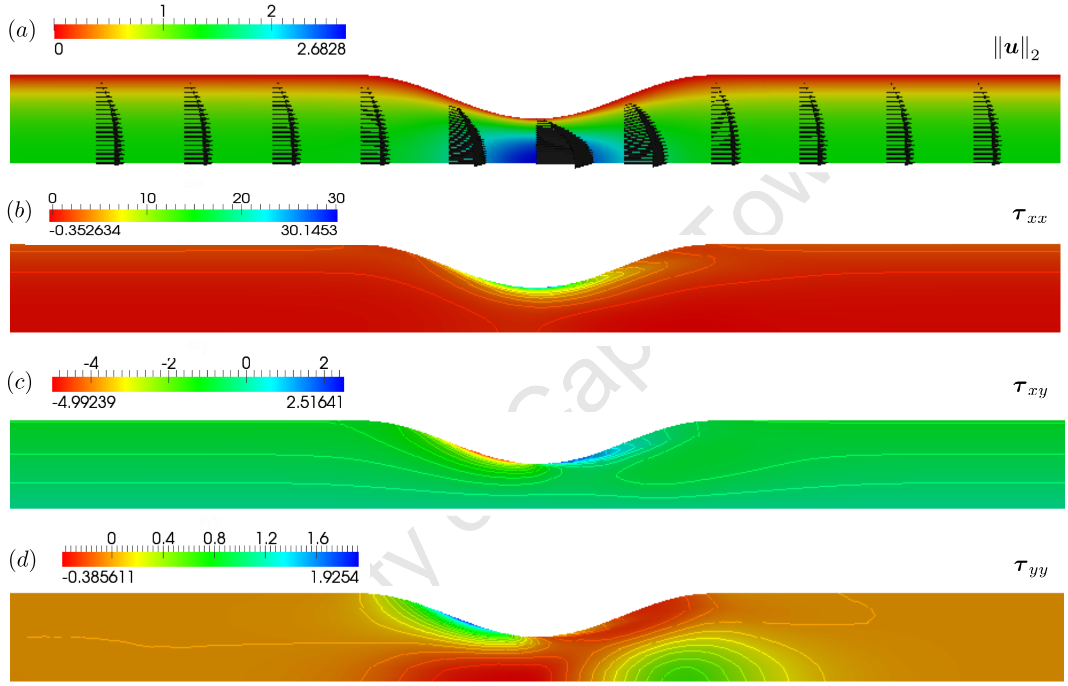

Figure 7.3. – Steady-state flow profiles for the generalized Oldroyd-B model in stenotic channel using mesh M6. Profiles are shown for the region near the constriction to illustrate the most interesting flow features. (a) Velocity magnitude and superimposed vector plot. (b) Horizontal normal stress τ_{xx} (c) Shear stress τ_{xy} (d) Vertical normal stress τ_{yy}

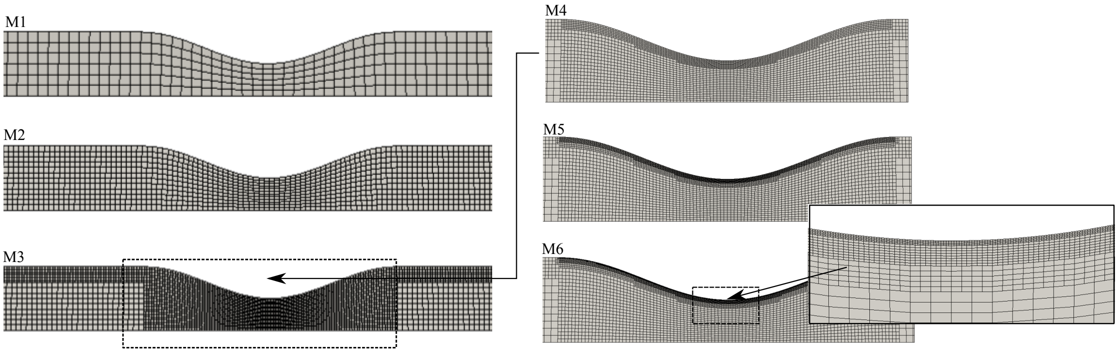

Figure 7.4. – Sequence of refined meshes for the stenotic channel M1-M6. M1,M2 and M3 are shown in the region around the constriction, while the more refined M4,M5 and M6 are shown as closeups over the constricted channel wall, where the additional refinement is performed.

			DoFs			
Mesh	# Cells	h	Q_2- $\boldsymbol{u}$	$P_1^{\text{disc}} - p$	$Q_0^{\text{disc}} - \boldsymbol{\tau}$	$Q_1^{\text{disc}} - \boldsymbol{\tau}$
M1	558	0.1821	4862	1674	1674	6696
M2	2232	0.0910	18650	6696	6696	26784
M3	5256	0.0455	43942	15768	15768	63072
M4	6414	0.0231	53846	19242	19242	76968
M5	8748	0.0116	73770	26244	26244	104976
M6	10914	0.0058	93542	32742	32742	130968

Table 7.3. – Mesh refinement details for flow in a stenotic arteriole. A summary of the number of degrees of freedom for each field, number of cells and characteristic mesh size h is shown.

constriction. To illustrate this we show the plot of each component of stress along the channel wall in figure 7.5 for each of the six meshes M1-M6 when using both $Q_1^{\text{disc}}$and Q_0^{disc} elements for the extra stress.

Initially we may observe that all meshes and element choices exhibit similar qualitative profiles, which is encouraging for the validity of method. Additionally we may observe that when using Q_1^{disc} elements, the extra stress appears to have converged with mesh refinement by M6. Furthermore, the horizontal stress component τ_{xx} is the slowest to convergence since this field exhibits the steepest boundary layer. The Q_0^{disc} elements appear to under-predict the stress, particularly for the τ_{xx} component in (a) where even for the finest mesh convergence is not attained. The shear stress τ_{xy} in (b) and vertical normal stress τ_{yy} in (c) show only slight variation between the Q_0^{disc} and Q_1^{disc} solutions, where the lower-order approximations are near converged. Although full convergence is not obtained, the trend with refinement is correct. Even finer meshes are required to

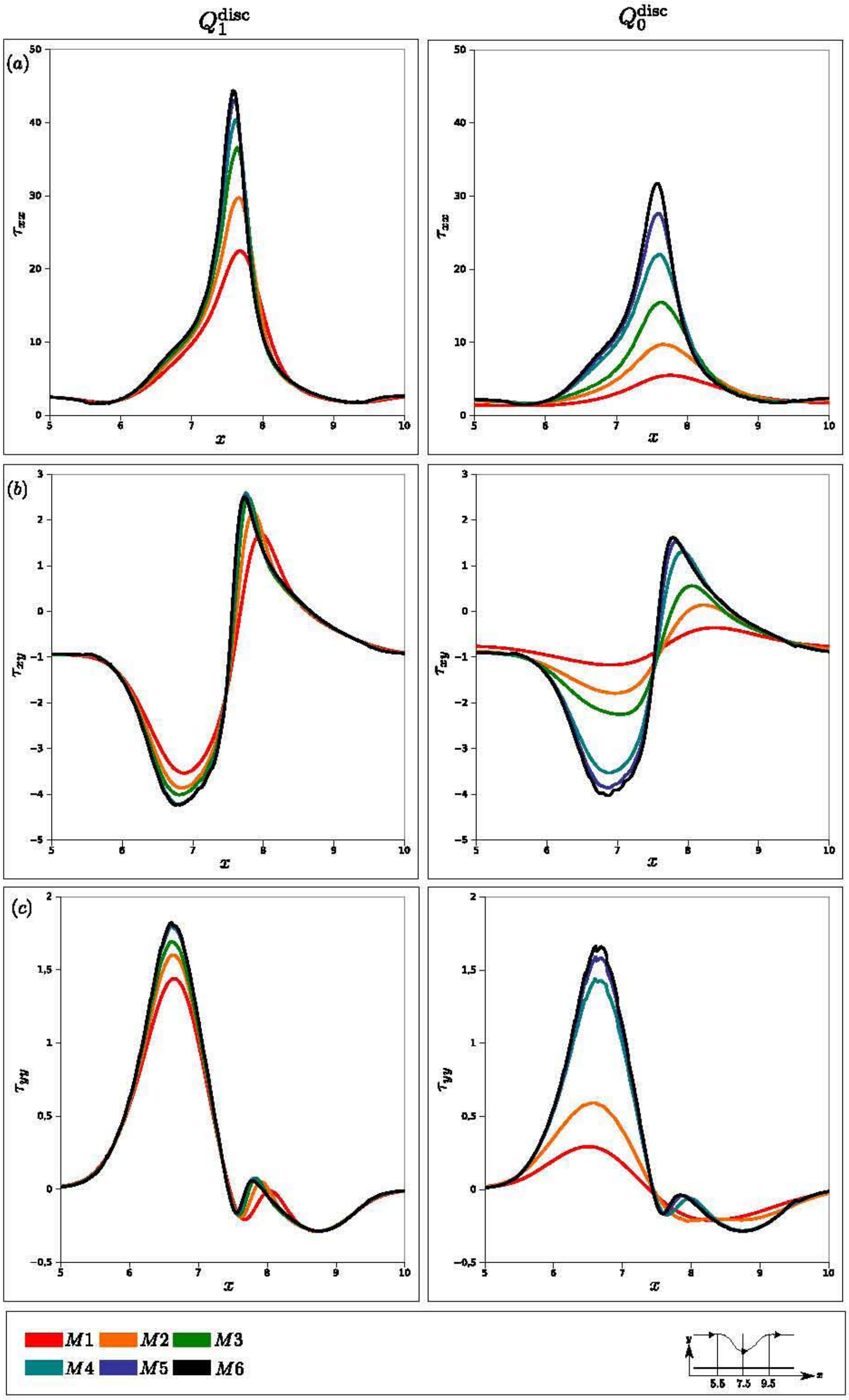

Figure 7.5. – Steady-state extra stress profiles along the channel wall and obstruction on each level of refinement M1-M6 using both Q_1^{disc} and Q_0^{disc} elements. (a) Horizontal normal stress τ_{xx} . (b) Shear-stress τ_{xy}. (c) Vertical normal stress τ_{yy}.

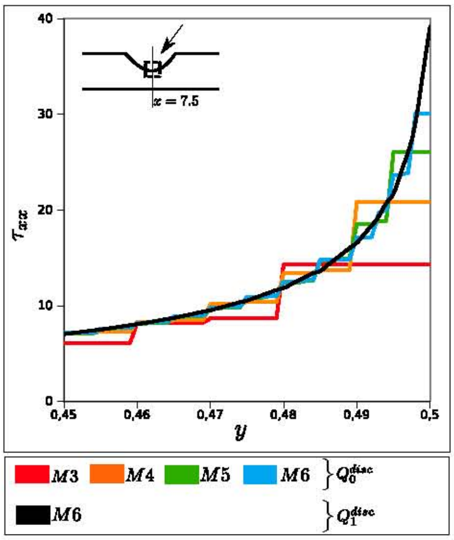

Figure 7.6. – Plot of τ_{xx} along the line $x = 7.5$ near the middle of the stenotic obstruction. Six levels of refinement M3-M6 are shown when using Q_0^{disc} elements and compared to the near-converged Q_1^{disc} solution on M6.

fully resolve the stress along the channel wall. Further refinement will not be considered at this point due to the prohibitive computational time and resources.

The apparent under-performance of the Q_0^{disc} elements in figure 7.5 is as a result of their inability to resolve sharp stress gradients along boundaries. They predict the stress at the centroid of the cell, which is a finite distance from the boundary, resulting in under-prediction. This is illustrated in figure 7.6 where a plot of τ_{xx} using Q_0^{disc} elements on M3-M6 is presented along the line $x = 7.5$, the mid-line of the constriction. These profiles are superimposed with the converged Q_1^{disc} on M6. It can be seen that the step-like Q_0^{disc} solutions intersect the smooth Q_1^{disc} solution near the centre of each step. These solutions are thus as accurate as the discretization. This fact combined with the resulting robustness of the resulting algorithm implies that this element choice provides a useful way for viscoelastic flows, particularly when combined with adaptive mesh refinement.

Slope Limiting

We continue our investigation by now considering the effects and purpose of introducing a slope limiter (see section §4.5). It is known that discontinuous elements of order higher than zero may produce non-monotone solutions in regions of sharp gradients, which could in turn lead to instability in the solution. This loss in monotonicity occurs predominantly on coarse meshes, where the gradients are more poorly approximated, and may be controlled by an appropriate use of a slope limiter.

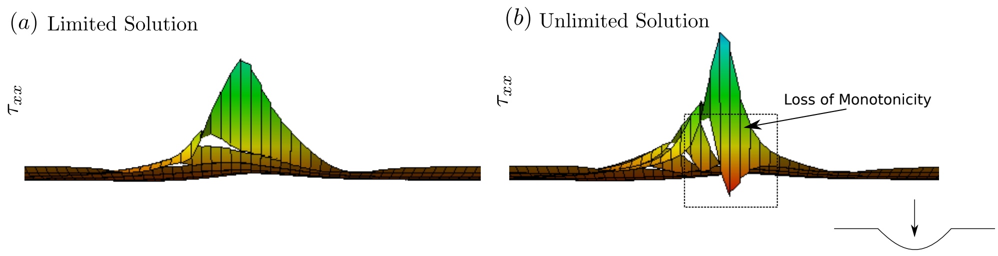

Figure 7.7. – Surface plot of τ_{xx} vs. (x, y) as viewed from behind the obstruction. (a) A slope limiter with parameter $\alpha_{SL} = 0.55$ is applied to all components of stress after each time step. (b) The original unlimited solution.

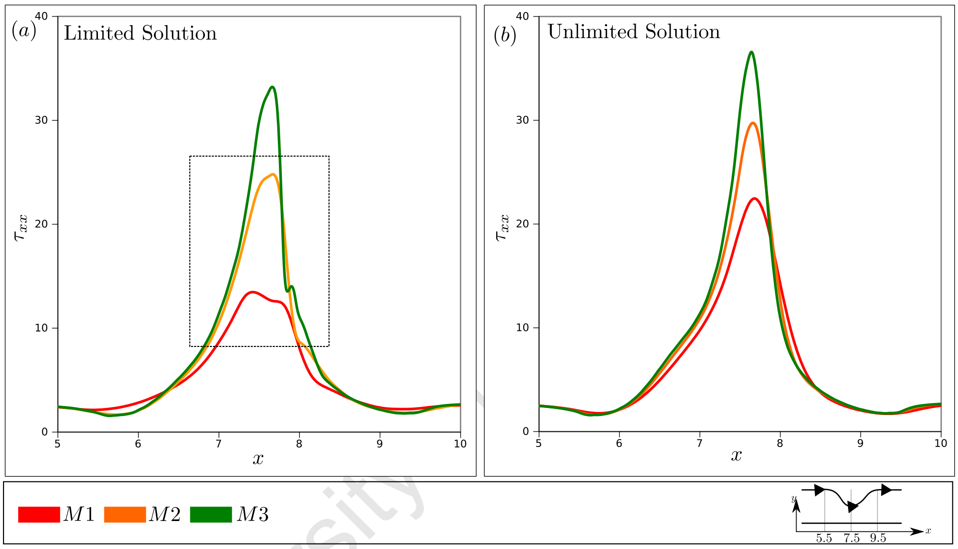

Figure 7.8. – Plot of τ_{xx} along the channel wall and obstruction on meshes M1-M3. (a) Solution when slope limiter with parameter $\alpha_{SL} = 0.55$ is applied. (b) Original unlimited solution.

To illustrate this point, consider that under slight adjustment of the parameters the scheme using Q_1^{disc} first becomes unstable in the boundary layer on the channel wall within the constriction. In figure 7.7 (b) a surface plot of τ_{xx} vs. (x, y) just prior to divergence is shown, as viewed from behind the constriction. From this perspective, the loss of monotonicity of τ_{xx} is clear and corresponds directly to the region where instability first occurs. The solutions in figure 7.7 were obtained on the coarsest mesh M1.

If the slope limiter with set parameter $\alpha_{SL} = 0.55$ is applied after each time step, no instability is observed. This improvement in stability is additionally characterized by an increased maximum allowed time step under the original problem parameters. The resulting limited stress profile, as shown in figure 7.7 (a), is much smoother and completely monotone. However, the stress for the limited solution appears to have a lower maximum than the unlimited counterpart.

Therefore this additional stability comes at the cost of accuracy. This may be seen in figure 7.8, where a plot of τ_{xx} along the channel wall for the three coarsest meshes (M1-M3) is shown when a slope limiter is applied in (a) and the original unlimited solution in (b). The flattening of the stress may be more clearly seen in this plot by the discrepancy between the limited and unlimited solution on M1 and M2 (enclosed by a rectangle). There appears little difference on the finer mesh M3 between the limited and unlimited solution. This result is expected, since a discontinuous solution would converge to the "real" monotone continuous solution with refinement. Since the application of the slope limiter becomes expensive and enforcing monotonicity is less required on finer meshes, it should only be applied when appropriate.

Boundary Representation

As was mentioned in section §3.1.4, the cells which define a mesh are themselves defined through a Q_1 mapping of a bi-unit square parent cell. Thus cells which lie on curved boundaries are constructed by placing the vertices on the boundary and then connecting these points with straight line segments. This introduces a problem during refinement since if we naively divide a boundary cell into four the newly inserted node will not lie on the domain boundary, as is seen in figure 7.9 (a). Hence, irrespective of the refinement throughout the mesh, the boundary will remain discretized coarsely. To overcome this we may take the exact form of the boundary into account during refinement and place new nodes explicitly on the boundary, as seen in figure 7.9 (b). This does however require that the exact form of the boundary is known, or is at least well approximated. This requirement may not always be possible for more complex geometries and especially so for 3D meshes.

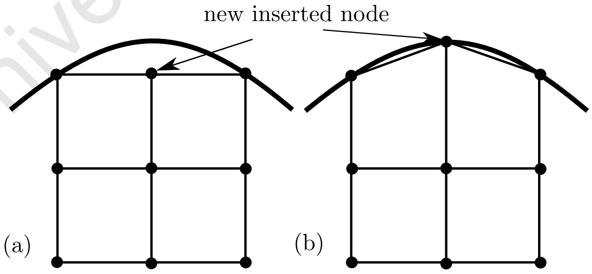

Figure 7.9. – Mesh refinement on curved boundaries. (a) Refinement by subdividing the coarse cells only. (b) Refinement by subdividing the coarse cells and considering the boundary definition.

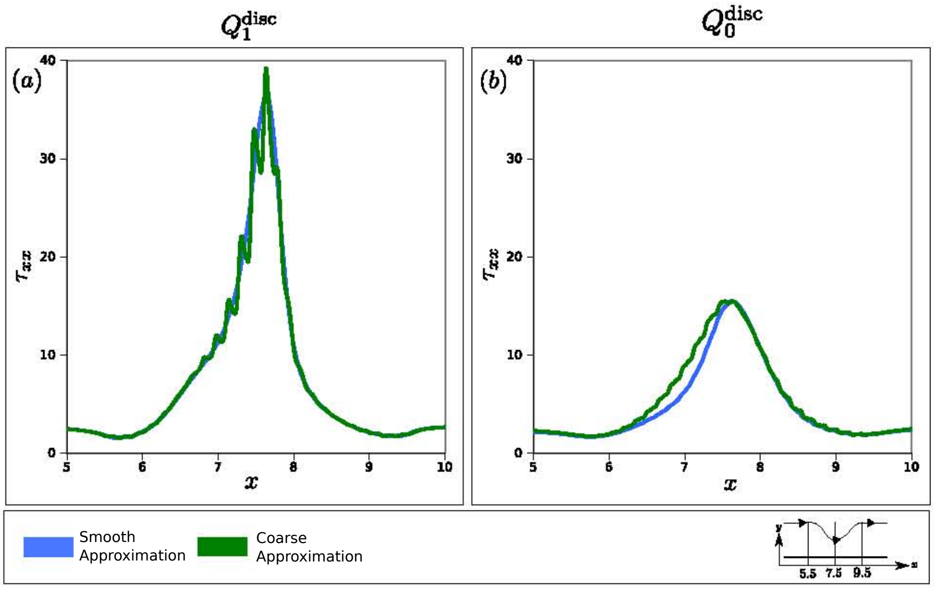

Figure 7.10. – Plot of τ_{xx} along the channel wall and obstruction using (a) Q_1^{disc} and (b) Q_0^{disc} stress elements when boundaries are approximated both smoothly and coarsely.

In this section we investigate the influence of taking into account the curve which defines the stenotic obstruction (7.1) during refinement. In figure 7.10 a plot of τ_{xx} along the channel wall is presented for the cases when the boundary is approximated both smoothly and coarsely on M3 using both (a) Q_1^{disc} elements and (b) Q_0^{disc}elements. In figure 7.10 (a) it may be observed that by using Q_1^{disc} elements the resulting solutions are very sensitive to the smoothness of the boundary approximation, with large non-physical oscillations present when the boundary is approximated coarsely. The solutions obtained using Q_0^{disc} elements on the other hand, show a far lower sensitivity to the boundary representation and remain smooth in both cases, as may be seen in figure 7.10 (b).

7.3.2. Model Comparison

The generalized Oldroyd-B model describes fluids with both shear-thinning and viscoelastic properties. Under an appropriate choice of parameters this model reduces to three other important models which describe fluids with only one or none of these properties, namely: the Newtonian (N), generalized Newtonian (GN) and Oldroyd-B (OB) model. This provides an interesting opportunity to study the influence of each of these properties by comparing the solutions obtained for each model.

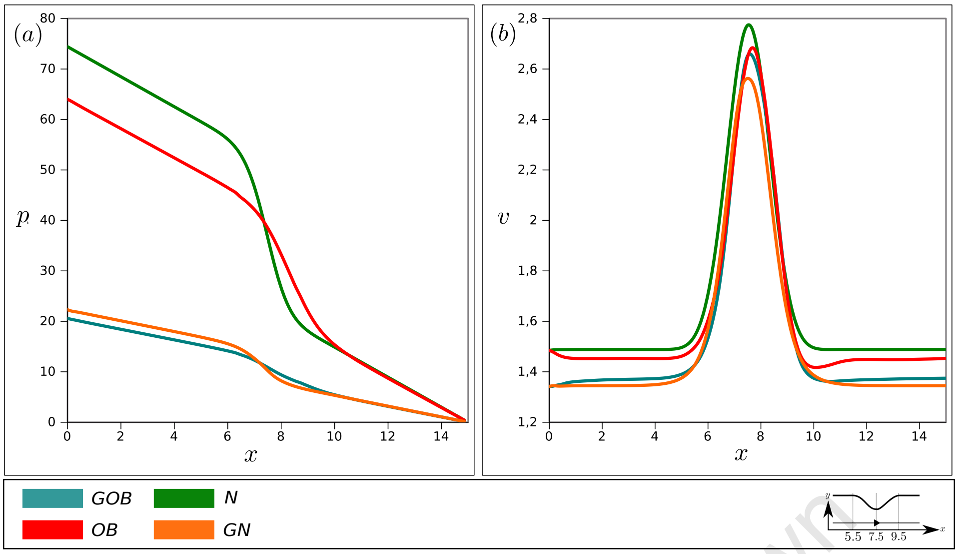

Figure 7.11. – Steady-state plot of (a) pressure and (b) velocity magnitude along the symmetry axis of the channel for the N, GOB, OB and GN model with normalized flow-rate for each model.

Velocity and Pressure

In [93] the pressure drop over a stenotic contraction was experimentally measured, which provided a base from which numerical studies may validate their work. Due to the 2D geometry used here, qualitative comparison is unlikely. However, some qualitative trends may be extracted. In figure 7.11 (a) the pressure along the axis of symmetry of the channel is plotted for all four models. It can be seen that the non-shear-thinning models (N and OB) show similar pressure gradients in the unconfined segments, as do both the shear-thinning models (GN and GOB). A large difference between both pairs is also observed, with the shear-thinning models predicting a much lower pressure gradient, as was similarly observed in [12]. In both the shear-thinning and non-shear-thinning cases, the viscoelastic models predict a smaller pressure drop over only the constriction than their purely viscous counterparts.

In figure 7.11 (b) the velocity along the axis of symmetry is shown for each of the four models. There is little difference between the solutions using different models. Both shear-thinning models show slightly lower average velocities since the models are normalized according to flow-rate, while both the GOB and GN model have a blunted parabolic velocity profile.

Wall Shear Stress (WSS)

As mentioned in the introduction, the development and evolution of an obstructed arteriole is greatly dependent on the mechanical properties of the plaques and fats which build up on the arterial walls. Apart from the material properties of these fat deposits, the stress exerted on these entities by the blood flow will determine the behaviour of the constriction. In the review of Berger [9], it is stated that the most important physical property of the blood flow in this regard is the wall shear stress (WSS) g_t. This is defined as the magnitude of the tangential traction vector along the channel wall, as

$$\begin{aligned} \boldsymbol{g}_t &= \boldsymbol{g} - (\boldsymbol{g} \cdot \boldsymbol{n}_s)\boldsymbol{n}_s \quad \text{where } \boldsymbol{g} = \boldsymbol{\Sigma} \cdot \boldsymbol{n}_s, \\ g_t &= \|\boldsymbol{g}_t\| \end{aligned} \tag{7.3}$$

where $\boldsymbol{\Sigma}$ is the Cauchy stress and $\boldsymbol{n}_s$ be the outward pointing normal to the surface. Although there is a dispute in the literature whether a low or high WSS is a more severe condition, the profile of this stress is clearly of physiological importance. The definition of stress is tabulated in table 7.4 for each model.

Model Type	Cauchy Stress ($\boldsymbol{\Sigma}$)
Newtonian	$-p\boldsymbol{I} + \dot{\boldsymbol{\gamma}}$
Oldroyd-B	$-p\boldsymbol{I} + \beta\dot{\boldsymbol{\gamma}} + \boldsymbol{\tau}$
Shear-Thinning	$-p\boldsymbol{I} + \mu(\dot{\gamma})\dot{\boldsymbol{\gamma}}$
Generalized Oldroyd-B	$-p\boldsymbol{I} + \beta\dot{\boldsymbol{\gamma}} + \boldsymbol{\tau}$

Table 7.4. – Stress definition for each model considered.

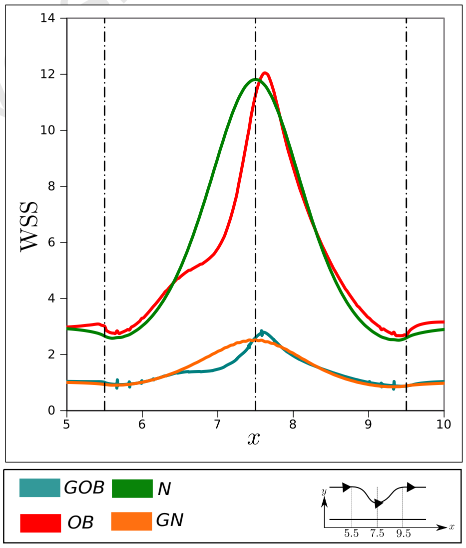

Figure 7.12. – Plot of wall shear-stress (WSS) along the channel wall and obstruction for a N, GOB, OB and GN fluid.

In figure 7.12 the WSS is shown for the four models along the channel wall near the stenotic obstruction. All four models exhibit similar behaviour, with the maximum stress present near the middle of the obstruction where the velocity is greatest. The value of the WSS also dips at both the entry and exit of the obstruction. The most noticeable difference between the models is the average magnitude between the shear-thinning and non-shear-thinning models, where the latter show many times larger WSS. It should be restated that models are normalized according to flow-rate and not according to pressure gradient. This lower WSS is thus related to the smaller pressure gradients for the shear-thinning, as shown in figure 7.11 (a). It is also observed that the peak of the WSS for the viscoelastic models appears shifted downstream along the stenosis as compared to the viscous models which have symmetric profiles around the middle of the obstruction. This is expected and due to the convection in the polymeric stresses for the viscoelastic models.

In the numerical work of [65], similar profiles for wall shear stress were obtained, although these were obtained at a higher Reynolds number where recirculation occurred downstream from the obstruction. In the work of [84], where a FENE viscoelastic fluid was considered, the decrease in stress with increased shear-thinning was also observed, correlating to the profiles presented in figure 7.12. The variation in shear-thinning was accomplished by decreasing the maximum extensibility of the dumbbells in the FENE model. The large variation of WSS profiles between models illustrates the importance of a comprehensive description for blood.

Viscosity

Blood is a highly shear-thinning material, as can be seen by the parameters in table 7.2 where the ratio of zero to infinite shear-rate viscosity is approximately 50. The polymeric viscosity is thus expected to vary greatly throughout the domain. We seek next to investigate the influence of viscoelasticity to profiles of polymeric viscosity by considering the profiles for this quantity when using both the GOB and GN models in figure 7.13. For both models the straight segments show higher viscosity in the centre and lower values along the channel wall, where the shear-rate is highest. This results in the blunted velocity profiles which is characteristic of a shear-thinning fluid. In the stenotic region, very low viscosity is observed along the obstruction where the shear-rate is highest. This correlates with the findings of the lower WSS values for the shear-thinning models. By comparing the two models it can be seen that presence of viscoelasticity in the generalized Oldroyd-B model decreases the influence of shear-thinning near the central axis, both in the straight and obstructed segments. As with the wall shear stress, some convection related asymmetry is present for the GOB model.

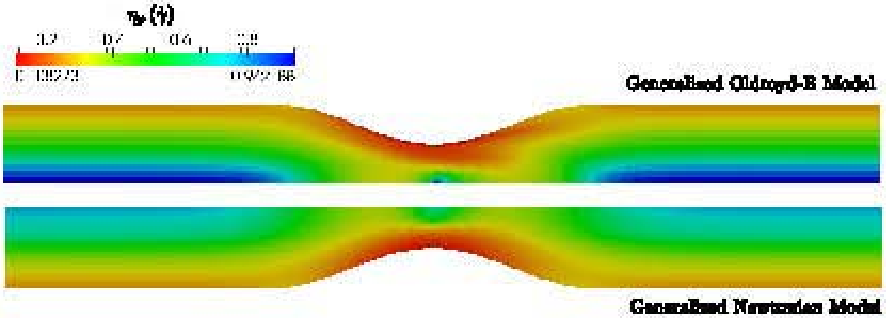

Figure 7.13. – The polymeric viscosity $\eta_p(\dot{\gamma})$ for steady flow (from left to right) for the generalized Oldroyd-B model (top) and shear-thinning model (bottom).

7.3.3. Pulsatile Flow

In the next stage of our investigation we seek to simulate pulsatile blood flow which occurs naturally in the circulatory system. This is accomplished by setting sinusoidally varying velocity (7.2) and corresponding stress boundary conditions at the inflow boundary. We then obtain transient solutions with our time-dependent algorithm. In figure 7.14, we plot for all four models the behaviour with time of (a) the magnitude of the velocity and (b) the pressure at the midpoint of the symmetry axis and additionally (c) the variation of the wall shear stress at the middle of the constriction on the channel wall.

Concerning the velocity magnitude, we observe that the shear-thinning models predict much larger amplitudes, particularly during the diastolic period, where the GOB model exhibits a much lower magnitude than any of the other models. By comparing the behaviour of the pressure, we observe that for the shear-thinning models there is a deviation from a sinusoidal profile, consisting of a flattened region during the low flow-rate phase. This effect is stronger for the GOB model than for the GN model. We also observe that there appears a relative phase-shift between the pressure and velocity profiles for the shear-thinning models. This is in close resemblance to the results in [75] and may be interpreted as treating the shear-rate-dependent viscosity as a complex viscosity in the linear limit. This is analogous to a combination of reactive and inductive electrical components in an alternating current circuit.

Concerning the behaviour of the WSS with time, we observe a *saw-tooth* profile for the GOB model, consisting of a rapid decrease to minimum and slow increase to maximum. We also observe an offset in average magnitude between the N and OB models; although both models had steady results of similar magnitude and both models have similar amplitudes during pulsatile flow. This may be explained by recalling that the viscoelastic models showed a slightly downstream *maximum* and hence the middle of the constriction does not correspond to the maximum WSS for these models.

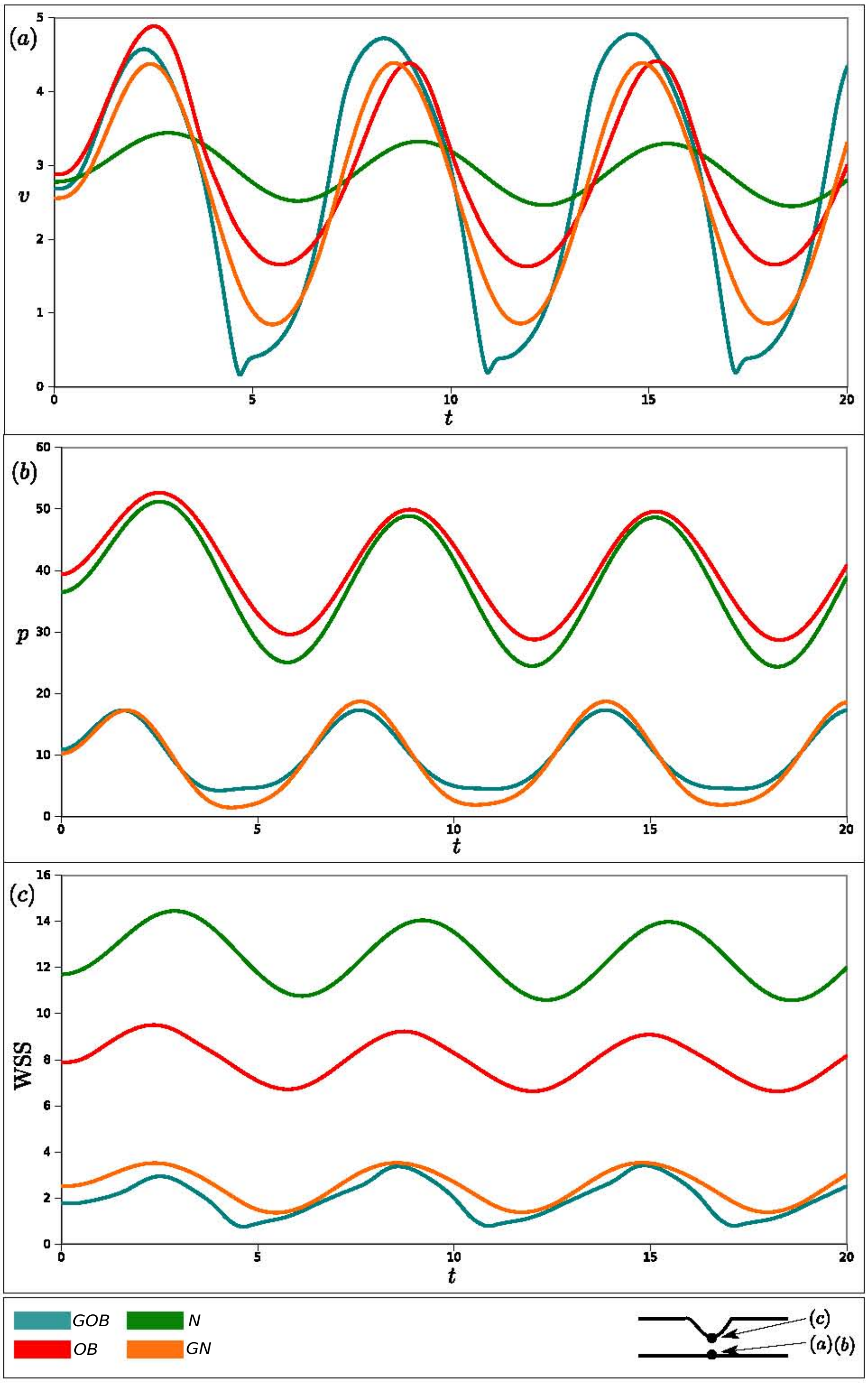

Figure 7.14. – Pulsatile flow for the GOB, OB, N and GN models. (a) Velocity magnitude variation with time at the midpoint along the symmetry axis. (b) The pressure variation with time at the midpoint of the symmetry axis. (c) WSS variation with time at the centre of the constriction.

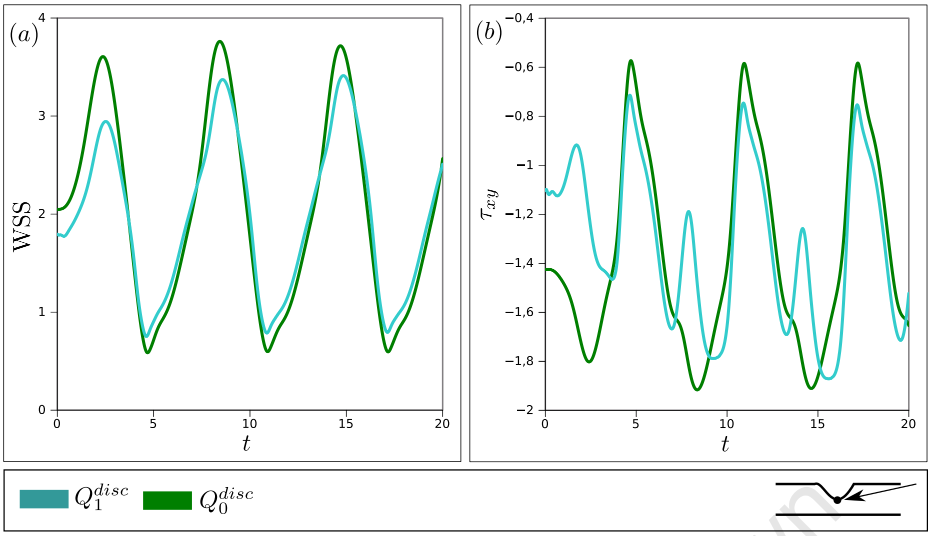

Figure 7.15. – Comparison between using Q_0^{disc} and Q_1^{disc} stress elements under pulsatile flow. (a) Variation of WSS with time at the centre of the constriction. (b) Variation of the τ_{xy} stress component with time at the centre of the constriction.

From this discussion we may conclude that: whereas during the steady flow, where the main flow features were primarily as a consequence of shear-thinning properties, during pulatile flow viscoelasticity has a far stronger presence. This presence is further amplified during the diastolic phase where the flow rate is low.

Element Choice

In this next section we compare the use of Q_0^{disc} and Q_1^{disc} approximations for the extra stress when simulating pulsatile flow. Qualitatively we observe similar behaviour when using both elements, with the quantitative differences mimicking those observed in the steady-state case. However, by observing the variation of the fields at specific points, some discernible differences were observed. In figure 7.15 we present a plot of (a) WSS vs. time and (b) polymeric shear stress τ_{xy} vs. time on the channel wall in the centre of the stenosis. In (a) we observe little difference in the behaviour of the WSS values, except during peak-flow, where the solutions using Q_0^{disc} elements exhibit a slightly larger magnitude. A much larger discrepancy is however observed between the two element choices in (b). The shear stress using Q_1^{disc} elements exhibits an additional *beat-like* frequency during the diastolic phase, which is not observed when using Q_0^{disc} elements. Although the reason for this difference is not clear, the presence of the “bump” in the Q_0^{disc} profile at the same time as the secondary oscillation in the Q_1^{disc} solution may indicate that this is due to a slower response for the Q_0^{disc} elements. This brings into question the influence of the time-discretization when comparing solutions using different elements and will hopefully form part of future work.

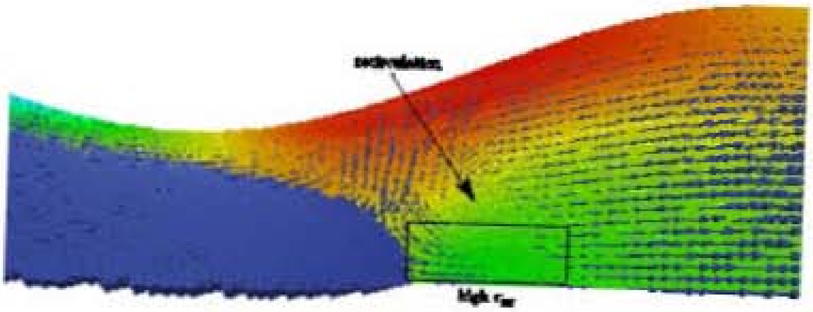

Figure 7.16. – Vector field plot of the velocity superimposed with a colour plot of the vertical normal polymeric stress τ_{yy} during diastolic phase where recirculation flow occurs.

Recirculation Flow

From the results in figure 7.14, we may infer that the most interesting flow features for the GOB model would occur during the diastolic phase of the pulse. This further emphasises that the non-Newtonian and viscoelastic effects are most prevalent in blood flow only at low flow-rates. Furthermore, the results so far suggest that in the GOB model, viscoelasticity and shear-thinning act almost as a linear combination of properties: implying that they produce no "new" flow features when acting in combination but merely stack their resulting effects. However, by observing the solution profile near the diastolic phase we encounter a flow phenomenon which occurs only for the GOB model, consisting of a region of recirculation which develops just past the constriction as the flow-rate decreases and then dissipates. For both the GN and OB models the flow-rate decreases similarly, but produces no such recirculation flow.

A vector plot of the velocity field shown in figure 7.16 at a time leading towards the diastole, shows this recirculation at the exit of the constriction. With time this region moves left towards the contraction until it dissipates when the flow-rate is lowest. This motion of the recirculation region coincides with the motion of a region of high τ_{yy} stress highlighted in figure 7.16. For the OB model, this region of high stress showed little motion during diastole as the flow-rate through the contraction varied with much smaller amplitude than for the GOB model. This behaviour was observed on all three meshes M1-M3 when using both Q_0^{disc} and Q_1^{disc} stress elements. Thus despite the small magnitude of this recirculation flow, this region of recirculation is not a numerical artifact and is thus a new flow feature arising only with the combination of viscoelastic and shear-thinning effects.

7.4. Summary

In this chapter we successfully applied our newly developed numerical method to simulate both steady and pulsatile flow of blood through a stenotic arteriole. We have illustrated the applicability of the numerical method by incorporating a physiologically fitted set of parameters for the model and shown it to produce reasonable preliminary results. Furthermore, this work may add to the literature of time-dependent simulations of shear-thinning viscoelastic flows, which to date and knowledge is limited to the works of Smith and Sequeria [84], Iolov *et.al.* [48] and Pontrelli [75]. The simultaneous treatment of the Newtonian, generalized Newtonian, Oldroyd-B and generalized Oldroyd-B models has also allowed for an interesting investigation of shear-thinning and elastic properties in isolation and combination.

8. Conclusion and Discussion

The main objective of this dissertation was to develop and implement a robust and efficient numerical scheme to simulate a two-dimensional time-dependent incompressible viscoelastic flow with a shear-rate-dependent viscosity, as described by the generalized Oldroyd-B model. Due to the known difficulties associated with simulating viscoelastic flow, various theoretical arguments on stability presented in the literature were considered for developing a free-energy dissipative scheme for both the Oldroyd-B and generalized Oldroyd-B model within the context of finite elements. The basis of these theoretical arguments revolved around the conservation of positive-definiteness of the conformation tensor $\boldsymbol{\sigma}$, which was shown to be true universally for the Oldroyd-B model and dependent on the positivity of a parameter ζ, which depends on the flow and model parameters. These arguments were also shown to carry over to the discrete problem when low-order piecewise constant Q_0^{disc} finite element approximations are used for the polymeric extra stress.

In light of these results, these elements were chosen for the extra stress along with corresponding stable choices of elements for the velocity and pressure fields, namely: biquadratic and linear discontinuous elements over quadrilaterals respectively. An alternative bilinear discontinuous element Q_1^{disc} for the extra stress was also considered to provide a basis to compare the stability and accuracy of each resulting scheme. An algorithm was then developed to solve the resulting mixed method problem, incorporating various techniques used in computational fluid dynamics, computational rheology and other numerical fields in order to improve the robustness and efficiency of the resulting scheme. These techniques included: a pressure-projection method, used to decouple the pressure variable and incompressibility constraint; a discontinuous Galerkin upwinding method, to stabilize the hyperbolic constitutive equation; a globalized Newton-Raphson scheme, to solve the nonlinear governing equations and a slope limiter, to preserve monotonicity in the discontinuous stress field when using higher-order elements.

In order to improve the efficiency of the algorithm a geometric multigrid preconditioner was incorporated. Various modifications were made to the multigrid method, namely: a cell-wise Vanka smoother, to act on the resulting block system; capabilities to handle hanging-nodes arising from non-uniform refinement and parallelization through mesh partitioning.

The numerical scheme was initially validated against two benchmark problems for the classic Oldroyd-B model: steady flow over a confined cylinder and start-up driven cavity flow. In the first problem, our transient algorithm was used to obtain steady-state solutions for a range of Weissenberg numbers. The algorithm produced results that compared well to the literature by considering the drag over the cylinder and the profiles of extra stress along the cylinder surface. By comparing results obtained using different choices of stress elements, the Q_1^{disc} elements were observed to be more accurate and better converging, although no stable solutions were obtained for $\text{We} \geq 0.8$. A piecewise constant approximation to stress resulted in a far more stable algorithm with no occurrences of instability in the considered range of parameters, and no loss in positive-definiteness for the conformation tensor observed.

By considering the energy density prior to the onset of instability using Q_1^{disc} elements, negative energy density and hence loss of positive-definiteness of $\boldsymbol{\sigma}$ was observed in the same region in which the solution first becomes unbounded. This additionally corresponded to the region where loss in monotonicity was observed for the extra stress. These properties were only point-wise features with both positive energy and positive-definiteness of $\boldsymbol{\sigma}$ being maintained when solutions were averaged over each cell. This indicates a strong link between stability and monotonicity and hence the apparent enhanced stability of using Q_0^{disc} stress elements, which naturally enforce monotonicity. The problem was then extended by considering the generalized Oldroyd-B model from which it was seen that the presence of shear-thinning acts to diminish the influence of viscoelasticity.

The second problem was a transient test case, allowing for the evolution of the free energy to be observed. Initially the Oldroyd-B model was treated and the improved stability of using Q_0^{disc} elements was again demonstrated as no instability was observed in the considered range of $\text{We} \leq 2$, while solutions obtained using Q_1^{disc} elements became unstable for $\text{We} \geq 0.4$. In a higher range of We, a clear distinction between accuracy and stability was illustrated as solutions converged with respect to energy, while they diverged with respect to mesh refinement. This raises questions concerning the connection and application of energy stability in relation to the high Weissenberg number problem.

Additionally, this problem served as a basis to test the numerical consequences of the requirement $\zeta \geq 0$ for the generalized Oldroyd-B model. Using Q_0^{disc} elements within the considered range of parameters, this requirement was violated in regions throughout the domain, albeit slightly, and yet no loss of positive-definiteness of $\boldsymbol{\sigma}$ or instability was observed. The constraint on ζ was hence shown to be a weak requirement with a more rigorous numerical study in the future, involving more severe flow regimes, possibly illuminating the stringency of $\zeta \geq 0$ further.

An application of the numerical method to simulating pulsatile blood flow through a stenotic arteriole was then considered. Using a physiologically realistic set of parameters, both steady and pulsatile flow was simulated allowing for further comparisons between the two choices of stress elements. Similar observations with regards to accuracy, convergence and stability were made as in the benchmark problems. Furthermore, a greater sensitivity to a smooth refinement of boundaries was observed for the Q_1^{disc} elements. Additionally, the effect of an applied slope limiter was investigated in this context where it appeared to improve stability, but severely diminish accuracy on coarser meshes.

By comparing solutions using the generalized Oldroyd-B model to results using a Newtonian, generalized Newtonian and Oldroyd-B model (all obtained using the same numerical method) some interesting observations could be made as to the individual influence of shear-thinning and viscoelasticity. As in the benchmark problem, shear-thinning was shown to be a dominant property with regards to the magnitudes of stress, while viscoelasticity introduced convective features to the velocity and stress profiles. During pulsatile simulations, a region of recirculation flow was observed during the diastolic phase when using the generalized Oldroyd-B model only. This showed the emergence of a new flow feature which arises solely from the combination of shear-thinning and viscoelastic properties.

In summary, the developed numerical scheme is robust and efficient, particularly when Q_0^{disc} stress elements are used to approximate stress. Although the resulting scheme using these elements is inaccurate and slow to converge, it produces qualitatively reasonable results very cheaply. Furthermore, by incorporating adaptive refinement in regions of high activity, quantitatively reasonable results may similarly be obtained. These elements exhibit natural stability related to their preservation of monotonicity. When using Q_1^{disc} elements, the scheme, although more accurate, is too sensitive to discretization parameters to easily handle a larger class of geometries and problems.

Future work arising from the results presented in the dissertation may focus on additional numerical tests, theoretical work and improvements to the numerical method as a whole. Further numerical tests may focus on more extensive mesh sensitivity studies. In particular, focus should be placed on conclusively showing convergence with mesh refinement when using Q_0^{disc} stress elements. Such a study could also produce an estimate for the order of convergence of the method. Sensitivity studies on the time discretization is another avenue worth exploring, in particular the influence that the time step has on the stability of the method.

Further theoretical work may focus on bridging the results for the continuous generalized Oldroyd-B problem to its discrete form, as was done for the classic Oldroyd-B model. Concerning the numerical method, perhaps the biggest weakness of the current scheme is in the Vanka smoother within the multigrid preconditioner. This introduces a limit on the maximum time step inversely proportional to the discretization size. A streamline reordering of cells, patch-wise smoothing and overall alternative smoothers are all potential options for improvement in this regard. Additionally, improvement may by made by incorporating automatic adaptivity in both spatial and time discretizations. In terms of implementation, a distributed computing parallelization should be considered, particularly if the numerical scheme is to handle larger problems. An investigation into porting aspects of the multigrid preconditioner to GPU architectures may also be rewarding.

A. Poiseuille Flow

A.1. Newtonian Fluids

Flow of an incompressible fluid through a circular pipe of constant cross-section driven by a constant pressure gradient is referred to as Poiseuille flow and is one the most popular and fundamental types of flow. It is also one of the few geometries and boundary conditions for which there exists an analytical solution to the Navier-Stokes equations

$$\begin{aligned} \mathrm{Re}\frac{\partial \boldsymbol{u}}{\partial t} + \mathrm{Re}\, \boldsymbol{u} \cdot \boldsymbol{\nabla} \boldsymbol{u} + \boldsymbol{\nabla} p - \boldsymbol{\nabla^2} \boldsymbol{u} &= 0, \\ \boldsymbol{\nabla} \cdot \boldsymbol{u} &= 0, \\ \text{where } \boldsymbol{u} &= \begin{bmatrix} u_x & u_y \end{bmatrix}^T . \end{aligned} \tag{A.1}$$

Consider a 2D channel $\{(x, y) \in \mathbb{R}^2 \mid x \in \mathbb{R} \text{ and } -h < y < h\}$, where no-slip boundary conditions are applied along the walls $\boldsymbol{u}|_{y=\pm h} = 0$. We assume the solution is steady, i.e. $\frac{\partial \boldsymbol{u}}{\partial t} \equiv 0$ and also take into account the symmetry in the x direction, i.e. in the limit of an infinite channel there exists no variation in the velocity field with respect to x. From these assumptions it follows that the velocity has no component in the y direction. This may be expressed as $\frac{\partial \boldsymbol{u}}{\partial x} \equiv 0$ and $u_y \equiv 0$ respectively. As we consider only a constant pressure gradient under the same considerations of symmetry as above, we may write $\boldsymbol{\nabla} p = \begin{bmatrix} C_1 & 0 \end{bmatrix}$, where $C_1 = \frac{dp}{dx}$ is a constant. With the assumptions and notation above, we may reduce the Navier-Stokes equations (A.1) to

$$\frac{\partial^2 u_x}{\partial y^2} = C_1. \tag{A.2}$$

This differential equation can be easily solved with the above specified boundary conditions to produce the solution

$$u_x(y) = -\frac{3}{2}\left[\left(\frac{y}{h}\right)^2 - 1\right] \tag{A.3}$$

where the velocity is normalized across the channel. Using the above solution, the pressure gradient is fixed and may be expressed as

$$\frac{dp}{dx} = C_1 = -\frac{3}{h^2}. \tag{A.4}$$

A.2. Oldroyd-B Fluids

The Oldroyd-B model is a complex system of partial differential equations and hence few analytical solutions exist for this model. Poiseuille flow is one of the few scenarios for which analytical solutions for the Oldroyd-B model exist. These solutions are used to provide necessary inflow boundary conditions in geometries such as pipes and channels where both velocity and extra stress must be specified. This is often referred to as fully developed flow and has been applied as a boundary condition in section §6.1 for the problem of flow over a confined cylinder and in chapter 7 for the problem of blood flow through a stenotic channel.

Consider the system of partial differential equations that define the Oldroyd-B model

$$\begin{array}{rcl} \mathrm{Re}\dfrac{\partial \boldsymbol{u}}{\partial t} + \mathrm{Re}\ \boldsymbol{u}\cdot\boldsymbol{\nabla}\boldsymbol{u} + \boldsymbol{\nabla}p - \beta\ \boldsymbol{\nabla}^{2}\boldsymbol{u} - \boldsymbol{\nabla}\cdot\boldsymbol{\tau} & = & 0, \\ \boldsymbol{\nabla}\cdot\boldsymbol{u} & = & 0, \\ \boldsymbol{\tau} + \mathrm{We}\ \overset{\nabla}{\boldsymbol{\tau}} - (1-\beta)\left(\boldsymbol{\nabla}\boldsymbol{u} + (\boldsymbol{\nabla}\boldsymbol{u})^{T}\right) & = & 0. \end{array} \tag{A.5}$$

Under identical geometry and symmetry conditions as in section §A.1, it similarly follows that $\frac{\partial \boldsymbol{\tau}}{\partial x} = 0$. Under an imposed pressure gradient (not assumed to be steady) (A.5) reduces to the system of equations

$$\begin{array}{rcl} \mathrm{Re}\dfrac{\partial u_x}{\partial t} + \dfrac{dp}{dx} - \beta\dfrac{\partial^2 u_x}{\partial y^2} - \dfrac{\partial \tau_{xy}}{\partial y} & = & 0, \\ \tau_{xx} + \mathrm{We}\dfrac{\partial \tau_{xx}}{\partial t} - 2\ \mathrm{We}\ \tau_{xy}\dfrac{\partial u_x}{\partial y} & = & 0, \\ \tau_{xy} + \mathrm{We}\dfrac{\partial \tau_{xy}}{\partial t} - \mathrm{We}\ \tau_{yy}\dfrac{\partial u}{\partial y} - (1-\beta)\dfrac{\partial u}{\partial y} & = & 0, \\ \tau_{yy} + \mathrm{We}\dfrac{\partial \tau_{yy}}{\partial t} & = & 0, \end{array} \tag{A.6}$$

where the original tensor equation is expanded using the notation $\boldsymbol{\tau} = \begin{bmatrix} \tau_{xx} & \tau_{xy} \\ \tau_{xy} & \tau_{yy} \end{bmatrix}$. If we assume steady flow, the equations in (A.6) may be further reduced to

$$\begin{array}{rcl} \tau_{xx} & = & 2\mathrm{We}\ \tau_{xy}\dfrac{\partial u_x}{\partial y} = \dfrac{18\ \mathrm{We}\ (1-\beta)}{h^2}\left(\dfrac{y}{h}\right)^2, \\ \tau_{xy} & = & (1-\beta)\dfrac{\partial u_x}{\partial y} = -\dfrac{3\ (1-\beta)}{h}\left(\dfrac{y}{h}\right), \\ \tau_{yy} & = & 0 \end{array} \tag{A.7}$$

where the velocity solution is unchanged from (A.3).

If we consider an unsteady solution, for example pulsatile flow, the first-order linear ODE's in can be solved by using an integrating factor method, assuming a known velocity solution. We initially solve for τ_{xy} and then use this solution to obtain τ_{xx} by evaluating the integrals

$$\begin{aligned} \tau_{xy}(y,t) &= \frac{1-\beta}{\mathrm{We}} \int\limits_0^t \mathrm{e}^{\frac{1}{\mathrm{We}}(t'-t)} \frac{\partial u_x}{\partial y}(y,t')\mathrm{d}t', \\ \tau_{xx}(y,t) &= 2 \int\limits_0^t \mathrm{e}^{\frac{1}{\mathrm{We}}(t'-t)} \tau_{xy}(y,t') \frac{\partial u_x}{\partial y}(y,t')\mathrm{d}t'. \end{aligned} \tag{A.8}$$

These integrals can be solved analytically or numerically, depending on the simplicity and availability of the velocity solution. When solving (A.8) numerically the bounds of the integral are changed such that the best known solutions at the previous time t_n are used to obtain estimates at a time t_{n+1}, expressed as

$$\begin{aligned} \tau_{xy}(y,t_{n+1}) &= \mathrm{e}^{-\frac{\Delta t}{\mathrm{We}}} \tau_{xy}(y,t_n) + \frac{1-\beta}{\mathrm{We}} \int\limits_{t_n}^{t_{n+1}} \mathrm{e}^{\frac{1}{\mathrm{We}}(t'-t_{n+1})} \frac{\partial u_x}{\partial y}(y,t')\mathrm{d}t', \\ \tau_{xx}(y,t_{n+1}) &= \mathrm{e}^{-\frac{\Delta t}{\mathrm{We}}} \tau_{xx}(y,t_n) + 2 \int\limits_{t_n}^{t_{n+1}} \mathrm{e}^{\frac{1}{\mathrm{We}}(t'-t_{n+1})} \tau_{xy}(y,t') \frac{\partial u_x}{\partial y}(y,t')\mathrm{d}t'. \end{aligned} \tag{A.9}$$

This formulation will decrease the computational time and the error in the numerical integration at larger times.

A.3. Adaptive Simpson's Integration

When solving the integrals in (A.9) numerically using a quadrature rule, errors incurred from any such method will propagate and grow in time. Hence it is important to have proper control over this numerical integration error to ensure the validity of solutions. To this purpose an adaptive quadrature method based on Simpson's rule was implemented and used. The details of this method are available in most introductory texts on numerical methods (see for example [19]) and are presented below.

Consider the approximation of the integral of a generic function over the interval $[a,b]$ as given by Simpson's rule

$$\int\limits_a^b f(x)\mathrm{dx} \simeq S(a,b) \equiv \frac{b-a}{6}[f(a) + 4f(\frac{a+b}{2}) + f(b)]. \tag{A.10}$$

Algorithm A.1 Adaptive Simpson's Integration: a recursive formulation.

```
function ADAPTIVE-SIMPSON($f, a, b, \varepsilon, n$)

    input
      $f$ - Integrand      $a$ - Lower Bound      $b$ - Upper Bound
      $\varepsilon$ - Integration Precision      $n$ - Max Recursion Depth

    $c \leftarrow \frac{1}{2}(a+b)$                                          ▷ midpoint
    $h \leftarrow b - a$                                                     ▷ domain length
    $S \leftarrow \frac{h}{6}(f(a) + 4f(c) + f(b))$                          ▷ Simpon's on whole domain
    $S_{\text{left}} \leftarrow \frac{h}{12}\left(f(a) + 4f(\frac{a+c}{2}) + f(c)\right)$
    $S_{\text{right}} \leftarrow \frac{h}{12}\left(f(c) + 4f(\frac{b+c}{2}) + f(b)\right)$   ▷ Simpson's on each half
    if $(|S - S_{\text{left}} - S_{\text{right}}| < 15\varepsilon)$ or $(n \leq 0)$ then
        return $S_{\text{left}} + S_{\text{right}}$                           ▷ solution has desired precision
    else
        $S^*_{\text{left}} = \text{Adaptive-Simpson}\left(f, a, c, \frac{\varepsilon}{2}, n-1\right)$
        $S^*_{\text{right}} = \text{Adaptive-Simpson}\left(f, c, b, \frac{\varepsilon}{2}, n-1\right)$
        return $S^*_{\text{left}} + S^*_{\text{right}}$                      ▷ recursively subdivide each half
    end if
end function
```

The error in the integral approximation ε may then be defined as

$$\left| \int_a^b f(x)\mathrm{dx} - S(a,b) \right| < \varepsilon. \tag{A.11}$$

A well-known result for Simpson's rule is

$$\left| S(a,b) - S(a, \frac{a+b}{2}) - S(\frac{a+b}{2}, b) \right| < 15\varepsilon \tag{A.12}$$

which will form the basis for the definition of an adaptive quadrature rule.

The adaptive Simpson rule can be defined and implemented recursively for a generic function, as shown in algorithm A.1. The algorithm recursively bisects the interval until the user-set tolerance ε is attained, or until the maximum recursion depth is reached.

A.4. Generalized Oldroyd-B fluid

The analytical parabolic velocity profile for the Newtonian and Oldroyd-B model does not apply to the GOB model, which has a blunted parabolic velocity profile characteristic of a shear-thinning fluid. A relatively accurate numerical approximation may be used when prescribing inflow boundary conditions for this class of fluids. This will decrease the required inlet length, which is usually set as long enough so as to allow the flow to become fully developed before it reaches any region of interest. In the remainder of this section we describe briefly the numerical method used to obtain this approximation.

For a generalized Oldroyd-B fluid in steady-state, under the same geometry and boundary conditions as in section §A.2, the momentum equation simplifies to

$$\frac{dp}{dx} - \beta\,\frac{\partial^2 u_x}{\partial y^2} - \frac{\partial \tau_{xy}}{\partial y} \quad = \quad 0 \tag{A.13}$$

while the xy tensor component of the constitutive equation simplifies to

$$\tau_{xy} - \left((\alpha-\beta) + (1-\alpha)\,\phi(\frac{\partial u_x}{\partial y})\right)\frac{\partial u_x}{\partial y} = 0, \tag{A.14}$$

where $\phi(\frac{\partial u}{\partial y})$ represents a functional part of a specific viscosity model such as the Carreau-Yasuda model (2.15). By differentiating (A.14) with respect to y and then using this expression to eliminate the extra stress from (A.13), a 1D diffusion problem with a gradient-dependent diffusion coefficient is obtained:

$$\frac{dp}{dx} = \frac{\partial}{\partial y}\left((\alpha + (1-\alpha)\,\phi(\frac{\partial u_x}{\partial y}))\frac{\partial u_x}{\partial y}\right). \tag{A.15}$$

This equation will be solved using a finite-difference method on the domain $y \in [o, h]$, where h is the height of the channel. A fixed number $(N_{\mathrm{FD}}+1)$ of equally-spaced points on this interval will define our 1D mesh with discretization size $\Delta y = h/N_{\mathrm{FD}}$. Following the work of [51] on a similar problem, an artificial time-derivative is introduced to act as an iterative procedure. The x subscript is dropped from the velocity field u in (A.15) and the resulting PDE may be expressed as

$$\begin{aligned} \frac{\partial u}{\partial t} &= \frac{\partial}{\partial y}\left(g(\frac{\partial u}{\partial y})\frac{\partial u}{\partial y}\right) - \frac{dp}{dx}, \\ \text{where } g(\frac{\partial u}{\partial y}) &= (\alpha + (1-\alpha)\,\phi(\frac{\partial u}{\partial y})). \end{aligned} \tag{A.16}$$

A Crank-Nicholson time discretization is used in conjunction with a Picard method in each time step to linearize the diffusion coefficient. The resulting linear system for the velocity in the i^{th} spatial coordinate and $n+1^{th}$ time step is then given by

$$\begin{aligned} u_i^{n+1} &= u_i^n + \frac{s}{2}\left\{ g(\left(\frac{\partial u}{\partial y}\right)_{i+\frac{1}{2}}^{n+1*})(u_{i+1}^{n+1} - u_i^{n+1}) - g(\left(\frac{\partial u}{\partial y}\right)_{i-\frac{1}{2}}^{n+1*})(u_i^{n+1} - u_{i-1}^{n+1}) \right\} \\ &+ \frac{s}{2}\left\{ g(\left(\frac{\partial u}{\partial y}\right)_{i+\frac{1}{2}}^{n})(u_{i+1}^{n} - u_i^{n}) - g(\left(\frac{\partial u}{\partial y}\right)_{i-\frac{1}{2}}^{n})(u_i^{n} - u_{i-1}^{n}) \right\} - \Delta t\, \frac{dp}{dx}. \end{aligned} \quad (A.17)$$

The time step $n+1*$ refers to the best known solution for the current time step $n+1$, i.e. the solution at the previous Picard iteration. Furthermore we define $s = \Delta t/\Delta y^2$, and imply that the $i+\frac{1}{2}$ and $i-\frac{1}{2}$ spatial coordinate represent the average of the solution between the i^{th} and $i+1^{th}$ and $i-1^{th}$ spatial coordinates respectively. Lastly, we assume the definition of the spatial variable as $y_i = i\Delta y$.

Homogeneous Dirichlet boundary conditions are applied on the channel wall $y = h$, and homogeneous Neumann boundary conditions are applied on the symmetry boundary $y = 0$. These conditions can then be expressed as (A.18).

$$u_{N_{FD}+1} = 0 \text{ and } \frac{1}{\Delta x}(u_1 - u_0) = 0 \quad (A.18)$$

Poiseuille flow for a Newtonian fluid is chosen as an initial value for the iterative procedure which produces the velocity profile for the GOB model. Using this solution, the velocity gradient may be obtained using a second-order central-difference approximation. It is now possible to obtain the solution for the polymeric stress components using (A.8) for steady flows and (A.9) for unsteady flows. The latter case is relevant for pulsatile flow where the above steady solution is varied with time. In order to obtain values of the fields at quadrature points, a spline interpolation technique is used. GSL [38] procedures are incorporated into the code for this purpose.

Bibliography

[1] M.A. Alves, F.T. Pinho, and P.J. Oliveira. The flow of viscoelastic fluids past a cylinder: finite volume high-resolution methods. *Journal of Non-Newtonian Fluid Mechanics*, 97:207–232, 2001.

[2] M. Anand and K.R. Rajagopal. A shear-thinning viscoelastic fluid model for describing the flow of blood. *International Journal of Cardiovascular Medicine and Science*, 4(2):59–68, 2004.

[3] D.N. Arnold, F. Brezzi, B. Cockburn, and L.D. Marini. Unified analysis of discontinuous Galerkin methods for elliptic problems. *SIAM : Journal on Numerical Analysis*, 39(5):1749–1779, 2002.

[4] F.P.T. Baaijens. Application of low-order discontinuous Galerkin methods to the analysis of viscoelastic flows. *Journal of Non-Newtonian Fluid Mechanics*, 52:37–57, 1994.

[5] F.P.T. Baaijens. Numerical experiments with a discontinuous Galerkin method including monotonicity enforcement on the stick-slip problem. *Journal of Non-Newtonian Fluid Mechanics*, 51:141–159, 1994.

[6] F.P.T. Baaijens. Mixed finite element methods for viscoelastic flow analysis: a review. *Journal of Non-Newtonian Fluid Mechanics*, 79:361–385, 1998.

[7] W. Bangerth, R. Hartmann, and G. Kanschat. deal.II - a general purpose object orientated finite element library. *ACM Transactions on Mathematical Software*, 33(4):1–27, 2007.

[8] M. Behr, D. Arora, O. Coronado, and M. Pasquali. Models and finite element techniques for blood flow simulation. *International Journal for Computational Fluid Dynamics*, 20(3-4):175–181, 2006.

[9] S.A. Berger and L.D. Jou. Flows in stenotic vessels. *Annual Review of Fluid Mechanics*, 32:347–382, 2003.

[10] R.B. Bird, R.C. Armstrong, and O. Hassager. *Dynamics of Polymeric Liquids: Volume 1 Fluid Mechanics.* John Wiley and Sons, 1977.

[11] R.B. Bird and J.M. Wiest. Constitutive equations for polymeric fluids. *Annual Review of Fluid Mechanics*, 27:169–193, 1995.

[12] T. Bodnar, A. Sequeira, and M. Prosi. On the shear-thinning and viscoelastic effects of blood flow under various flow rates. *Applied Mathematics and Computation*, 217:5055–5067, 2011.

[13] J.C.G. Boot. *Quadratic Programming : Algorithms-Anomalies-Applications.* North-Holland Publishing Company-Amsterdam, 1964.

[14] S. Boyaval. Lid-driven-cavity simulations of Oldroyd-B models using free-energy-dissipative schemes. *Numerical Mathematics and Advanced Applications 2009*, pages 191–198, 2010.

[15] S. Boyaval, T. Leliévre, and C. Mangoubi. Free-energy-dissipative schemes for the Oldroyd-b model. *ESAIM : Mathematical Modelling and Numerical Analaysis*, 43(3):523–561, 2009.

[16] A. Brandt. Multi-level adaptive solutions to boundary-value problems. *Mathematics of Computation*, 31(138):333–390, 1977.

[17] A.N. Brooks and T.J.R. Hughes. Streamline upwind/Petrov-Galerkin formulation for convection dominated flows with particular emphasis on the incompressible Navier-Stokes equations. *Computational Methods in Applied Mechanical Engineering*, 94:285–299, 1982.

[18] R.A. Brown and G.A. McKinley. Report on the VIIth international workshop on numerical methods in viscoelastic flows. *Journal of Non-Newtonian Fluid Mechanics*, 52:407–413, 1994.

[19] R.L. Burden and J.D. Faires. *Numerical Analysis: Eighth Edition.* Thomson Brooks/Cole, 2005.

[20] P.J. Carreau. PhD thesis, University of Wisconsin, Madison, 1968.

[21] S. Chien, S. Usami, R.J. Dellenback, M.I. Gregersen, L.B. Nanninga, and M.M. Guest. Blood viscosity: influence of erythrocyte aggregation. *Science (New York)*, 157:829–831, 1967.

[22] Y.J. Choi, M.A. Hulsen, and H.E.H. Meijer. Simulation of the flow of viscoelastic fluid around a stationary cylinder using an extended finite element method. *Computers and Fluids*, 57:183–194, 2012.

[23] A.J. Chorin. Numerical solution of the Navier-Stokes equations. *Mathematics of Computation*, 22(104):745–762, 1968.

[24] A.J. Chorin and J.E. Marsden. *A Mathematical Introduction to Fluid Mechanics: Third Edition.* Springer-Verlag New York, 1993.

[25] B. Cockburn, G.E. Karniadakis, and C.W. Shu. The development of discontinuous Galerkin methods. *UMSI research report/University of Minnesota (Minneapolis, Mn). Supercomputer institute 99*, page 220, 2000.

[26] B. Cockburn and C.W. Shu. A local discontinuous Galerkin method for time-dependent convection-diffusion systems. *SIAM Journal on Numerical Analysis*, 35(6):2440–2463, 1998.

[27] O.M. Coronado, D. Arora, M. Behr, and M. Pasquali. A simple method for simulating general viscoelastic fluid flows with an alternate log-conformation formulation. *Journal of Non-Newtonian Fluid Mechanics*, 147:189–199, 2007.

[28] T.A. Davis and I.S. Duff. An unsymmetric-pattern multifrontal method for sparse LU factorization. *SIAM Journal on Matrix Analysis and Applications*, 18(1):140–158, 1997.

[29] J. Donea and A. Huerta. *Finite Element Methods for Flow Problems.* John Wiley and Sons, 2003.

[30] H.S. Dou and N.P. Thien. The flow of an Oldroyd-B fluid past a cylinder in a channel: adaptive viscosity vorticity (davss-omega) formulation. *Journal of Non-Newtonian Fluid Mechanics*, 87(1):47–73, 1999.

[31] Y. Fan, R.I. Tanner, and N. Phan-Thien. Galerkin/least-square finite-element method for steady-viscoelastic flows. *Journal of Non-Newtonian Fluid Mechanics*, 84:233–256, 1999.

[32] J. Fang and R. G. Owens. Numerical simulations of pulsatile blood flow using a new constitutive model. *Biorheology*, 43(5):637–660, 2006.

[33] R. Fattal and R. Kupferman. Time-dependent simulation of viscoelastic flows at high Weissenberg number using the log-conformation representation. *Journal of Non-Newtonian Fluid Mechanics*, 126:23–37, 2005.

[34] R.P Fedorkeno. A relaxation method for solving elliptic difference equations. *Zhurnal Vychislitel'noi Matematiki i Matematicheskoi Fiziki*, 1(5):922–927, 1961.

[35] J. Fish and T. Belytschko. *A First Course in Finite Elements.* John Wiley and Sons, 2007.

[36] M. Fortin. Old and new finite elements for incompressible flows. *International Journal for Numerical Methods in Fluids*, 1(4):347–364, 1981.

[37] M. Fortin and A. Fortin. A new approach for the FEM simualtion of viscoelastic flows. *Journal of Non-Newtonian Fluid Mechanics*, 32:295–310, 1989.

[38] M. Galassi, J. Davies, J. Theiler, B. Gough, G. Jungman, P. Alken, M. Booth, and F. Rossi. GNU scientific library. *Network Theory*, 2002.

[39] A.M. Grillet, B. Yang, B. Khomami, and E.S.G. Shaqfeh. Modeling of viscoelastic lid driven cavity flow using finite element simulations. *Journal of Non-Newtonian Fluid Mechanics*, 88:99–131, 1999.

[40] J.L. Guermond, P. Minev, and J. Shen. An overview of projection methods for incompressible flows. *Computational Methods in Applied Mechanics and Engineering*, 195:6011–6045, 2006.

[41] T. Hayat, M. Khan, and M. Ayub. Exact solutions of flow problems of an Oldroyd-b fluid. *Applied Mathematics and Computation*, 151:105–119, 2004.

[42] J.G. Heywood, R. Rannacher, and S. Turek. Artificial boundaries and flux and pressure conditions for the incompressible Navier-Stokes equations. *International Journal for Numerical Methods in Fluids*, 22:325–352, 1996.

[43] H. Hoteit, P. H. Ackerer, R. Mosé, J. Erhel, and B. Philippe. New two-dimensional slope limiters for discontinuous Galerkin methods on arbitrary meshes. *International Journal for Numerical Methods in Engineering*, 61:2566–2593, 2004.

[44] D. Hu and T. Lelievre. New entropy estimates for the Oldroyd-B model, and related models. *Communications in Mathematical Sciences*, 5(4):909–916, 2007.

[45] T.J.R. Hughes. *The Finite Element Method: Linear Static and Dynamic Finite Element Analysis.* Prentice Hall Inc., 1987.

[46] M.A. Hulsen, A.P.G. Van Heel, and B.H.A.A. Van Den Brule. Simulation of viscoelastic flows using Brownian configuration fields. *Journal of Non-Newtonian Fluid Mechanics*, 70:79–101, 1997.

[47] M.A. Ikbal. Viscoelastic blood flow through arterial stenosis - effect of variable viscosity. *International Journal of Non-Linear Mechanics*, 2012.

[48] A. Iolov, A.S. Kane, Y. Bourgault, R.G. Owens, and A. Fortin. A finite element method for a microstructure-based model of blood. *International Journal for Numerical Methods in Biomedical Engineering*, 27:1321–1349, 2011.

[49] D.F. James. Boger fluids. *Annual Review of Fluid Mechanics*, 41:129–142, 2009.

[50] B. Jannsen and G. Kanschat. Adaptive multilevel methods with local smoothing for H1- and H-curl-conforming high order finite element methods. *SIAM: Journal of Scientific Computing*, 33(4):2095–2114, 2011.

[51] S.C. Jardin, G. Bateman, G.W. Hammett, and L.P. Ku. On 1d diffusion problems with a gradient-dependent diffusion coefficient. *Journal of Computational Physics*, 227:8769–8775, 2008.

[52] V.N. Kalashnikov. Shear-rate dependent viscosity of dilute polymer solutions. *Journal of Rheology*, 38(5):1385–1403, 1994.

[53] G. Kanschat. Multi-level methods for discontinuous Galerkin FEM on locally refined meshes. *Computers and Structures*, 82:2437–2445, 2004.

[54] G. Karypis and V. Kumar. A fast and high quality multilevel scheme for partitioning irregular graphs. *SIAM Journal on Scientific Computing*, 20(1):359–392, 1998.

[55] R. Keunings. On the high Weissenberg number problem. *Journal of Non-Newtonian Fluid Mechanics*, 20:209–226, 1986.

[56] J.M. Kim, C. Kim, K.H. Ahn, and S.J. Lee. An efficeint iterative solver and high-resolution computations of the Oldroyd-b fluid flow past a confined cylinder. *Journal of Non-Newtonian Fluid Mechanics*, 123:161–173, 2004.

[57] H. Lee. A multigrid method for viscoelastic fluid flow. *SIAM Journal on Numerical Analysis*, 42:109–129, 2004.

[58] P. Lesaint and P.A. Raviart. *On a Finite Element Method for Solving the Neutron Transport Equation.* Univ. Paris VI, Labo. Analyse Numérique, 1974.

[59] A. Leuprecht and K. Perktold. Computer simulation of non-Newtonian effects on blood flow in large arteries. *Computer Methods in Biomechanics and Biomedical Engineering*, 4(2):149–163, 2001.

[60] J.K-J. Li. *Dynamics of the Vascular System- Vol .1.* World Scientific Publishing Co. Pte. Ltd., 2004.

[61] A. Lozinski and R.G. Owens. An energy estimate for the Oldroyd-B model: theory and applications. *Journal of Non-Newtonian Fluid Mechanics*, 112:161–176, 2003.

[62] J.M. Marchal and M.J. Crochet. A new mixed fintie element for calculating viscoelastic flow. *Journal of Non-Newtonian Fluid Mechanics*, 26:77–114, 1987.

[63] J. Mewis and N.J. Wagner. Thixotropy. *Advances in Colloid and Interface Science*, 147-148:214–227, 2009.

[64] H.B.H. Mohamed and B.D. Reddy. Some properties of models for generalized Oldroyd-B fluids. *International Journal for Engineering Science*, 48:1470–1480, 2010.

[65] L. Nadau and A. Sequeira. Numerical simulations of shear-dependent viscoelastic flows with a combined finite element-volume method. *Computers and Mathematics with Applications*, 53:547–568, 2007.

[66] A. Najet, V. Abdollahi, and K. Vahidkhan. Lattice Boltzmann simulation of non-newtonian flows past confined cylinders. *Journal of Non-Newtonian Fluid Mechanics*, 166:689–697, 2011.

[67] J.G. Oldroyd. On the formulation of rheological equations of state. *Proceedings of the Royal Society of London. Series A, Mathematical and Physical Sciences*, 200(1063):523–541, 1950.

[68] R.G. Owens, C. Chauvière, and T.N. Philips. A locally upwinded spectral technique (LUST) for viscoelastic flows. *Journal of Non-Newtonian Fluid Mechanics*, 108:49–71, 2002.

[69] R.G. Owens and T.N. Phillips. Steady viscoelastic flow past a sphere using spectral elements. *International Journal for Numerical Methods in Engineering*, 39:1517–1534, 1996.

[70] R.G. Owens and T.N. Phillips. *Computational Rheology.* Imperial College Press, 2002.

[71] P. Pakdel and G.H. McKinley. Cavity flows of elastic liquids: purely elastic instabilities. *Physics of Fluids*, 10(5):1058–1070, 1998.

[72] P. Pakdel, S.H. Spiegelberg, and G.H. McKinley. Cavity flows of elastic liquids: two-dimensional flows. *Physics of Fluids*, 9(11):3123–3140, 1997.

[73] T.W. Pan and J Hao. Numerical simulation of a lid-driven cavity viscoelastic flow at high Weissenberg numbers. *Comptes Rendus Mathematique*, 344:238–286, 2007.

[74] N. Phan-Thien and R.I. Tanner. A new constitutive equation derived from network theory. *Journal of Non-Newtonian Fluid Mechanics*, 2(4):353–365, 1977.

[75] G. Pontrelli. Pulsatile blood flow in a pipe. *Computers and Fluids*, 27(3):367–380, 1998.

[76] G. Pontrelli. Blood flow through a circular pipe with an impulsive pressure gradient. *Mathematical Models and Methods in Applied Sciences*, 10(2):187–202, 2000.

[77] G. Pontrelli. Blood flow through an axisymmetric stenosis. *Proceedings of the Institution of Mechanical Engineers, Part H: Journal of Engineering in Medicine*, 215:1–10, 2001.

[78] W.H. Press, S.A. Teukolsky, W.T. Vetterling, and B.P. Flannery. *Numerical Recipes in C++, The Art of Scientific Computing (Third Edition).* Cambridge University Press, 2007.

[79] W.H. Reed and T.R. Hill. Triangular mesh methods for the neutron transport equation. *Tech. Report LA-UR-73-479, Los Alamos Scientific Laboratory, Los Alamos, NM*, 1973.

[80] J. Reinders. *Intel threaded building blocks: outfitting C++ for multi-core processor parallelism.* O'Reilly Media , Incorporated, 2007.

[81] B. Riviére. *Discontinuous Galerkin Methods for Solving Elliptic and Parabolic Equations: Theory and Implementation.* SIAM : Frontiers and Applied Mathematics Vol 35., 2008.

[82] A.M. Robertson, A. Sequeira, and R.G. Owens. Rheological models for blood. *Cardiovascular Mathematics*, pages 211–241, 2009.

[83] A.H. Shiang, A. Öztekin, J-C. Lin, and D. Rockwell. Hydroelastic instabilities in viscoelastic flows past a cylinder confined in a channel. *Experiments in Fluids*, 28:128–142, 2000.

[84] K.D. Smith and A. Sequeira. Micro-macro simulations of a shear-thinning viscoelastic kinetic model: application to blood flow. *Applicable Analysis*, 90(1):227–252, 2011.

[85] R. Temam. Une méthode d'approximation des solutions des équations Navier-Stokes. *Bull. Soc. Math. France*, 98:115–152, 1968.

[86] G.B. Thurston. Viscoelasticity of human blood. *Biophysical Journal*, 12:1205–1217, 1972.

[87] C. Tu and M. Deville. Pulsatile flow of non-newtonian fluids through arterial stenosis. *Journal of Biomechanics*, 29(7):899–908, 1996.

[88] S. Turek. *Efficient Solvers for Incompressible Flow Problems.* Springer-Verlag Berlin Heidelberg New York, 1991.

[89] P. Wapperom, R. Keunings, and V. Legat. The backward-tracking Lagrangian particle method for transient viscoelastic flows. *Journal of Non-Newtonian Fluid Mechanics*, 91:273–295, 2000.

[90] P. Wesselling. *An Introduction to Multigrid Methods.* John Wiley and Sons, 1992.

[91] K.K. Yeleswarapu, M.V. Kameneva, K.R. Rajagopal, and J.F. Antaki. The flow of blood in tubes: theory and experiment. *Mechanics Research Communications*, 25(3):257–262, 1998.

[92] D.F. Young and F.Y. Tsai. Flow characteristics in models for arterial stenoses - I. Steady flow. *Journal of Biomechanics*, 6(4):395–410, 1973.

[93] D.F. Young and F.Y. Tsai. Flow characteristics in models of arterial stenoses - II. Unsteady flow. *Journal of Biomechanics*, 6(5):547–559, 1973.

[94] F. Yurun. A comparative study of the discontinuous Galerkin and continuous SUPG finite element methods for computation of viscoelastic flows. *Computational Methods in Applied Mechanics and Engineering*, 141:47–65, 1997.

[95] O.C. Zienkiewicz. *The Finite Element Method: Third Edition.* McGraw-Hill Book Company (UK) Limited, 1977.